FABRICATION AND OPTIMIZATION OF RF-SQUID AND SQUID INTEGRATION ASSEMBLY FOR HIGH RESOLUTION MAGNETIC IMAGING SYSTEMS

A DISSERTATION SUBMITTED TO
THE DEPARTMENT OF ELECTRICAL AND ELECTRONICS ENGINEERING
AND THE INSTITUTE OF ENGINEERING AND SCIENCE
OF BILKENT UNIVERSITY
IN PARTIAL FULFILLMENT OF THE REQUIREMENTS
FOR THE DEGREE OF
DOCTOR OF PHILOSOPHY

By
Rizwan Akram
August 2005

I certify that I have read this thesis and that in my opinion it is fully adequate, in scope and in quality, as a dissertation for the degree of doctor of philosophy.

Assist. Prof. Dr. Mehdi Fardmanesh(Adviser)

I certify that I have read this thesis and that in my opinion it is fully adequate, in scope and in quality, as a dissertation for the degree of doctor of philosophy.

Prof. Dr. Doğan Abukay

I certify that I have read this thesis and that in my opinion it is fully adequate, in scope and in quality, as a dissertation for the degree of doctor of philosophy.

Prof. Dr. Levent Gürel

I certify that I have read this thesis and that in my opinion it is fully adequate, in scope and in quality, as a dissertation for the degree of doctor of philosophy.

Prof. Dr. Billur Barshan

I certify that I have read this thesis and that in my opinion it is fully adequate, in scope and in quality, as a dissertation for the degree of doctor of philosophy.

Assoc. Prof. Dr. Ahmet Oral

Approved for the Institute of Engineering and Sciences:

Prof. Dr. Mehmet Baray
Director of the Institute of Engineering and Sciences

ABSTRACT

FABRICATION AND OPTIMIZATION OF RF-SQUID AND SQUID INTEGRATION ASSEMBLY FOR HIGH RESOLUTION MAGNETIC IMAGING SYSTEMS

Rizwan Akram
Ph.D. in Electrical and Electronics Engineering
Supervisor: Assist. Prof. Dr. Mehdi Fardmanesh
August 2005

Superconducting QUantum Interference Devices or SQUIDs are by far the most sensitive devices known for sensing magnetic flux down to a resolution of about 10^{-21}Wb and finds innumerous applications in various fields. In order to apply these sensors to sense nano structures or to use in antibody or antigen ammunoassay experiments, especially in unshielded environments at Liquid Nitrogen temperatures, one needs to optimize the SQUIDs for high SNR and low background magnetic field sensitivity. The chief motivation for this research work and this thesis is to optimize and characterize HTc rf-SQUIDs so that high field sensitivity and high spatial resolution could be obtained.

During the course of this study, rf-SQUIDs were fabricated using SEJ and Bicrystal technology and optimized for the above mentioned characteristics. In the next stage, these optimized sensors were integrated into an imaging system after a thorough investigation on problems related to the front-end assembly of such a system. Different SQUID microscope systems have been designed, fabricated, and tested in order to achieve high field sensitivity and high spatial resolution magnetic imaging under the constraint of keeping the sample at room temperature, while the SQUID is in Liquid Nitrogen Temperature. Using the developed systems, magnetic imaging of room temperature samples with sensitivities in the range of about $100fT/\sqrt{(Hz)}$ and spatial resolution of about 100 μm were achieved.

Keywords: Superconductor, YBCO, Josephson Junction, Step Edge junction, Bicrystal junction, rf-SQUID, Scanning SQUID microscope.

ÖZET

Rizwan Akram
Elektrik ve Elektronik Mühendisliği, Doktora
Tez Yöneticisi: Yrd. Doç. Dr. Mehdi Fardmanesh
Ağustos 2005

Süperiletken Kuantum Girişim Aygıtları veya SQUID'ler, manyetik alan algılamada yaklaşık 10^{-21}Wb çözünürlükle şimdiye kadar bilinen en hassas aygıtlardır ve çeşitli alanlarda sayısız uygulamaları bulunmaktadır. Bu sensörleri özellikle sıvı nitrojen sıcaklığında koruyucu kılıfı olmayan ortamlarda, nano yapıları algılamak amacıyla uygulamak veya antikor-antijen belirleme deneylerinde kullanmak için, SQUID'lerin yüksek SNR ve düşük arka plan manyetik alan duyarlılığına optimize edilmesi gerekmektedir. Bu araştırma çalışması ve tez için ana amaç, HTc rf-SQUID'lerin karakterizasyonu ve optimize edilmesi sonucunda yüksek alan duyarlılığı ve yüksek uzaysal çözünürlüüün elde edilebilmesidir.

Bu çalışma süresince rf-SQUID'ler, SEJ ve Bi-kristal teknoloji kullanılarak üretilmiştir ve yukarıda bahsedilen karakterizasyonlar için en iyi şekilde optimize edilmiştir. Bir sonraki adımda, optimize edilmiş sensürler büyle bir sistemin kurulumundan ünce ve sonrasına bağlı olarak problemlerin tamamen araştırılmasından sonra bir gürüntüleme sistemine entegre edilmiştir. SQUID sıvı azot ortamındayken, ürnek oda sıcaklı sınırlarında tutularak, yüksek alan hassasiyeti ve yüksek uzaysal çözünürlüklü manyetik görüntü elde edebilmek amaıyla farklı SQUID mikroskop sistemleri tasarlanmış, üretilmiş ve test edilmiştir. Geliştirilen sistemleri kullanarak oda sıcaklığındaki örneğin manyetik görüntüsü yaklaşık olarak $100fT/\sqrt{(Hz)}$ sınırı içerisinde bir hassasiyetle ve yaklaşık 100μm uzaysal çözünürlük elde edilmesi başarılmıştır.

Anahtar sözcükler: Süperiletken, YBCO, Josephson kavşak, Step Edge kavşak, Bi-Kristal Kavşak, rf-SQUID, SQUID tarama mikroskoplar.

Acknowledgement

It is my pleasure to express my sincere gratitude to my supervisor, Dr. Mehdi Fardmanesh for his invaluable guidance, encouragement, and support throughout this endeavour. I am deeply indebted to him.

I would like to thank the members of my thesis committee, Prof. Doğan Abukay, Prof. Levent Gürel, Prof. Billur Barshan, and Prof. Ahmed Oral for reading and commenting on this thesis.

I am obliged to thank my co-researchers in Forschungszentrum Jülich (Germany), Dr. H.-J. Krause, Dr. J. Schubert, Dr. Yi Zhang, Dr. M. Bick, Mr. M. Banzet, Mr. D. Lomparski, Mr. W. Zander, Mr. M. Schmidt, and the rest of the group for their constant support, suggestions, and help in making the setup and in the developing the devices. It would be an understatement to say that I learnt a lot from them.

I am thankful to BMBF, The German Ministry of Education and Research, and TÜBİTAK, The Scientific and Technological Research Council of Turkey, for sponsoring the joint project with Forschungszentrum Jülich.

Special Thanks to the Advanced Research Laboratory (Physics Department, Bilkent Univ.), for providing Liquid Nitrogen during innumerous occasions.

I would also like to thank S. Ersin Başar and Ergün Hırlakoğlu, Lab Technicians, for their continuous help in establishing the electrical and mechanical setups.

I also thank my friends inside and outside the department, especially Ali Bozbey and Anirudh Srinivasan for their help and support.

I would like to express my deepest gratitude to S. Imaduddin Qadri, Dr. S. Fakhre Mahmud and Dr. S. Iftekhar Ahmed and their families for their relentless encouragement and moral support during all of my endeavors. Last, but not the least, I thank my family for their understanding, love, and countless prayers.

To My Parents.

Contents

List of Figures

List of Tables

Chapter 1

Introduction and Literature Survey

1.1 Introduction

Effect of magnetism is known from ancient times for about more than 4000 years. But till 19^{th} century, it was just used as compass for medieval explorers to navigate [7]. Though, discovery of the first quantitative magnetometers was late till 19^{th} century, application of magnetic sensors today has a wide range such as metrological, domestic and industrial proximity switching, electromagnetic non-destructive testing, geomagnetic, and prospecting a biomagnetism [8].

Two inherently different types of magnetic sensors exist: absolute and vectorial. Absolute magnetometers are based on Zeeman effect and are scalar magnetic field-to-frequency converters, measuring the absolute values of the field, regardless of the orientation, with field sensitivities of few $pT/\sqrt{Hz}$ with bandwidth of 1 Hz to 1kHz [9], [10]. Whereas for vectorial sensors, projection of the field vector onto the sensitive direction of the device is measured. As the magnetic flux penetrating a pickup area is detected, they can be regarded as magnetic flux-to-voltage converters. In this case, field sensitivities of a few $pT/\sqrt{Hz}$ with about 1000 Hz bandwidth are attainable [11]. Hall probes [12] and conventional

magnetoresistors are based on galvanomagnetic effects occurring in semiconductors and metals [13], [14]. Field sensitivities of Hall probes lie in the range of a few hundred $nT/\sqrt{Hz}$. Whereas field sensitivity in magnetoresistive sensors, based on carrier scattering with the lattice results in the increased electrical path length causeing a change in the electrical resistance, typically range around a few hundred $pT/\sqrt{Hz}$. For low-field sensitivity, high-permeability ferromagnetic Ni-Fe alloys and flux focusers are employed [15]. This way record sensitivity values down to $1pT/\sqrt{Hz}$ have been reported. In addition to sensitivity limitations of each of the sensors described above, limitations in spatial resolution, dynamic range, linearity, bandwidth and the thermal and temporal stability have to be taken into account.

In terms of detectability of localized weak dipoles, the flux sensitivity is the figure of merit of the sensor. The SQUID "Interferometers or superconducting quantum interference devices (SQUIDs)" is by far the most sensitive sensor of magnetic flux known, reaching a resolution of 10^{-21} Wb. Magnetic field resolution in the range of $fT/\sqrt{Hz}$ are possible with a pickup area of only few square millimeters. Magnetic flux quantization in the superconducting loop and the Josephson effect lead to a flux-to-voltage characteristic with flux quantum peridocity. Hence, an extremely large dynamic range is attainable, especially when combining a null-detector scheme with flux quanta counting. The only major draw back of SQUIDs is that they require cooling to very low temperatures, with the attending relatively high cost and somewhat complicated handling.

SQUID works on the basis of interference of the superconducting wave function across a junction called the Josephson junction. It is a deceptively simple device, consisting of a small superconducting loop of inductance L_s with one or two damped (resistively shunted, RSJ) Josephson junctions, each having a critical current, I_c, and normal resistance, R_n. Magnetic flux threading the superconducting loop is always quantized in units of Φ_0, where $\Phi_0 = 2.0679 \times 10^{-5}$Wb is the flux quantum. The phase difference across a Josephson junction switches by 2π when its current crosses I_c. In brief, the junction is shortening the single junction SQUID by a superconducting path; therefore, the voltage response is obtained by coupling the loop to a radio frequency biased tank circuit. For

this reason this kind of devices is usually called an rf-SQUID, which is further discussed later in this chapter. In the double junction configuration, the weak links are not shorted by a continuous superconducting path; therefore, the dc current-voltage characteristics can be observed. In the operating conditions, the device is current biased at a value slightly greater than the critical current, and the voltage drop across it is monitored. These kinds of devices are usually called dc-SQUIDs.

Here, we will analyze the rf-SQUID in details as during the course of this study rf-SQUID has been the basic sensor for the targeted scanning SQUID microscope, used either in magnetometer or gradiometer configuration. Both configurations will be discussed in detail later in this chapter.

1.2 Thesis Organization

The first chapter of this thesis discusses the basic requirements for developing the high resolution imaging system using Optimized SQUID sensor and SQUID integration assembly. The necessary literature survey on the basic components of a SQUID sensor, its working principle, and some necessary formulations to be able to follow the discussions in the forthcoming chapters are also included.

The second chapter discusses Josephson junctions in detail, starting from fabrication techniques, and the characterization setup to the individual characteristics of Step Edge Junctions and Bi crystal grain boundary Josephson junctions. This is based on the $I - V$ characteristics and magnetic field dependencies of these particular junctions.

Chapter 3 is on the rf-SQUID sensors. In this chapter we discuss in rigorous detail the important issues related to the fabrication and optimization of rf-SQUIDs for high resolution magnetic imaging systems.

The impediments related to the front end assembly of microscope is discussed in chapter 4. The expected solutions to these problems have also been discussed

in details in this chapter.

Chapter 5 includes the developed and investigated systems for scanning SQUID microscopy with advantages and disadvantages together with scanning results on wire samples and dipoles to find out the ultimate field and spatial resolution of the developed prototype system.

Summary and conclusions are presented in chapter 6 together with the scientific contributions of this work and some suggestions for future work for improving the spatial resolution by using multi layer self shielded transformer structures.

1.3 Requirements for SQUID magnetic imaging

To make a SQUID microscope we need to optimize the SQUID properties for stability of working in the desired temperature range while having low noise as well as background field independence. What we need as a first site is to have high temperature Superconductor, HTS, junctions which have the highest possible I_cR_n product at 77K in the range between 0.1 and 1 mV, to provide high V_{spp} at this temperature. Higher I_cR_n value conforms high signal to noise ratio (SNR). Of the many types of internally shunted HTS Josephson junctions, which have been investigated and developed in the past decade, only some can approach these requirements. The grain boundary bicrystal junction, i.e, microbridges patterned on bicrystal substrates, typically $SrTiO_3$, have been preferentially used by most experimenters and SQUID vendors [16], [17], [18], [19]. Other types of junctions currently used by some of leading experimental groups are: GB step-edge junctions patterned as microbridges across steep steps locally etched in substrates [20], SNS step-edge junctions with normal interlayer across the step in substrate being gold, silver or an Au-Ag alloy [21], quasi-planar SNS edge (ramp) junctions with praseodymium cuprate $PrBa_2Cu_3O_{7-\delta}$ (PBCO) barriers [22], and SNS junctions consisting of oxygen-ion implanted weak links [23]. Not used commercially, but worthy of mentioning are the CAM (c-axis microbridge) planar junctions, which unfortunately have low R_n [24].

Each of the above mentioned types, offers some advantages and disadvantages. Bicrystal junctions are the easiest to fabricate and their I_c and R_n are relatively reproducible with spreads lower than in most other types (best $1\sigma = 20$ to 30%). Here, they are particularly suitable for dc-SQUIDs where the I_c and R_n of the two junctions should be nearly identical. However, bicrystal substrates are expensive and impose topological limitations on the SQUID layout design, since the grain boundary extends across the whole substrate. When it intersects other parts of the superconducting layout, such as the washer body or the flux pickup loop, additional 1/f flux noise is likely to be generated in the film's grain boundary. This boundary represents a long Josephson junction, in which Josephson vortices can easily shuttle. Another disadvantage of this method is the small integration scale of junctions since all junctions are aligned along the bicrystal boundary.

In the step-edge process, steps of thicknesses comparable to the film thickness are made in the substrate by etching. When the YBCO film is grown across the edge, the c-axis is tilted and at least two grain boundaries are formed. It has been possible to adjust the junction parameters by adjusting the step height and angle, but the junction reproducibility has been low [25]. Stepedge GB junctions use less expensive substrates and can be relatively freely positioned on the substrate (when a series connection of two junctions is acceptable), but their reproducibility is poorer and have typical spreads of parameters much larger compared to e.g. bicrystal junctions. These junctions found application mostly in rf-SQUIDs, as only one junction is required there. The I_c and R_n of both mentioned GB junction types can be easily adjusted or trimmed by annealing in oxygen, inert atmosphere, or vacuum. This is done at temperatures low enough for YBCO films properties not to be seriously affected, except at the grain boundary [26]. The R_n values for a few microns wide junctions are typically in the 1 to 10Ω range, suitable for SQUID operation. The correlation between I_c and R_n is given by the scaling law in the form:

$$I_c R_n \propto (1/\rho_n)^q or I_c R_n \propto (J_c)^{\frac{q}{q+1}}, \tag{1.1}$$

where ρ_n is R_n times the junction's area, and q can vary somewhat, but is usually

about 1.5 on $SrTiO_3$. This scaling is generally valid for HTS junctions.

In the biepitaxy process, a thin (l0-20 nm) seed layer is deposited epitaxially on part of a substrate. During the YBCO growth, the in-plane $(a-b)$ orientation is different for the film grown on the seed layer compared to other parts of the substrate, and hence, grain boundaries are formed at the borders. Most processes give a 45^o rotation, but misorientation angles of 18^o and 27^o have also been reported [27].

The SNS step-edge junctions insure a similar freedom of positioning as the GB step edge type, but the fabrication process is much more difficult and has been mastered by only a couple of laboratories [28], [29]. However, these junctions apparently exhibit excellent long-term stability and reasonable spreads of I_c and R_n, comparable to those found in bicrystal junctions on $SrTiO_3$. Similarly, freedom of positioning, excellent long term stability, and acceptable spread are claimed for edge junctions with PBCO barriers, and for ion implanted SNS weak links, but again at a price of a complicated fabrication process. For SNS and ramp junctions, the typical values of I_c and R_n can be made comparable to those of GB junctions. Today, no optimum type of junctions for SQUIDs can be identified. However, it is probable that with continuing progress in fabrication process, the GB junctions will be replaced by one or another type of SNS or PBCO barrier junctions suitable for multilayered SQUID structures [30].

1.4 Josephson Junction

1.4.1 Introduction

The term tunneling is applicable when an electron passes through a region, in which the potential is such that a classical particle with the same kinetic energy can not pass, as shown in Figure 1.1. In quantum mechanics, one finds that an electron incident on such a barrier has a certain probability of passing through, depending on the height, width, and the shape of the barrier.

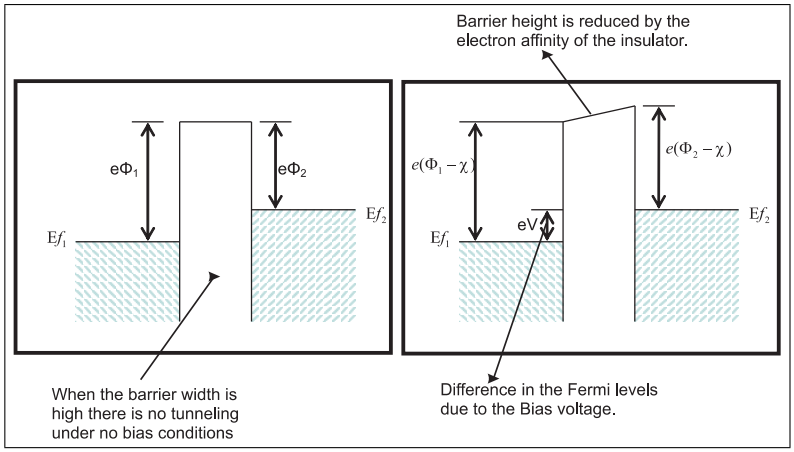

Figure 1.1: Left; Fermi levels in two isolated metals with different work functions. Right; Energy levels in metal-insulator-metal junction with a bias V applied to left side.

There are different types of tunneling junctions which can be made, like normal-insulator-normal (NIN), normal-insulator-superconductor (NIS), and Superconductor-insulator-Superconductor (SIS). Here in this section we study the SIS type of tunnel junction before going in to the analysis of the particular GB case.

1.4.2 Josephson effect

The idea of tunneling of electron pairs between closely spaced superconductors even with no potential difference was first suggested by B.D. Josephson during his PhD. in 1962. This goes back to formation of junctions between two superconductors, which are weak enough to allow slight overlap of electron pair wave function of two individual superconductors as shown in Figure 1.2.

In addition to this so-called Josephson tunnel junction (or SIS Junction, Superconductor Insulator Superconductor) numerous other configurations also allows weak coupling between two superconductors for both metallic (LT_cSC) and oxide (HT_cSC) materials. This includes thin normal conducting layer (SNS) junctions, micro bridges, grain boundaries, damaged regions, and point contacts serving as weak contacts. The most important characteristic property of the pair

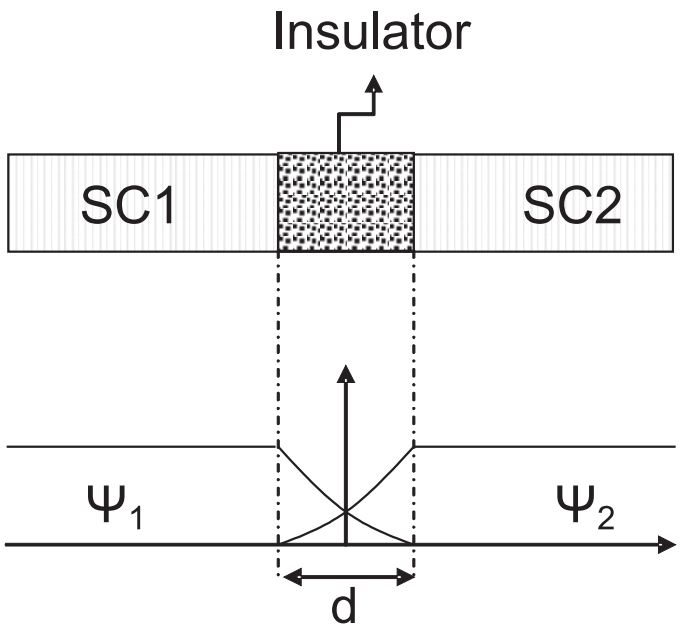

Figure 1.2: Schematic of Josephson junction with the wave function representations in the barrier region.

tunneling is that, unlike quasi particle tunneling, it does not involve excitations and can occur even without bias across the junction. This refers to absence of voltage when we bias the junction with currents less than critical current where this current is carried through the junction by cooper pairs.

1.4.2.1 Josephson Relations

Wave function to describe the pairs in the superconductors can be expressed in the form as,

$$\psi = |\psi(r)| \exp\{i\theta(r) - (2\varepsilon_f/\hbar)\}, \tag{1.2}$$

where $|\psi(r)|^2$ represents the actual Cooper pair density, n_s. As the separation of the superconductors is reduced, the wave functions penetrate the barrier sufficiently to couple where the system energy is reduced by the coupling. When this energy exceeds the thermal fluctuation energy, the phases become locked and pairs can pass from one SC to the other without energy loss. Under biased condition, the only difference between the pair tunneling is that this time phases

of wave function are not locked but rather slip relative to each other at a rate that is precisely related to the voltage. Time evolution of the wave function of the superconductor on each side of a coupled Josephson junction results in the following famous Josephson relations;

$$J = J_c \sin \phi \tag{1.3}$$

where J_c is the critical current density and,

$$\frac{\partial \phi}{\partial t} = \frac{2e}{\hbar} V \tag{1.4}$$

These are the Josephson relations that express the behavior of the electron pairs. From these Josephson relations, it can be inferred that coupling of the wave function reduces the energy which can be expressed as,

$$E_c = (\hbar I_c / 2e) \cos \phi \tag{1.5}$$

so coupling energy is maximum when ϕ=0, but as the current density, J, is raised to its maximum value of J_c, $\phi \rightarrow \pi/2$ and coupling energy is reduced to zero. For currents where $J > J_c$, the wave functions become uncoupled and begin to slip relative to each other at a rate determined by phase equation. General expression from microscopic theory for the maximum zero-voltage current density, can be written as :

$$J_{ctu} = \frac{G_n}{A} \left(\frac{\pi \Delta(T)}{2e} \right) \tanh \frac{\Delta(T)}{2k_B T} \tag{1.6}$$

where G_n is the tunneling conductance for $V \gg 2\Delta/e$ and A is the junction area. Figure 1.3 shows the $I - V$ characteristics of the tunnel junction at $T = 0$.

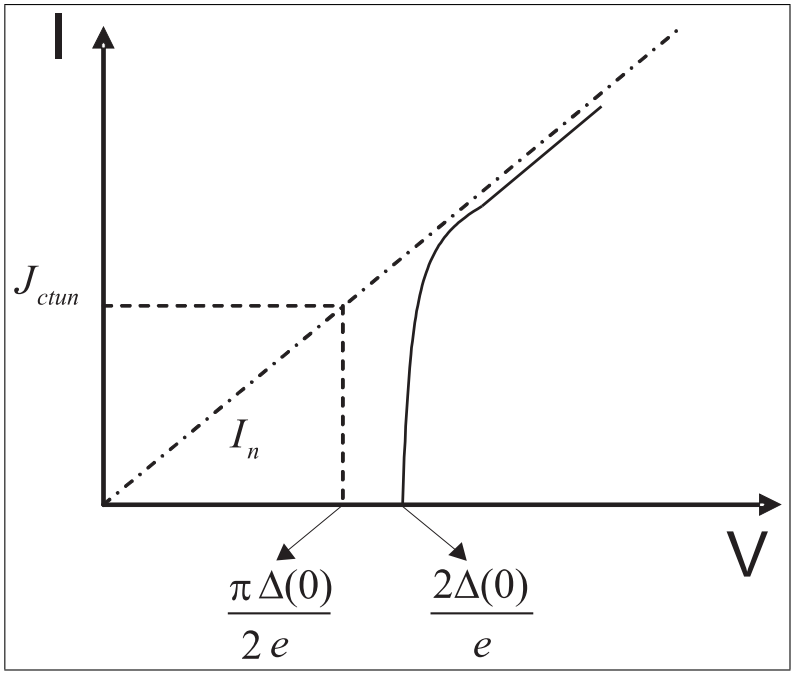

Figure 1.3: $I-V$ characteristic for a Josephson junction at $T = 0$K. the maximum zero-voltage current is equal to the normal-state current at $\pi/4$ of the quasiparticle tunneling gap.

1.4.2.2 Josephson Ac Effect

If a dc-voltage $\imath$V$\prime$ is applied to a junction, integration of second Josephson relation shows that

$$\phi = \phi_0 + (2e/\hbar)\, Vt. \tag{1.7}$$

If this is substituted into current density expression we obtain,

$$I = I_c \sin(\omega_J t + \phi_0). \tag{1.8}$$

So there is an ac current at the frequency,

$$f_J = \frac{\omega_J}{2\pi} = \left(\frac{1}{2\pi}\right)\frac{2e}{\hbar}V. \tag{1.9}$$

An important aspect of this result is that substantial ac pair currents flow even when the junction voltage exceeds the gap by several times. So it can be referred

that junction under applied voltage behave like an antenna which radiates this ac current. This current can close itself through quasi particles that is the reason of putting R to its model, which will be discussed in details in the next section. Another important fact is that this ac current causes ac voltage and these ac voltages add up to that dc voltage which one wants to flow through the junction.

1.4.2.3 Magnetic field Effect

For a general shape under the assumption that magnetic field produced by tunneling currents is negligible and the applied field is in the y direction, we can write,

$$\frac{\partial \phi}{\partial z} = \frac{2ed'}{\hbar} B^o \tag{1.10}$$

Here B^o is the field in the insulator region, and, $d' = d + 2\lambda$ where d is the insulator thickness and λ is the penetration depth. By plugging the phase obtained from the above equation into Josephson relation and integrating along y and z coordinates, we get the current per meter width as,

$$I(B^o) = \int_{-\infty}^{\infty} J_c(z) \sin\left[\frac{2ed'B^o}{\hbar} z + \phi(o)\right] dz \tag{1.11}$$

Special Case: As shown in the following figure we consider a rectangular junction with uniform critical current density. In this case, the above current integral ends up to a well known expression,

$$I(B^o) = I_c(0) \left| \frac{\sin\left(\frac{ed'LB^o}{\hbar}\right)}{\frac{ed'LB^o}{\hbar}} \right| = I_c(0) \left| \frac{\sin\left(\frac{\pi\phi}{\phi_0}\right)}{\frac{\pi\phi}{\phi_0}} \right| \tag{1.12}$$

Where the constants in the above equation are defined as $I_c(0) = WLJ_c$, $e/\hbar = \pi/\phi_0$, and $\phi = d'lB^0$. Equation 1.12 is plotted in Figure 1.4 for symmetric junction case. An important observation thus can be concluded by the measurement of maximum zero-voltage, is to find out the uniformity of the junction by comparing

with the symmetry of the sinc function of the form as derived from the above equation. But this test is valid as far we are in the limit of small junction $\left(L/\lambda_j \leq 1\right)$ approximation, where self-field effect is not included.

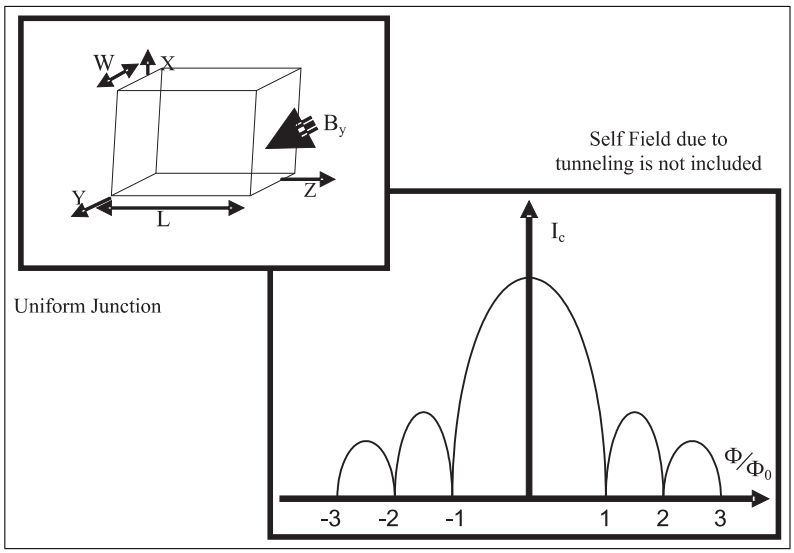

Figure 1.4: Rectangular shape under consideration. Dependence of the maximum zero-voltage current in a junction with a current density of the Fraunhofer pattern for uniform junctions.

Now let's assume the case when we have junctions with higher dimensions compare to λ_j and we face the problem of self-field effect due to the tunneling currents. In this particular case we see that there are two important symptoms of the self-field effect; 1) Current through the junction does not increase indefinitely as the size of the junction is increased, and 2) We don't observe zero in the maximum zero voltage for any applied value of magnetic field. Analysis of such sort of problem requires nonlinear mathematics and can be solved numerically.

1.4.3 Circuit model and the damping characteristics

Whenever we have sufficiently weak coupling between two superconductors, then Josephson relations can be applied as,

$$I = I_c \sin\phi \frac{\partial\phi}{\partial t} = \frac{2e}{\hbar} V. \tag{1.13}$$

Though I_c(T) suffices to characterize the zero voltage dc properties of a weak link for finite voltage situations involving the ac Josephson effect, but we define the junction with its equivalent model when it is required to get complete analysis. Here this section discusses the most famous model, to describe the Josephson junction, named as RCSJ (resistively and capacitively shunted junction) model, in which physical Josephson junction is modeled by an ideal current source, shunted by a resistance R and a capacitance C. This model is shown in Figure 1.5. Resistance R builds in dissipation in the finite voltage regime, without affecting the lossless dc regime, while C reflects the geometric shunting capacitance between the two electrodes and not the capacitance of the electrodes to ground. Capacitance models the presence of displacement current, which flows between the adjacent superconducting electrodes.

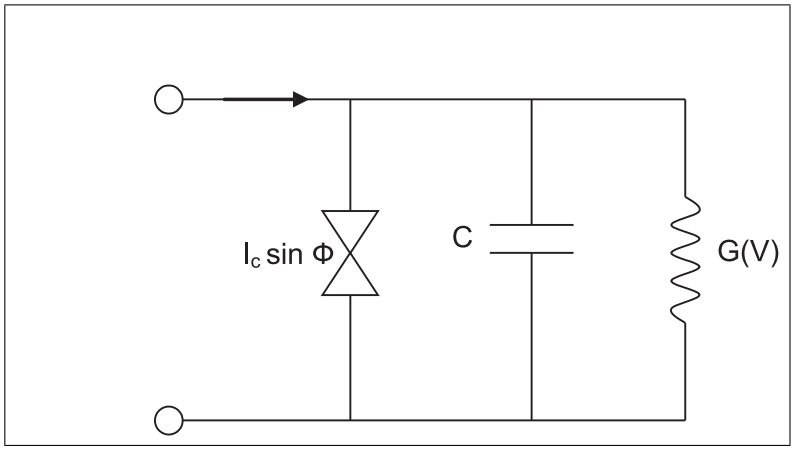

Figure 1.5: Equivalent circuit model for RCSJ .

Considering that above given circuit is biased with a dc current source and according to the analyses of Stewart and McCumber assuming G constant, we can write the differential equation of the above circuit of RCSJ model as,

$$I = I_c \sin\phi + GV + C\frac{dV}{dt}. \tag{1.14}$$

Eliminating V in favor of ϕ, we obtain the second order differential equation,

$$I = \frac{\hbar C}{2e}\frac{d^2\phi}{dt^2} + \frac{\hbar G}{2e}\frac{d\phi}{dt} + I_c \sin\phi. \tag{1.15}$$

If we divide the above equation by I_c and introduce a dimensionless time variables,

$$\theta \triangleq \omega_c t \triangleq (2e/\hbar)\,(I_c/G)\,t \tag{1.16}$$

and

$$\beta_c \triangleq \frac{\omega_c C}{G} \triangleq \left(\frac{2e}{\hbar}\right)\left(\frac{I_c}{G}\right)\frac{C}{G} = Q^2, \tag{1.17}$$

where Q is the quality factor, then we obtain a more simplified expression for the above equation as,

$$\frac{I}{I_c} = \beta_c \frac{d^2\phi}{d\theta^2} + \frac{d\phi}{d\theta} + \sin\phi. \tag{1.18}$$

Where β_c, damping parameter, is the ratio of the capacitive susceptance at that frequency to the shunt conductance. 'ω_c' is called plasma frequency or Josephson angular frequency for a voltage corresponding to the maximum zero-voltage current I_c and the conductance G. As far as $I < I_c$ a static solution to above equation with $\phi = \sin^{-1}(I/I_c)$ and V=0 is allowed, but when $I > I_c$ then only time dependent solution exists. We have two conditions for the later case, "over damped" when C is very small, and "under damped" when C is large.

- **Over damped junction:** We have this condition when C is small enough so that $Q \ll 1$. This reduces the equation 1.18 to first order differential equation of the form,

$$\frac{d\phi}{dt} = \frac{2eI_cR}{\hbar}\left(\frac{I}{I_c} - \sin\phi\right). \tag{1.19}$$

  As can be seen from the above equation, the $d\phi/dt$ is always positive when $I > I_c$. So the phase advances more slowly when $\sin(\phi)$ is positive, and vice versa. Hence to find the $I - V$ relation, first we find the time average voltage by integrating this equation to determine the period of time, T, required for ϕ to advance by 2π. Then using the Josephson frequency relation $2eV/\hbar = 2\pi/T$ we get,

$$V = R\left(I^2 - I_c^2\right)^{1/2}. \tag{1.20}$$

This parabolic dependence for $I > I_c$ and β_c =0 is shown in Figure 1.6(a), where normalized voltage GV/I_c is plotted in relation to normalized current I/I_c.

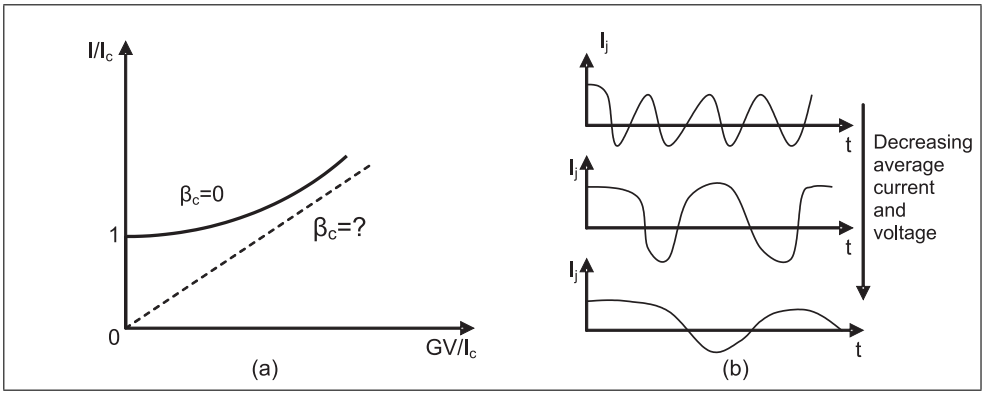

Figure 1.6: (a) Normalized $I - V$ characteristics for a Josephson junction described by RCSJ model under over-damped and under-damped cases. (b) Time dependence of current through the Josephson junction for small β_c at three different points on the $I - V$ characteristic. The average values of these functions measure the difference of the $I - V$ characteristics from that for $\beta_c = \infty$, where only the current through G determines the average voltage.

It is clear that an appreciable amount of dc current is flowing through the Josephson junction at low voltages for $\beta_c = 0$. If the voltage across the junction were dc only, there would be only a sinusoidal ac current. This ac current in the junction passes through the shunt conductance as the source has infinite impedance. It thus produces an alternating voltage across the junction, so the rate of change of phase is no longer constant. Then the result is a complex temporal variation of current; as seen by averaging

$$V = (2\pi/\Phi_0)\, {}^{d\phi}/_{dt} \tag{1.21}$$

over one period, which has a periodicity equal to the Josephson frequency equivalent of the average voltage. Figure 1.6(b) shows how the current becomes increasingly non sinusoidal as the voltage approaches zero.

- **Under damped Junction:** This condition which is much complex than the previous one arises when C is large enough so that $Q > 1$. In this case $I - V$ curve becomes hysteretic meaning that there is a range of current

$I_{min} > I < I_c$ in which there are two values of voltages, $V = 0$ and $V \neq 0$. So upon increasing I from zero, V=0 until I_c, at which point V jumps discontinously up to a finite voltage V, corresponding to a running state, in which the phase difference increases at the rate $2eV/\hbar$. On the way back if I is reduced below I_c, V does not drop back to zero until a retrapping current $I_r \approx 4I_c/\pi Q$ is reached. Hysteretic $I-V$ curve of an under damped Josephson junction is shown in Figure 1.7 with two different schematics for detailed understanding [31].

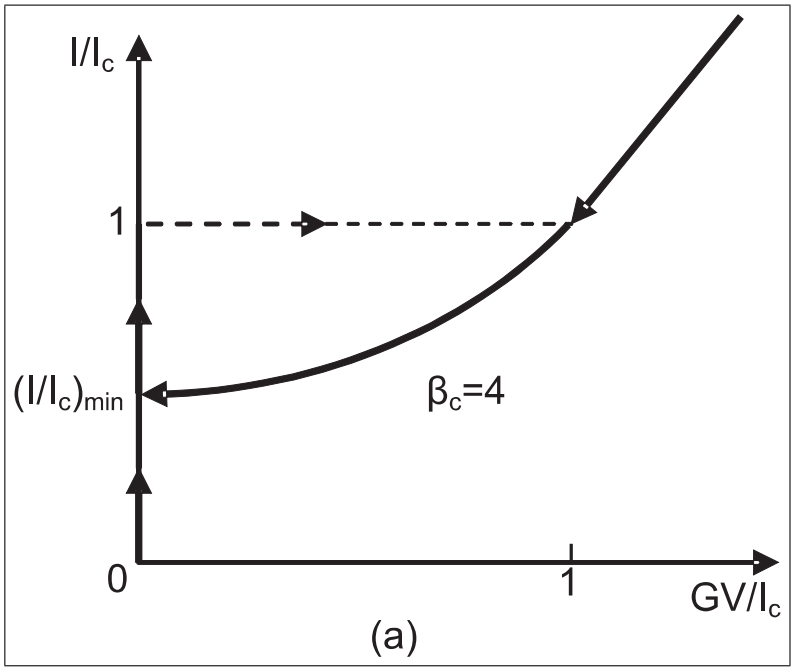

Figure 1.7: Normalized $I - V$ characteristic for a junction with $\beta_c = 4$.

1.5 Superconducting Quantum Interference Devices (SQUID)

1.5.1 rf-SQUID

The rf-SQUID consists of a single Josephson junction integrated into a superconducting loop that is inductively coupled to the inductance L_T of an LC resonant

(tank) circuit [Fig. 1.8(a)]. The tank circuit is driven by an rf current, and the resultant rf voltage is periodic in the flux applied to the SQUID with period Φ_0. Detailed reviews on rf-SQUIDs have been written by many authors (for example, Jackel and Bhrman, 1975; Ehnholm, 1977; Likharev and Ulrich, 1978; Likharev, 1986; Ryhanen et al., 1989; Clarke, 1996).

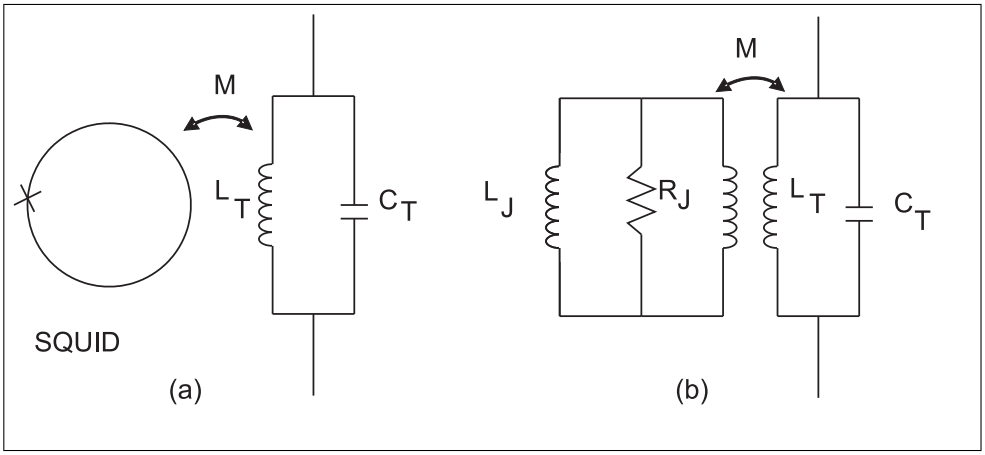

Figure 1.8: a) SQUID coupled to the tank circuit via a mutual inductance M. b) Equivalent circuit of SQUID coupled to the tank circuit.

The total flux Φ_T in rf-SQUID is related to the applied flux Φ by

$$\Phi_T = \Phi - LI_0 \sin(2\pi\Phi_T/\Phi_0). \tag{1.22}$$

We see immediately that Eq. 1.22 can exhibit two distinct kinds of behaviors. For $\beta_L' = 2\pi LI_0/\Phi_0 < 1$, the slope $d\Phi_T/d\Phi = [1 + \beta_L' \cos(2\pi\Phi_T/\Phi_0)]^{-1}$ is everywhere positive and the Φ_T vs Φ curve is nonhysteretic. On the other hand, for $\beta_L' > 1$, there are regions in which $d\Phi_T/d\Phi$ is positive, negative, or divergent so that the Φ_T vs Φ curve becomes hysteretic. Radio frequency superconducting quantum interference devices have been operated in both modes. In the hysteretic mode the SQUID makes transitions between quantum states and dissipates energy at a rate that is periodic in Φ. This periodic dissipation in turn modulates the quality factor Q of the tank circuit, so that when it is driven on resonance with a current of constant amplitude, the rf voltage is periodic in Φ. In the case $\beta_L' < 1$, the nondissipative mode, the SQUID behaves as a parametric inductance, modulating the effective inductance and hence the resonance frequency

of the tank circuit as the flux is varied. Thus when the tank circuit is driven at constant frequency, the variations in its resonant frequency cause the rf voltage to be periodic in Φ.

Historically, it appears that most low-T_c rf-SQUIDs were operated in the hysteretic mode, although as we shall see, there are advantages to the nonhysteretic mode. However, the theory of noise in the nondissipative regime was worked out in the late 1970s, just as dc-SQUIDs began largely to replace rf-SQUIDs. As a result, the importance of the nonhysteretic rf-SQUID was not widely exploited experimentally. The advantage of 77K operation has changed this situation dramatically, largely due to the systematic experimental effort of the group at J*ü*lich and the very recent theoretical work of Chesca (1998). In the following two sections we briefly outline the theory of the dissipative and nondissipative rf-SQUIDs.

1.5.1.1 Effects of the parametric Inductance

In the limit of zero bias, the Josephson element can be described in terms of a parametric inductance. When the junction is inserted in the superconducting loop, its behavior affects the total inductance of the loop. In the case of small signal variation, that is, when the amplitude of the time varying component of the applied flux is small compared to the flux quantum Φ_0, the expression of the effective inductance L_{eff} of the system can be obtained directly from the static characteristics. In fact, in this approximation, following Silver and Zimmerman (1975, 1976), we can define

$$L_{eff} = -\frac{d\Phi_e}{di}. \tag{1.23}$$

Deriving this equation with respect to i and plugging in the fact that $i = -I_1 \sin 2\pi\frac{\Phi}{\Phi_0}$, we get the expression for junctions equivalent inductance as;

$$L_J(\Phi) = \frac{L}{\beta_e \cos(2\pi\Phi/\Phi_0)}. \tag{1.24}$$

The effect of the parametric inductance can be observed by coupling the

SQUID to a tank circuit of inductance L_T and capacitance C_T (see Fig. 1.8 (a))

If L is the inductance of the superconductor loop, the system can be described by the equivalent circuit of Figure 1.8(b) (Goodkind and Stolfa 1970). The weak link is represented by the parametric inductance L_J being small enough to "shunt" the capacitance of the link. In terms of the resistively shunted model, this implies that the parameter $\beta_J = 1/\omega_J C R_J$ is much greater than 1. The effective inductance of the tank circuit coupled to the SQUID, computed using the equivalent circuit of Figure 1.8, is given by

$$\tilde{L}_T = L_T \left[1 - \kappa^2 \frac{L}{L_J(\phi) + L}\right], \tag{1.25}$$

where κ is the coupling coefficient defined by

$$M^2 = \kappa^2 L_T L \tag{1.26}$$

and $\phi = \Phi/\Phi_0$.

Let us assume that $\beta_L \ll 1$. In such a case Φ can be approximated by Φ_e and therefore effective inductance becomes

$$\tilde{L}_T = L_T \left[1 - \frac{\kappa^2}{1 + (1/\beta_L \cos 2\pi\phi_e}\right] \simeq L_T(1 - \kappa^2 \beta_L \cos 2\pi\phi_e). \tag{1.27}$$

The effective tank circuit inductance, because of its coupling to the SQUID, is a periodic function of the magnetic flux ϕ_e coupled to the loop. This dependence can be observed by measuring the variation of the effective resonance frequency of the tank circuit $\tilde{\upsilon} = 1/(\tilde{L}_T C_T)^{1/2}$ as a function of the applied magnetic field (Silver and Zimmerman 1967). A different method for observing the effect of the parametric inductance in the limit of $\beta_L \ll 1$ has been more employed by Pascal and Sauzade (1974). The authors have analyzed the noise spectrum of a preamplifier connected to the tank circuit. The pre-amplifier was working at a temperature of 4.2K. The frequency, at which the peak in the noise spectrum occurs, varies with the applied flux Φ_L.

For $\beta_L > 1$, the situation is rather different. The static characteristics are then hysteretic. The contribution of L_J becomes negligible compared to the right geometrical inductance L. This circumstance can be easily verified by looking at L_{eff} and by observing that on increasing B_L the stable branches of the i vs. Φ_L dependence approach progressively straight lines. However, at the edges of these regions where transitions between different branches occur, the shape of the curve changes. This effect is more evident for B_L, not much greater than 1. The same argument holds for the Φ vs. Φ_L dependence. In fact, deriving $\Phi = \Phi_L + L_i$ with respect to Φ_L we get

$$\frac{d\Phi}{d\Phi_L} = 1 + L\frac{di}{d\Phi_e}. \tag{1.28}$$

Combining the last expression with L_{eff} results in,

$$\frac{d\Phi}{d\Phi_L} = 1 - \frac{L}{L_{eff}(\phi)}. \tag{1.29}$$

Therefore the slope of the Φ vs. Φ_e curve is related to the effective inductance L_{eff} of the device. The change in this slope can be detected (Pascal and Sauzade 1974) by biasing the tank circuit by a slow varying sawtooth current with a superimposed rf signal of small amplitude. The rf signal, V_T, detected across the tank circuit is proportional to $d\Phi/dt$ and therefore to $d\Phi/d\Phi_e$. The slowly varying signal is proportional to the quasi static flux.

1.5.1.2 Operational modes of rf-SQUID

rf-SQUID in Hysteretic mode (Dispersive Mode): For the case $\beta'_L > 1$, the unstable nature of the Φ_T vs. Φ curve in Figure 1.9(a) causes the SQUID to make transitions between stable quantum states as Φ is changed [Fig. 1.9(b)].

For example, when Φ is increased from 0, there is a transition from the $k = 0$ flux state to the $k = 1$ state at a critical flux (neglecting fluctuations) $\Phi_c = LI_0$. In rf operation, a current I_{rf} sin$\omega_{rf}(t)$ is applied to the resonant circuit. The

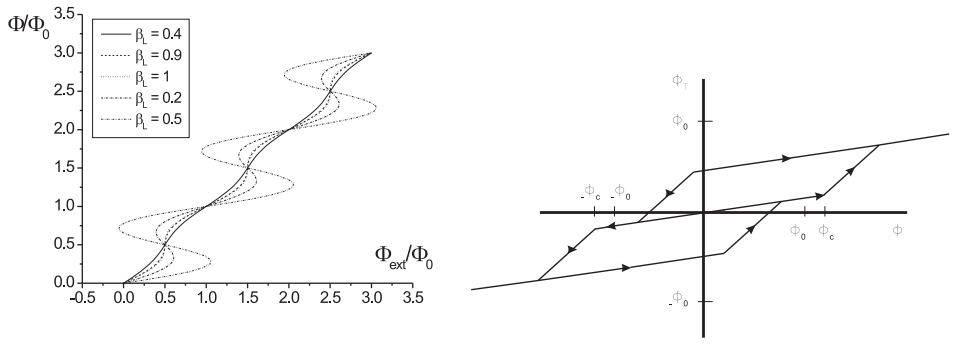

(a) (b)

Figure 1.9: The rf-SQUID: (a) Normalized total flux Φ_T/Φ_0 vs normalized applied flux Φ/Φ_0 for different β_L' values. (b) Total flux Φ_T vs. applied flux Φ for rf-SQUID with $LI_0/\Phi_0 = 5/4$, showing transitions between quantum states in absence of thermal noise as Φ is increased and subsequently decreased.

peak voltage V_T across the resonant circuit increases linearly with I_{rf} until, for $\Phi = 0$, $I_{rf} = \Phi_c/MQ$, at which value

$$V_T^{(0)} = \omega_{rf} L_T \Phi_c / M, \tag{1.30}$$

where $M = \kappa(LL_T)^{1/2}$. At this point [A in Figure 1.10] the SQUID makes a transition to the $k = +1$ or -1 state. As the SQUID traverses the hysteresis loop, energy ΔE is extracted from the tank circuit. Because of this loss, the peak flux on the next half cycle is less than Φ_c, and no transition occurs. The tank circuit takes many cycles to recover sufficient energy to induce a further transition, which may be into either the $k = +1$ or -1 state. If we now increase I_{rf}, transitions are induced at the same values of I_T and V_T but, because energy is supplied at a higher rate, the stored energy builds up more rapidly after each energy loss ΔE, and transitions occur more frequently. At B, a transition is induced on each positive and negative rf peak, and a further increase in I_{rf} produces the "riser" BC. At C, transitions from the $k = \pm 1$ states to the $k = \pm 2$ states occur, and a second step begins. A plot of the peak values $V_T^{(0)}$ vs I_{rf} produces the "steps and risers" shown in Figure 1.10. If we now apply an external flux $\Phi_0/2$, the

hysteresis loops in Figure 1.9(b) are shifted by this amount, and one finds

$$V_T^{\pm 1/2} = \omega_{rf} L_T \left(\Phi_c - \Phi_0/2\right)/M. \tag{1.31}$$

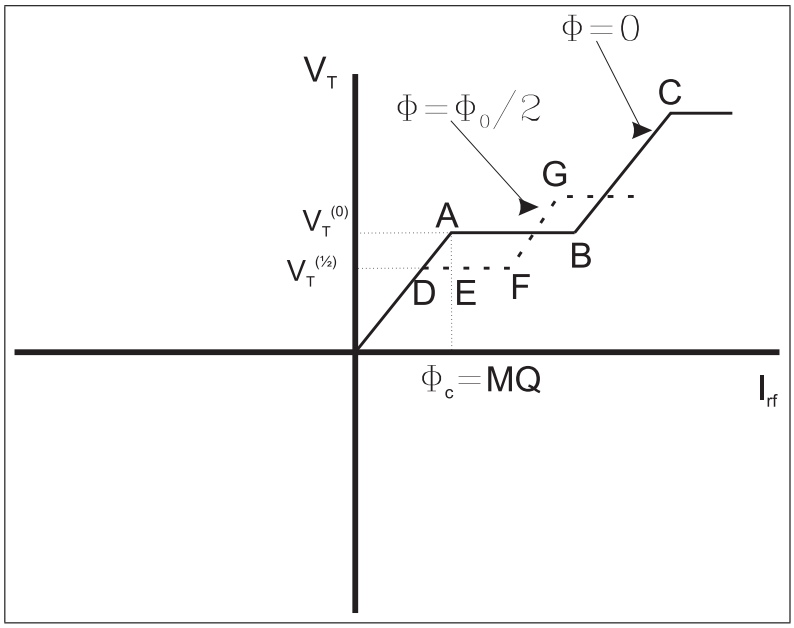

Figure 1.10: Peak rf voltage, V_T, across tank circuit vs. peak rf current, I_{rf}, in absence of thermal noise for $\Phi = 0$ (solid line) and $\Phi = \pm\Phi_0/2$ (dashed line).

As I_{rf} is increased, this voltage remains constant until the point Φ, at which the SQUID traverses the hysteresis loop corresponding to the $k = 0 \rightarrow k = +1$ transitions once per rf cycle. A further increase in I_{rf} produces the riser FG; at G, corresponding to a peak rf flux - $(\Phi_c + \Phi_0/2)$, transitions $k = 0 \rightarrow k = -1$ begin. Thus an applied flux other than $n\Phi_0$ (n is an integer) causes the step AB to split as shown in Figure 1.10.

The model outlined above enables us to calculate the transfer function at values of I_{rf} that maintain the SQUID biased on a step: the change in V_T as we increase Φ from 0 to $\Phi_0/2$ is $V_T^{(0)} - V_T^{(\pm 1/2)} = \omega_{rf} L_T \Phi_0/2M$, so that for small changes in flux in the range $0 < \Phi < \Phi_0/2$ we find $V_\Phi = \omega_{rf} L_T/M$. At first sight, this result seems to imply that V_Φ can be increased indefinitely by reducing κ. This is not the case, since one must ensure that the point F in Figure 1.10 lies to the right of E, that is, DF must exceed DE. To calculate DF we note that the power dissipated in the SQUID is zero at D and approximately $I_0\Phi_0\omega_{rf}/2\pi$ at F,

since the energy dissipated per rf cycle is approximately $I_0\Phi_0$ for a device with $LI_0 \approx \Phi_0$. Thus, taking account of the fact that the rf currents and voltages are peak values, we find $(I_{rf}^{(F)} - I_{rf}^{(D)}) = V_T^{(\pm 1/2)}/2 \approx I_0\Phi_0\omega_{rf}/2\pi$. Furthermore, we can easily see that $I_{rf}^{(E)} - I_{rf}^{(D)} = \Phi_0/2MQ$. Assuming $LI_0 \approx \Phi_0$ and using Eq. 1.31, we can write the requirement that DF exceeds DE in the form $\kappa^2 Q \geq \pi/4$. Taking $\kappa \approx 1/Q^{1/2}$, we find that the expression for V_Φ becomes

$$V\Phi \approx \omega_{rf}(QL_T/L)^{1/2} \approx \omega_{rf}(L_T/L)^{1/2}/\kappa. \tag{1.32}$$

We note that Φ_F scales with $\omega_r f$ and as $L^{-1/2}$. Detailed theories have been developed for noise in the hysteretic rf-SQUID operating at liquid Helium temperatures (Kurkijärvi, 1972, 1973; Jackel and Buhrman, 1975; Giffard et al., 1976; Ehnholm, 1977; Hollenhorst and Giffard, 1980; Ryhänen et al., 1989). Although in a noise-free model the steps are flat, thermal noise causes them to tilt to a slope η. In addition, thermal noise induces voltage noise on the step arising from fluctuations in the value of flux, at which transitions between flux states occur. The corresponding intrinsic flux noise of the SQUID is (Kurkijä rvi, 1973).

$$S_\Phi^i(f) \approx \frac{(LI_0)^2}{\omega_{rf}} \left(\frac{2\pi k_B T}{I_0\Phi_0}\right)^{4/3}. \tag{1.33}$$

In the case of Helium-cooled rf-SQUIDs, in which the tank circuit voltage is detected with a room-temperature amplifier, there is a second, extrinsic contribution to the flux noise. This arises in part because the noise temperature of the rf amplifier is above the bath temperature and in part because a fraction of the coaxial line connecting the tank circuit to the amplifier is at room temperature. We can represent these two contributions by an effective noise temperature T_a^{eff}, enabling us to write the noise energy due to intrinsic and extrinsic noise sources as (Jackel and Buhrman, 1975; Giffard et al.,1976);

$$\varepsilon \approx \frac{LI_0^2}{2\omega_{rf}} \left(\frac{2\pi k_B T}{I_0\Phi_0}\right)^{4/3} + \frac{2\pi\eta k_B T_a^{eff}}{\omega_{rf}}. \tag{1.34}$$

Equation 1.34 makes two important points. First, scales as $1/\omega_{rf}$, up to a limiting value R/L. Second, for low-T_c SQUIDs, the extrinsic noise energy generally dominates the intrinsic noise: if we take the representative values T= 4 K, $\Gamma = 0.1$, $\eta = 0.2$, $\beta'_L = 2\pi$, and $T_a^{eff} = 100K$, we find that the extrinsic noise energy is about 20 times the intrinsic value. Thus, although we should be wary of extrapolating these results to 77 K, where to our knowledge, there are no simulations or calculations, the overall noise energy of the hysteretic rf-SQUID should not increase very much as we raise the temperature from 4 K to 77 K. This result is in contrast to the dc-SQUID, which for properly designed circuitry is limited largely by intrinsic noise at 4.2 K, so that the overall noise energy will increase significantly as the temperature is raised to 77 K.

rf-SQUID in Nonhysteretic mode (Dissipative mode): To give an approximate account of the operation of the nonhysteretic rf-SQUID, we follow the description of Hansma (1973), which is valid in the limits $\beta'_L \ll 1$, where the total magnetic flux threading the SQUID is nearly equal to the applied flux, and $\omega_{rf} \ll I_0 R/\Phi_0$. More general treatments are given, for example, by Jackel and Buhrman (1975), Erne et al. (1976), Danilov et al. (1980), Likharev (1986), and Ryhänen et al. (1989).

In the presence of a static flux Φ and rf flux Φ_{rf} sinωrft, the current in the SQUID loop is

$$\begin{aligned} &I = I_0 \sin\left[(2\pi/\Phi_0)\left(\Phi + \Phi_{rf}\sin\omega_{rf}t\right)\right] \\ &(2\pi L I_0 \ll \Phi_0). \end{aligned} \tag{1.35}$$

The oscillating component of this current induces a current $I_i = -(M/Z)dI/dt$ into the tank circuit, where $Z = R_T + i[\omega_{rf}(L_T - M^2/L) - 1/\omega_{rf}C_T]$ is its impedance; the inductance of the tank circuit is modified by the contribution $-M^2/L$ from the SQUID. If we assume that the rf frequency is near resonance and that Q is reasonably large, we can neglect all frequency components other than the fundamental. Expanding the right-hand side of Eq. 1.35 in terms of the Bessel function J_1, we find the induced current as,

$$\mathrm{I_i} = \frac{2\kappa^2 Q L I_0}{M(1+\delta^2)^{1/2}} \cos\left(\frac{2\pi\Phi_{rf}}{\Phi_0}\right) J_1\left(\frac{2\pi\Phi_{rf}}{\Phi_0}\right) \sin(\omega_{rf}t - \theta). \tag{1.36}$$

Here, $\delta = 2[(\omega_{rf} - \omega_0)/\omega_0]Q$ is the normalized difference between the rf frequency and the tank-circuit resonant frequency Φ_0 , and $\theta = tan^{-1}\delta + \pi/2$.

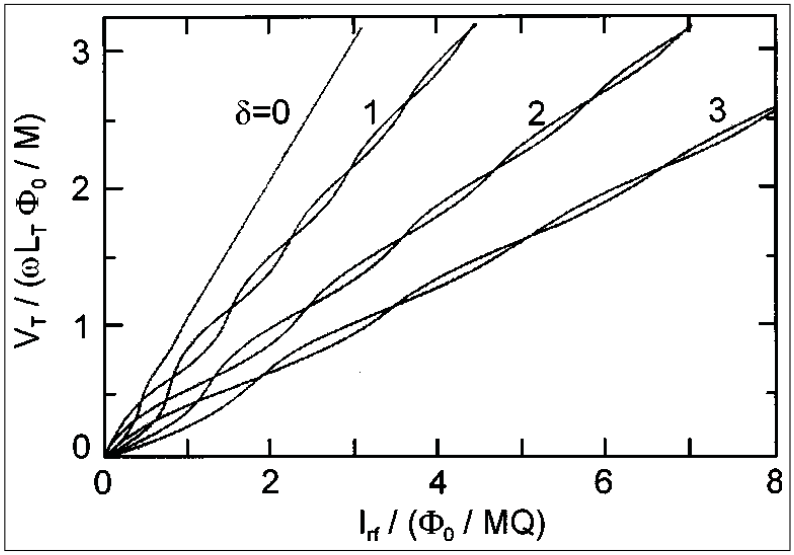

Figure 1.11: Tank circuit voltage, V_T, vs rf drive current I_T for four values of the tuning parameter $\delta = [2(\omega_{rf} - \omega_0)/\omega_0]Q$ and for $\Phi = 0, and \Phi_0/2$. Curves plotted for $\kappa^2 Q\beta'_L = \pi/2$ (Hansma, 1973).)

The rf flux applied to the SQUID is $MI_T \sin\omega_{rf}t$, where I_T is the amplitude of the total current in the inductor, which in addition to the induced current given by Eq. 1.36, also contains a component of amplitude $QI_{rf}/(1+\delta^2)^{1/2}$ produced by the external rf current. From Eq. 1.36 we see that the total current leads the induced current by a phase angle θ. The amplitudes of the total and external rf currents are related by

$$I_{rf} = \frac{(1+\delta^2)^{1/2}}{Q} \left\{ \left[\frac{2\kappa^2 Q L I_0}{(1+\delta^2)^{1/2} M} \cos\left(\frac{2\pi\Phi}{\Phi_0}\right) \times J_1\left(\frac{2\pi M I_T}{\Phi_0}\right) + I_T \cos\theta \right]^2 + I_T^2 \sin^2\theta \right\}^{1/2}. \tag{1.37}$$

Figure 1.11 shows plots of V_T vs I_{rf} for $\Phi = 0$ and $\Phi_0/2$ for four values of the tuning parameter δ. We see that the response is insensitive to the flux in the SQUID for $\delta = 0$; thus the tank circuit for the nonhysteretic SQUID is operated

off resonance. For a given value of δ, the response shows a series of oscillations as I_{rf} is increased, arising from the oscillations of the Bessel function. The maximum peak-to-peak modulation of V_T at fixed I_{rf} is of the order of $2\kappa^2 QLI_0(\omega_{rf}L_T/M)$, so that,

$$\begin{aligned} V_\Phi &\approx (2/\pi)\,\kappa^2 Q\beta'_L\omega_{rf}L_T/M \\ &\approx (2/\pi)\,(\kappa^2 Q\beta'_L)\omega_{rf}(L_T/L)^{1/2}/\kappa. \end{aligned} \tag{1.38}$$

This transfer function exceeds that of the hysteretic rf-SQUID [Eq. 1.38] by a factor of order $\kappa^2 Q\beta'_L$, which can be made larger than unity for the nonhysteretic case by choosing $\kappa^2 Q \gg 1$.

The intrinsic noise energy of low-T_c nonhysteretic rf-SQUIDs has been calculated by several authors, and is approximately $3k_BT/(\beta'_L)^2\omega_c$ (Likharev, 1986), where the drive frequency is set equal to $\omega_c = R/L$, the cutoff frequency of the SQUID. A noise energy as low as $20\hbar$ has been achieved by Kuzmin et al. (1985).

As a preamble to the discussion of nonhysteretic high-T_c SQUIDs, we note that Falco and Parker (1975) successfully observed flux modulation in an rf-SQUID at 2K with a supercurrent as low as 50 nA. The corresponding value of the noise parameter $\Gamma = 2\pi k_BT/I_0\Phi_0$ was about 1.7; at this high value, they were unable to observe any trace of supercurrent in an isolated junction. Thus it is evident that one can expect to operate an rf-SQUID with substantially higher values of Γ than is the case for the dc-SQUID (see Sec. II.C). Although this important fact has been known experimentally for many years, only very recently has the work of Chesca (1998) provided a quantitative explanation. In contrast to previous theories of the rf-SQUID in which one regards thermal noise as a perturbation on a noise-free system, Chesca solves the Smoluchowski equation for the situation, in which thermal fluctuations dominate. Thus both the signal produced by the SQUID and the noise are found in a unified calculation that yields analytical results. For the case $\beta'_L \leq 1$ and $\omega_{rf} \ll R/L$, Chesca finds;

$$\varepsilon \approx 3\Gamma^2\left(1 + \frac{T_k}{T}\frac{1}{\kappa^2 Q}\frac{R/L}{\omega_{rf}}\right)\frac{\exp(L/L'_{th})}{L/L'_{th}}\frac{k_BTL'_{th}}{R}. \tag{1.39}$$

Here, $L'_{th} = (\Phi_0/2\pi)^2/k_BT$ and T_k is the effective noise temperature of the tank circuit, including any contribution from the pre-amplifier. If one assumes $L/L'_{th} = \beta'_L\Gamma \ll 1$ and that k^2Q can be made sufficiently large that $(|T_k|/T)(R/\omega_{rf}L)/\kappa^2Q \ll 1$, Eq. 1.39 can be written in the alternative forms of,

$$\begin{aligned} \varepsilon &\approx 3k_BT/(\beta'_L)^2(R/L) \quad (a) \\ &\approx 3k_BT\Phi_0/2\pi\beta'_LI_0R. \quad (b) \end{aligned} \tag{1.40}$$

Interestingly, Eq. 1.40(a) is identical to the result found perturbatively for the rf-SQUID for low values of Γ. The value for ε in Eq. 1.40(b) is equal to $3/4\pi\beta'_L(1+\beta_L)$ times that for the dc-SQUID in the limit $\Gamma\beta_L < 0.2$.

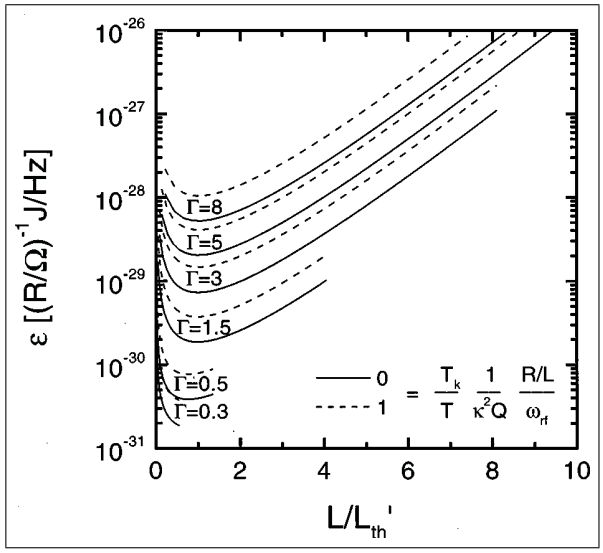

Figure 1.12: ϵ vs. L/L_th' for nonhysteretic rf-SQUID at 77K (chesca, 1998).

Equation 1.39 is plotted in Figure 1.12 for the two cases $(|T_k|/T)(1/\kappa^2Q)(R/\omega L_{rf}) = 0$ and 1, and for six values of Γ. One concludes from these plots that the optimal values are (Chesca, 1998),

$$\beta'_L = 1 \quad if \quad \Gamma \leq 1, \tag{1.41}$$

$$\beta'_L = 1/\Gamma \quad if \quad \Gamma > 1. \tag{1.42}$$

We note that for the lowest value of Γ plotted, 0.3, the curve is cut off at $\beta'_L\Gamma = L/L'_{th} = 0.55$, at which value the noise energy approaches $10^{-31}4JHz^{-1}$ for $R = 1\Omega$. For the case $\Gamma \geq 1$, the noise energy is higher and the optimal SQUID inductance is approximately $L_t h' \approx 100pH$ at 77 K. Again, this value is about two times higher than for the dc-SQUID at 77 K. One consequence of this result is that one can expect to use rf-SQUIDs with an area about two times higher than dc-SQUIDs.

1.5.2 dc-SQUID

It is the most common type of SQUIDs. The dc-SQUID is shown in figure 1.13. Here without going into detailed analysis of the operation, like in rf-SQUID case, we will present in simple words the working principle of the dc-SQUID. The dc-SQUID contains two nearly identical RSJ junctions connected in parallel to a bias current source.

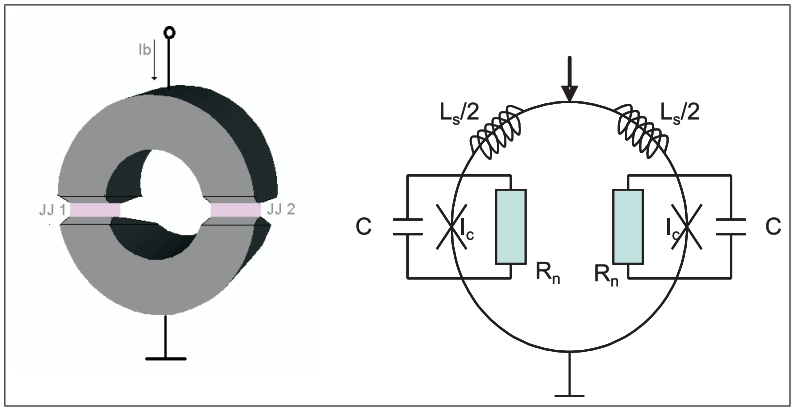

Figure 1.13: The dc-SQUID: the symbol (left) and the equivalent circuit (right).

The bias current, I_b, is usually chosen such that the critical current of each junction is slightly exceeded, $I_b > 2I_c$, and a corresponding voltage drop, V, can be measured across these junctions. When external (measured) magnetic flux Φ_{ext} tries to enter the loop, additional circulating current $I = -\Phi_{ext}/L_s$ is induced in the ring, adding to the bias in one junction while, subtracting in the other. With increasing Φ_{ext}, junction phases are switching alternately, and I is reversing

direction at each $\Phi = \Phi_0/2$, i.e., $I = \Phi_0/2L_s$. The V changes accordingly so that the current-voltage $(I-V)$ curve measured across the two parallel junctions is alternating between two extreme traces: upper one, corresponding to $\Phi = n\Phi_0\,(n = 0, 1, 2, 3, ...)$ and lower one corresponding to $(n + 1/2)\Phi_0$, as shown in Figure 1.14. The voltage drop change ΔV across a dc-SQUID is thus a periodic function of Φ_{ext} with the period equal to Φ_o. In the simplest approximation, the peak-to-peak amplitude of this SQUID output signal is $\Delta V = (\Phi_0 R_n)/(2L_s)$, with R_n denoting the ohmic resistance of the Josephson junction in its normal conducting state (in Figure 1.14, the slope of the dashed line gives the resistance of two junctions in parallel, i.e., $R_n/2$). In the FLL mode, the SQUID is operated at the steepest part of the $V - \Phi_{ext}$ curve. The transfer coefficient is thus:

$$V_\Phi = |\delta V/\delta\Phi|_{I_b} \cong \Delta V/(\Phi_0/2) = R_n/L_s \tag{1.43}$$

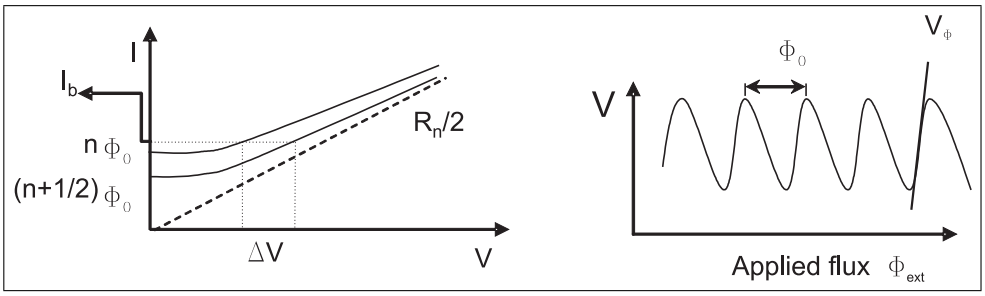

Figure 1.14: The current voltage characteristics at low extreme flux values (left) and output voltage vs. applied flux (right).

Figure 1.14 makes it clear that the SQUID measures the flux changes starting from an arbitrary initial voltage state. The principles of the feedback electronics providing for the FLL null detector operation, and usually permitting one to resolve a flux change of 10^{-6} to $10^{-7}\Phi_0$.

The additional $1/f$ noise contribution of the SQUID itself becomes significant at lower signal frequencies. It originates from the junctions critical current fluctuations and from thermally activated hopping of flux vortices (quanta) which penetrate the SQUID body, including the junction electrodes. The current fluctuations and the flux hopping are acceptably low at very low temperatures. However, both of these $1/f$ noise sources become quite significant at 77K. Fortunately, noise due to critical current fluctuations can be removed by periodically reversing

the direction of the dc current bias [32]. There is no such universal method of suppression the vortex hopping. However, one can try to prevent flux penetration into the SQUID body, pin it once penetrated, and expel by heating above the critical temperature or by demagnetization. With a suitable bias reversal circuit, the crossover frequency from thermal (white) to $1/f$ noise can still be as low as 1 to 10Hz, even at 77K.

1.5.3 rf-SQUID configurations

1.5.3.1 Magnetometer

In most magnetometric applications the task is to measure the local intensity of magnetic field $B = \Phi/A$, and of its gradients. Here, A is the area, over which the flux is collected. Bold font indicates a vector quantity. To measure very small B sensitively, in the range of fT range, one needs a relatively large A, say, of the order of cm^2 or even mm^2. Hence, SQUID magnetometers must include flux pickup structures (flux antennae) having a sufficiently large effective area, A_{eff}. In the simplest and most typical case, only one component of the field vector is measured. The effective area of a SQUID coupled to any flux concentrating structure is $A_{eff} = \Phi_e/B_m$, where B_m is the measured field component and Φ_e is the flux which the field focusing structure can concentrate into the SQUID hole. The low-inductance SQUID loop alone has a very small A_{eff}, of the order of 10^{-4} to 10^{-2} mm^2, which is not sufficient in most cases. Here, we note also the conflicting requirements of having L_s as small as possible for low SQUID noise, but a large A_{eff}, thus a correspondingly large L_s, for good field sensitivity. The various solutions seeking to resolve that conflict all consist of collecting Φ over a large area, and coupling it more or less effectively to the very small SQUID hole. In thin film technology, the simplest solution is to make outer dimensions of the SQUID loop much larger than the loop's hole. This is in order to concentrate into that hole a fraction of the flux expelled by the superconductor. This is the so called washer SQUID. Much higher A_{eff} per unit area can be obtained using planar or hybrid (with three dimensional wire-wound pickup coils) flux

transformers [33], [34].

Generally, A_{eff} is the figure of merit of a magnetometer pickup structure. The magnetic field spectral resolution (field noise) of a magnetometer is:

$$B_N = S_\Phi(f)^{1/2} \Big/ A_{eff} = (\delta B/\delta\Phi)\, S_\Phi(f)^{1/2} \tag{1.44}$$

where $(\delta B/\delta\Phi) = 1/A_{eff}$ is the field-to-flux transformation coefficient, usually quote in units on nT/Φ_0. The concept of A_{eff} can also be extended to gradiometers.

1.5.3.2 Gradiometers

In many applications, one needs to measure field gradients or to detect very weak signals from localized sources against a background of magnetic disturbances (magnetic noise), which are orders of magnitude stronger, but more uniformly distributed in space, like, e.g., the fields of power lines. In such cases, the use of gradiometers is an alternative to magnetic shielding. The 1^{st} and higher spatial gradients are obtained by spatial differentiation of field along spatial coordinates. for example the 1^{st} and k^{th} gradient components are given by;

1st gradient:

$$G_{ij} = \frac{\delta B_i}{\delta x_j} \qquad i, j = 1, 2, 3 \tag{1.45}$$

k-th gradient:

$$G_{j_1 j_2 \ldots j_k j_{k+1}} = \delta^k B_{j_1} \Big/ \prod_{p=2}^{k+1} \delta x_{j_p} \qquad j_p = 1, 2, \text{or } 3 \text{ for } p = 1, \ldots \text{k} + 1 \tag{1.46}$$

In the case of first order gradients, there are components of magnetic field and spatial coordinates. Hence, the 1^{st} order gradient is a 9-component tensor. However, because $divB = 0$ the first gradient tensor is traceless, and because

$curlB = 0$, the tensor is symmetrical and there are only five linearly independent components of the tensor. Similarly, the 2nd order gradient is a $3 \times 3 \times 3 = 27$ components tensor, which due to the same symmetry properties has only 7 linearly independent components. Generally, a gradient of order k has $3+2K$ independent components, which need to be independently measured [35].

The measurement of flux (field) gradients always requires measuring flux (field) values at different locations. Subtraction of these values directly in the pickup structure, before feeding the difference to the SQUID, is the traditional and effective approach to determine one component of the tensor. The polarity is controlled by the coil orientation. When different weights are required at different locations, the corresponding coils can have different numbers of turns (at least in the 3D wire construction).

The gradiometer of order k can also be formed synthetically from a combination of magnetometers can lower order gradiometers of orders less than k. Each component of a synthetic gradiometer is connected to an individual SQUID sensor and the individual outputs are combined synthetically (in the software) to yield and construct the desired gradiometer order. The synthetic gradiometers allow one to obtain more complex configurations that the hardware gradiometers do. But they impose more stringent conditions on the characteristics of the SQUID system such as the dynamic range, slew rate, and linearity.

The synthetic gradiometers are a special case of synthetic systems. In synthetic systems, the sensor and reference signals are recorded separately and are linearly combined by digital processing. The coefficients of this linear combination determine the behavior of the synthetic system and can be designed to meet a variety of criteria, for example, to minimize a norm of the resulting signal (adaptive system), or to construct higher-order gradiometers. The synthetic systems are quite flexible, because results with different characteristics can be obtained from the same sensor and reference data.

The effective area of a gradiometer is a concept sometimes used to characterize

gradiometers, especially of first order type. In analogy to the magnetometer case:

$$1/A_{eff} = (\delta G_{ij}/\delta\Phi)\, b^{-1} \tag{1.47}$$

where b is the baseline. For the first order: $A_{eff,parallel} = 2A_{eff,serial}$.

1.5.3.3 Inductance and Effective Area calculation for single layer devices

Inductance calculation: Single layer magnetometer and gradiometer sensors are of current interest only when operation at or near 77K is intended. This interest is motivated by the immaturity of the present HTS multi-layer technology. The single layer designs usually borrow from concepts proven earlier in the LTS devices. The washer structures with a slit, mentioned I.D., function as a flux focuser [36] and are the simplest single-layer magnetometer structure usable for HTS. Two variants of a square-washer structures are shown in Figure 9, one suitable for dc-SQUID (a) and another (b) for rf-SQUID.

Generally, the inductance of a SQUID washer is a sum of the inductance of the hole, of the slit, and of the (parasitic) inductance of the junction(s), which usually can be neglected. For the HTS SQUID, kinetic components of the hole and slit inductances may not be negligible, due to the large London penetration depths, λ_L, of the HTS material. Since the rf-SQUID washer needs to be much larger than the dc one (outer edge of the order of mm to insure inductive coupling to the rf tank circuit), the inductance of the slit would be excessive for optimum β_L, or even for the SQUID operation when $L_s \gg L_f$. The geometric inductance of a washer SQUID with square or round hole is:

$$\text{Square}: L \cong 1.25\mu_0 d \times 10^{-8} \ \text{[pH]} \tag{1.48}$$

and

$$\text{Round}: L \cong \mu_0 d \times 10^{-8} \ \text{[pH]} \tag{1.49}$$

where $\mu_0 = 4\pi \times 10^{-7}$H/m is the permeability of free space and d is the square

hole edge or the round hole diameter in μm. This expression is valid when the loop with $w = (D-d)/2 > d$, where D is the outer edge or diameter of the washer [36]. When $w < d$, i.e., for narrow line width square coils:

$$L \cong (2\mu_0 D/\pi) \ln (D/w) . \tag{1.50}$$

For more arbitrary loop shapes, and for taking into account the kinetic components, three dimensional numerical computations are required [37]. Comparison with these computations shows that the inductance of a rectangular slit hole can be roughly estimated from an empirical formula [38]:

$$L \cong 0.48a + 1.7b \ \ [\text{pH}] \tag{1.51}$$

where a is the slit length and b its width, in micrometers. Inductances of narrow slits can be also estimated from other formulae for coplanar lines [39]. A compendium of inductance and capacitance formulae useful in SQUID design is included in [40].

Effective area calculation: The effective area of the square washer with a square hole [41] is:

$$A_{eff} \ = \ adD \tag{1.52}$$

where the coefficient a is of the order of unity. for a circular washer:

$$A_{eff} = (8/\pi) (r_1 r_2) \tag{1.53}$$

where r_1 is the radius of the washer and $r_2 = d/2$ is the radius of the hole. One can see that such flux focusers are not very effective since A_{eff} increases only linearly with D or r_1. Nevertheless, they have been in practical use, especially in first and second generation HTS rf-SQUIDs.

An alternate single-layer SQUID layout resulting in comparable A_{eff} values per unit area is the direct coupled SQUID shown in Figure 10 [42]. This is currently the dominant design approach for HTS dc-SQUID magnetometers, although it is also applicable to rf-SQUID. The large flux focuser is replaced by a pickup loop (antenna) of inductance L_p and geometric area A_p, analogous to that used in planar thin-film flux transformer described below. The coil is connected to the loop of a very small washer SQUID such that the signal current induced in the pickup is injected near the junction. The effective area of this structure is [43].

$$A_{eff} \cong A_s + \alpha_d A_p \left(L_s/L_p\right) \tag{1.54}$$

where A_s is th effective area of the small washer and $\alpha_d \leq 1$ is the coupling coefficient given by the fraction of L_s, to which the signal is coupled. Since $L_s \ll L_p$, with L_p of the order of the 10 to 20 nH on a $1cm^2$ substrate chip, the mismatch between the two inductances is enormous (ideally one would need $L_s \cong L_p$), and even the fact that α_d usually approaches 1 cannot help much. Making the pickup loop width large can reduce L_p by a factor ≤ 2. The layout with a very wide loop approaches that of a large washer, but in higher ambient fields direct coupling might have distinct advantages.

1.5.4 rf-SQUID Electronics

Practical use of SQUIDs require conversion of their specific physical properties into useful signal and characteristics. This task is accomplished by SQUID electronics, which in most application can roughly be divided into the electronics used to operate (bias) the SQUID sensor, the feedback loop to linearize the SQUID transfer function characteristics and the data acquisition system. In Figure 1.15 typical transceiver circuit with additional low frequency signal generator is shown. Without going into much details we will just describe a basic principle of the transceiver and for further reading much detailed work can be seen in references [31],[33], [44], [45], [46], [47], [48].

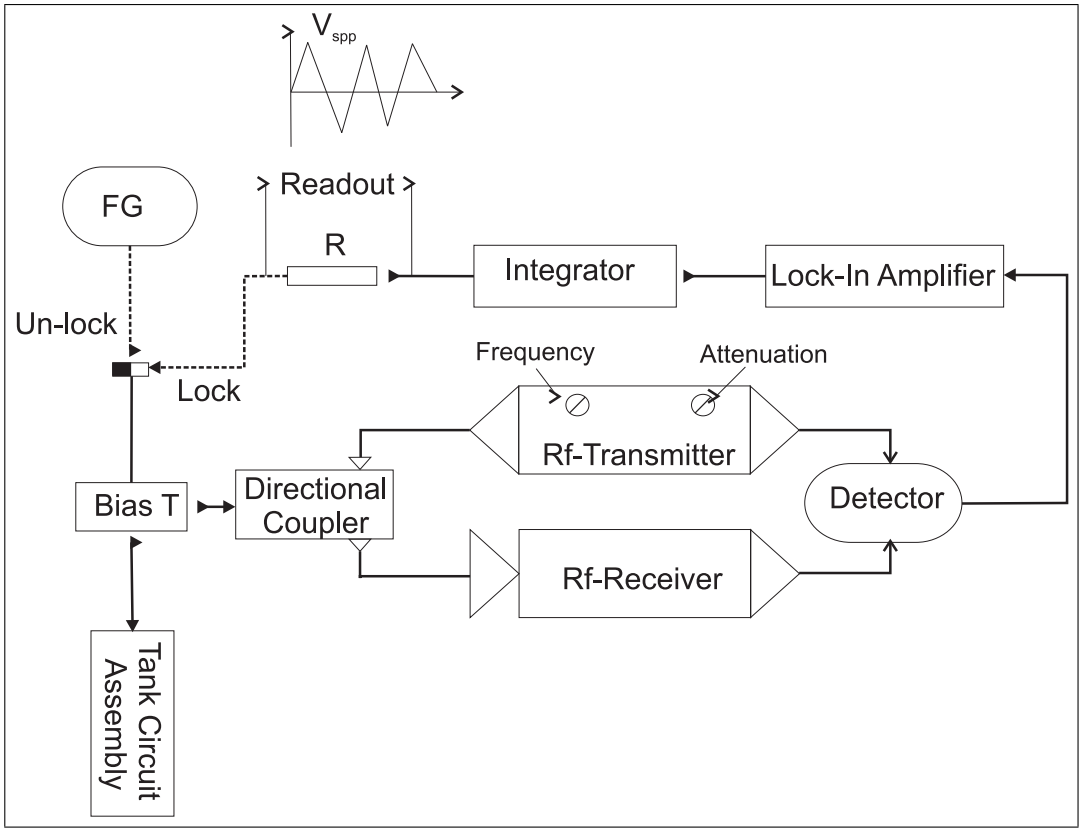

Figure 1.15: A typical schematic for rf-SQUID readout electronics.

The rf source (transmitter) supplies the rf power to rf-SQUID tank-circuit assembly via a directional coupler having good isolation (preferably 15dB larger than the return loss of the tank circuit assembly [48]). The response signal coming from rf-SQUID is taken from the tank circuit assembly through the same directional coupler and amplified to a detectable level [49]. Besides, the output signal (V_s) is taken on feed back resistor. For detection, a spectrum analyzer or a detector with an oscilloscope can be used. In our mode of operation a low rf power (-60dBm to -90dBm) is applied to the SQUID, such that, during its cycle, no quantum transition takes place. For this to happen, critical rf magnetic flux should not exceed,

$$\Phi_{rf} = \frac{\Phi_0}{4} + L_s I_i \tag{1.55}$$

Here L_s is the effective inductance of the rf-SQUID and I_i is the super-current

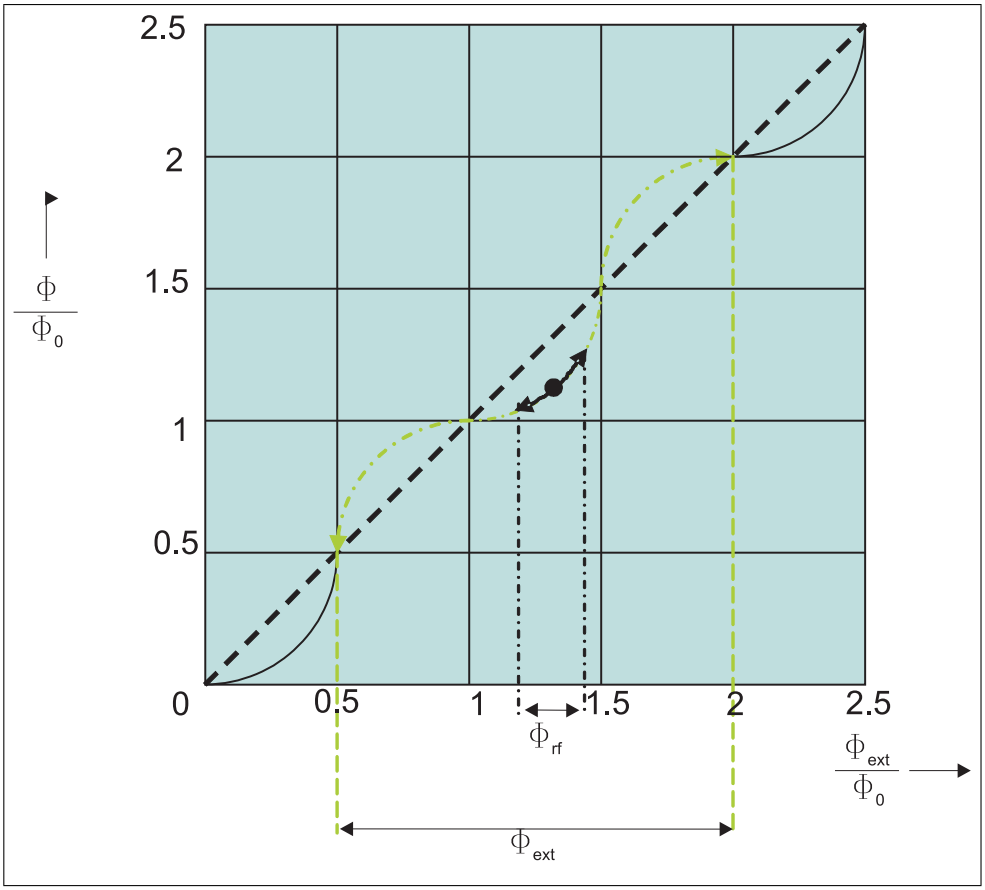

Figure 1.16: The effect of externally applied low frequency signal flux together with rf power flux.

in the loop. At this point, an externally applied low frequency signal creates magnetic flux via a coupling coil on the tank circuit and the bias position of the rf-signal sweeps. This case can best be understood from curve indicated in Figure 1.16. The extent of Φ_{ext} is much larger than Φ_{rf} and when applied together, Φ_{rf} sweeps over Φ_{ext} on the flux curve. According to figure 1.10, an applied Φ_{ext} causes Φ_{rf} to sweep between two staircase patterns [50], [49]. Thus an amplitude modulation is applied to the rf power whose envelope has a triangular like relation. This triangular like signal is called SQUID signal, flux to voltage transferfunction, V_{spp}. Phase sensitive detector compares the phases of the original low frequency signal with detector output to give a dc component, which is an error signal giving a measure of how far the SQUID is from the extrema where it has been biased. If a flux locked loop is implemented together with the integrator, the error signal

will be integrated and fed back to SQUID to change SQUID's state to one of the extrema, at which the detector output will give "0" voltage. In this condition, SQUID's condition will only change in flux fluctuations [31], [51], [49] and [52].

Chapter 2

Fabrication and Characterization of Josephson Junctions for rf-SQUID Applications

2.1 Introduction

In order to investigate the optimal parameters for rf-SQUID layout design, junction characteristics of SEJs and BGBJs on crystalline $LaAlO_3$ and bi-crystal $SrTiO_3$ substrates, respectively, have been studied in detail. Measurements of the magnetic field dependence of the I_c of the junctions were also performed to investigate the field sensitivity of our GB based technology rf-SQUIDs. Here in this chapter we present the investigated dc characteristics and magnetic field dependencies of YBaCuO bi-crystal grain boundary junctions (BGBJs) and step edge junctions (SEJs). Test junctions, up to 8 μm widths, as well as the junctions of the rf-SQUID were studied for both type of the fabrication processes. This study provides us insight to the optimum design parameters and limits imposed by each technology, which can be useful to determine the more advantageous techniques to fabricate magnetically stable rf-SQUIDs for magnetic imaging systems. During the course of this work, the dependencies of the junction parameters on junction

width, magnetic field, and temperature has been investigated. The SEJ based samples were made on $LaAlO_3$ (100) with ramp type and sharp step structures with height of 150-300 nm [5], [25]. The bi-crystal GB devices were made on symmetric 36.8^o GB bi-crystal $SrTiO_3$(100) substrates. All the junctions were characterized in four probe configuration, by making contacts with wire bonding either directly onto the surface of the films or by using gold coated contacts pads. Contacts made by this procedure resulted in contact resistance in range of a few Ohms at low temperatures.

2.2 Film Deposition by PLD

Pulsed laser deposition (PLD) is a successful thin film deposition method for the preparation of epitaxial films on different single crystalline substrates from the vapor phase. Several deposition methods like MOCVD [53], MBE [54], [55] and rf-magnetron sputtering [56] have been used to deposit HTS-material as $YBa_2Cu_3O_{7-x}$, ferroelectric $BaTiO_3$ and other perovskite thin films on many different substrates. The advantage of PLD is the stoichiometric transfer of complex target materials to the substrate, which can be maintained at a high temperature in a reactive atmosphere.

2.2.1 Working Principle

In PLD, a high power pulsed laser beam is focused onto a target of the material to be grown. As a result, a plume of vaporized material (atoms, ions, molten droplet, and particulate) is emitted and then collected on a substrate to grow the film [Saenger, 1993; Chrisey and Hubler, 1994]. Figure 2.1 shows the basic PLD setup. By holding a substrate at high temperatures, opposite to the target, the evaporated material condenses on it and a thin film is formed. For high-T_c superconductors and related material, the substrate needs to be heated using a deposition to obtain a crystalline thin film (insitue deposition)and the deposition needs to take place in an environment having oxygen to obtain the required crystal

structure. "If the substrate is aligned orthogonal to the direction of the plume, it is called on axis ablation where as if it is parallel to plasma then it is called off axis ablation".

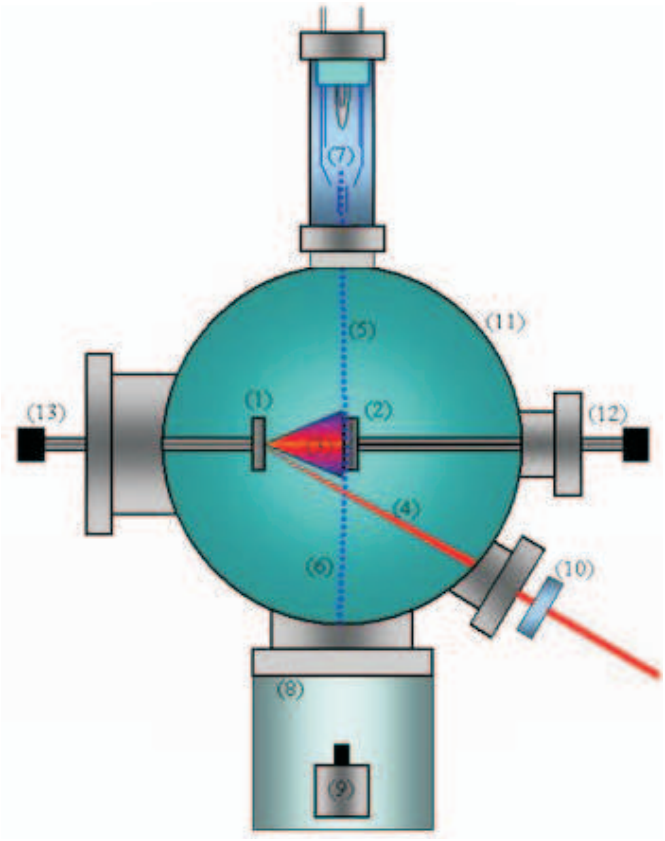

Figure 2.1: A schematic diagram of the PLD system: (1) Target, (2) substrate (heated by direct joule heating), (3) ablated species "Plume," (4) focused laser, (5) electron probe, (6) diffracted electrons, (7) electron gun, (8) phosphorous screen, (9) CCD camera, (10) focusing lens, (11) ultra high vacuum chamber, (12) substrate manipulator, (13) target manipulator [1].

PLD has been used to grow films of superconductors [Schubert et al., 2000; Kim et al., 2000], magnetoresistant materials [Venimadhav et al., 2001; Liu et al., 2001], semiconductors [Ohta et al., 2001; Cazzanelli, 1999; Rouleau, 1998], ferroelectrics [Hur et al., 2001; Goux et al., 2001] and many others. Among the **interesting features** of PLD are:

- Conceptually, it could be used to grow a thin film out of any material, regardless of its melting point.

- The stoichiometry is completely preserved [Cheung and Sankur, 1988].
- The high energy of the ablated particles may have beneficial effects on film properties.
- It could be easily modified to grow multi-component or multi-layered films.
- Most importantly, it consists of periods of high deposition rate (1-10 ms) followed by periods of no deposition (on the second scale), allowing for surface relaxation that may lead to enhancement of the properties of the grown film [Pronko et al., 2003; McCamy and Aziz, 1997].

On the other hand, PLD has some complications. The most challenging one (the most interesting too from the physical point of view) is the formation of particulates, due to splashing of the molten surface layer. In general, the formation is affected by a number of parameters:

- Target density
- Laser pulse duration
- Target surface quality
- Laser wavelength
- Laser fluence

The dynamics of film growth by pulsed laser deposition is quite difficult, because of the large number of interacting parameters that govern the growth process and hence the film properties. These parameters include the substrate type, orientation and temperature, the energy distribution of the particles; the laser parameters (wavelength, fluence, pulse duration, and repetition rate), and the geometry of the experiment. In addition, the periodic nature of deposition has to be taken into account.

2.2.2 The used system specifications

PLD system employs a Lambda Physics LPX305 KrF excimer laser (248 nm, 20 ns, approx. 1 J/pulse, up to 50Hz) [57]. The laser beam is focused by a cylindrical lens (f = 400 mm), resulting in an energy density of more than $2.5 J/cm^2$ at the target. The cylindrical target consists of single phase $YBa_2Cu_3O_{7-x}$ powder YBCO has been pressed and sintered. The SQUIDs are prepared from a 200nm thick film prepared by PLD on a single crystalline $LaAlO_3 - (100)$ substrate with dimensions of $10mm \times 10mm \times 1mm$. The typical deposition temperature for the $YBa_2Cu_3O_{7-x}$ thin film was 780^oC in an ambient of 1 mbar pure oxygen. These films show $T_c > 89K$, $j_c(T = 77K) > 3 \times 10^6 A/cm^2$ and a crystalline perfection measured by the minimum yield value $\chi_{min} < 4\%$ in a RBS/channeling analysis [58].

2.3 Types of the employed Junctions and their fabrication techniques

Two widely used Josephson junctions (JJ) types for fabrication of YBaCuO rf-SQUID are step edge junction (SEJs) and bi-crystal grain boundary junctions (BGBJs). Both types of the junctions have advantages and disadvantages for making the rf-SQUIDs with respect to the dc-characteristics, fabrication, and their I_c magnetic field dependencies point of view. The properties of such JJs are strongly dependent on the detailed crystal structure of the YBCO film at the grain boundary (GB) [5], [59], [60]. It is to be noted that the fabrication of rf-SQUIDs requires an almost precise critical current (I_c) controlled by the fabrication process [25], [61]. This is due to the required optimum SQUID parameter, $\beta_L = 2\pi L I_c/\Phi_0 \cong 1$, where L is the device inductance. The straightforward fabrication of the bi-crystal GB junctions, make them very reliable and successful when can be applied in the circuits and layout designs. The applications of the bi-crystal GB JJs are limited by the extended bi-crystal GB across the substrate, the quality of which is essential in this technology. The SEJs allows fabrication

of very complex circuits with arbitrary position and multiple junctions on the substrate lead in to very high flexibility in integrated circuit lay out designs. But fabrication of the SEJ based circuits are far more disadvantageous compared to the bi-crystal GB based JJs due to the difficulty of the control of the step structures and the micro structure of the film growth at the GB. The magnetic field dependence of the I_c of the junctions are also an important parameter for the rf-SQUIDs made for applications in unshielded environment [62].

Characteristics of both type of JJs technologies are studied in this work. Here we present results on the study and comparison of the characteristics of SEJ and bi-crystal GB Josephson junctions respectively. In this study $LaAlO_3$ (100) and bi-crystal $SrTiO_3$ (100) substrates were used for the SEJ and bi-crystal GB JJs, respectively. This is to determine the more advantageous technique and find the optimum design parameters and limits imposed by each technology for fabrication of magnetically stable rf-SQUIDs [62].

2.3.1 Step Edge Josephson junction (SEJs)

Among the known technologies used to make Josephson junctions(JJ) for High-T_c devices such as rf-SQUIDs, the step edge junctions(SEJs) are the highly preferred and used technology [59]. One of the most attractive features attributed to SEJs is the flexibility they provide for any possible layout designs where they also have besides a relatively simple fabrication process, when compared to the ramp type junctions and low cost when compared to the bi-crystal grain boundary junctions [63], [43], [64], [65]. Another characteristic property associated with SEJs is that they provide lower critical current (I_c) JJs in the micron size dimensions easing the fabrication process by avoiding the need for very small dimensions in devices where small I_c of junctions (I_{c-j}) is required. This is in particular for the typical high-T_c rf-SQUID layout designs where a very small I_{c-j} in the range of a few μA is required at 77K.

A primary requirement for any SEJ based device such as SQUIDs is a high quality step structure. In order to facilitate this, many efforts have been made to

obtain a high yield of stable low noise SEJ rf-SQUIDs by improving both the step structure and the film quality. While SEJ devices provide design flexibility and the relative ease in fabrication, it is well known that due to the nature of such grain boundary JJs, control of the parameters remain a challenge. It is worth nothing that the quality of both the step structure and the superconducting films are essential for a high yield of stable low noise devices such as rf-SQUIDs [59], [4]. The effects of the step structure and the superconducting film on the noise, operation temperature range, as well as the yield and stability of the SEJ rf-SQUIDs were investigated.

It is well known that, optimal operating temperature of the grain boundary junction based SQUIDs is adjustable to a desired temperature (77K) by further oxygen treatment. This is mainly associated with the oxygen content of the GB junctions and is found to be unstable if the final oxygen content is not close to its equilibrium level determined by the junction structure and the growth [58]. The main aim of the SEJ study [66] was to reduce $1/f$ type noise, increase yield, and control the operating temperature range of the SQUIDs without oxygen treatment.

2.3.1.1 Sample preparation

During the course of this study, different type of steps, including ramp and sharp step structures were made onto $LaAlO_3(100)$ substrates using stationary $40-45^o$ angled argon ion beam perpendicular to the edges of the ditches in the substrates. The steps involved to get clean steps are shown pictorially in Figure 2.2 and explained as follows [67], [5].

- Substrate cleaning: Conventional procedure, Ultrasound bath in N-Hexane for 10 minutes to remove oil or grease components. Bath in Propanol - Acetone - Propanol for 3 to 4 hours with moderate ultrasound power (using q-tip if required).
- Pre-Etching: Pre-etching using conventional IBE for $\sim 10min$. Using $\sim 250-600eV$ and $0.1-0.5mA/cm^2$. The main purpose of this step is to

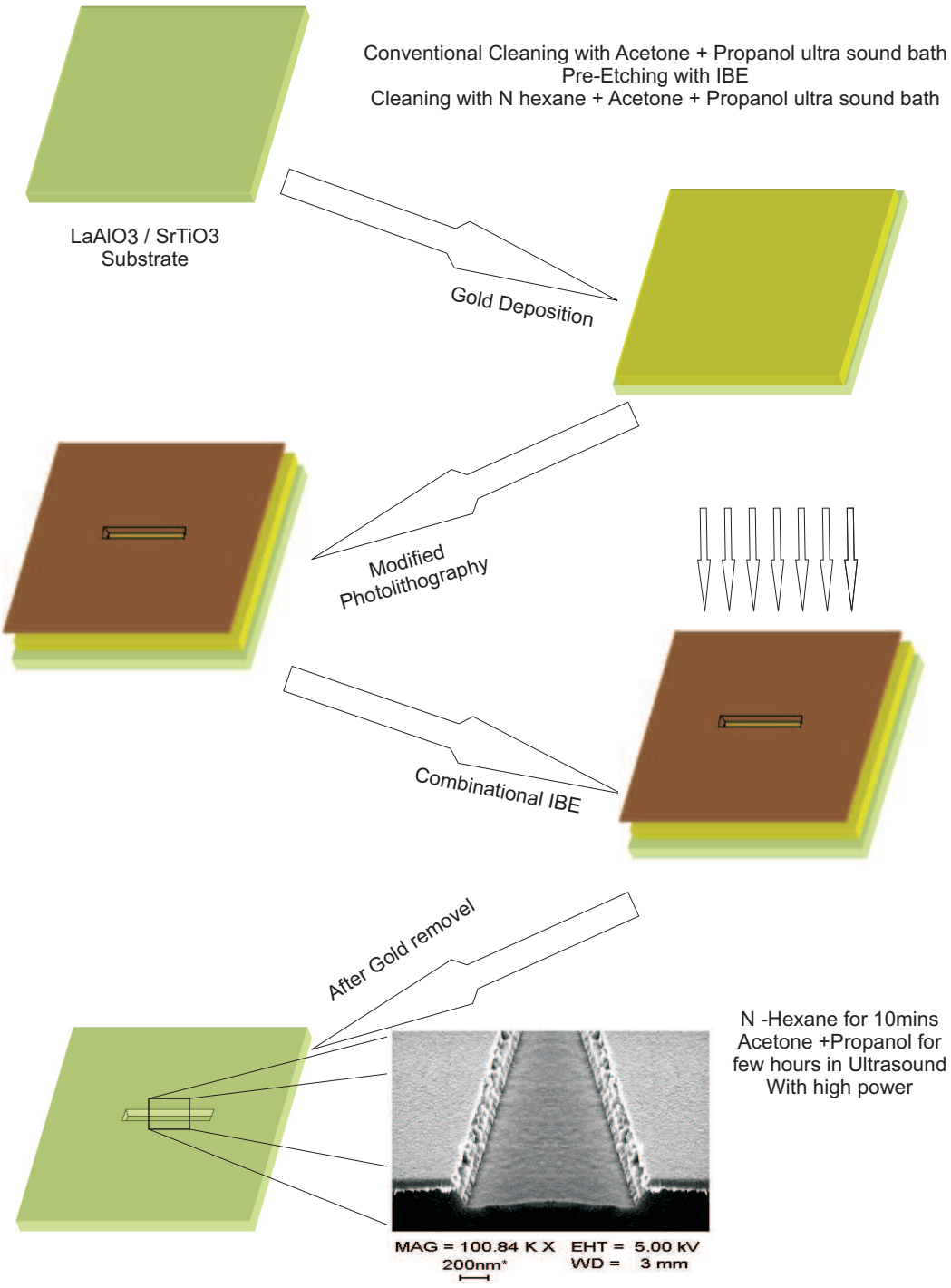

Figure 2.2: Steps involved in the formation of ditch on the substrate for SEJ formation.

reduce the surface roughness if there is any and remove the particles which are embeded on the surface and cannot be removed by simple cleaning process.

- Substrate cleaning: Cleaning with N-Hexane in order to remove grease from the IBE process with moderate Ultrasound and then conventional cleaning with Acetone and propanol for few minutes.

- Gold deposition: In order to obtain clean edges at the steps, prior to the step etching process, a typical ∼70nm thick e-beam evaporated gold layer was deposited on to the substrates with e-beam evaporation technique.

- Photolithography: In the next step, ditches were patterned onto the substrates, using modified photolithography process to obtain sharp photoresist shadow mask patterns. The steps are listed below,

  - AZ5214 and 4000RPM for minimum pattern $\geq 2\mu$m.
  - 5 min. soft bake at 90^oC.
  - Cleaning edges using 30 sec Exposure time and developing in 3(water):1(developer) developer.
  - 1.8 sec exposure time for patterning.
  - 4:1 developer for 30 sec.
  - Hard bake at 100^oC for about 5min.

- Ditch formation: Using combinational Ion Beam Etching Process, ditch with clean and sharp edges is produced for SEJs.

- Gold removal: Wet Etching of Gold is done by Ultrasound bath of warm "KI-I", (1000ml)H_2O + (5ml)KI + (2.5ml)I (1-2 minutes ultra sound), followed by high pressure water (pulsed) for 1 to 2 minutes, then distilled Water bath for 10min. At the end, conventional cleaning procedure stated at the beginning and blow dry.

After obtaining the ditches positioned at desired locations with appropriate quality, the next step is to deposit the film and pattern them for SEJs. The step wise procedure is shown in Figure 2.3 and is listed here as follows:

- Cleaning: N-Hexane for 10 min with Ultrasound. Propanol + Acetone for 3 to 4 hours with 50% ultrasound power (use q-tip if required).

- Film Deposition: Using PLD technique discussed earlier, film with different thickness have been deposited during the course of this study but typical deposition was of about 200 nm.

- Lithography for devices: For patterning the devices, conventional photolithography technique has been used.

- Etching YBCO: In this study, both IBE and chemical etching process has been used for YBCO etching with the parameters given below;

  IBE parameters: for 184 min, 250eV, 44 mA, 0^o, plus Rotation and Shutter. Chemical etching: for variable time, 1000 ml H_2O + 5ml H_3PO_4.

- Cleaning: Use N-Hexane bathing for 5 min with ultra low ultrasound power if YBCO has been etched by using IBE, and then with Propanol for 10 min, otherwise simply propanol with Ultrasound with 10% power.

- Contacts for characterization: There are two ways to make contacts- in first case, gold is evaporated on the contact pad regions and then wire bonding is done, where as in the second case direct wire bonding on the YBCO material is used. In our samples we used direct wire bonding using gold wire with conventional wedge-bonder with modified parameters in order not to apply stress on the junction, which might cause a change in the characteristics of the sample.

- Characterization: Sample was mounted in the system by using non-magnetic chip-holder with 4-probe configuration.

The steps for the fabrication of the devices are listed pictorially in Figure 2.3. The SEM pictures and mask are taken from real samples from the study.

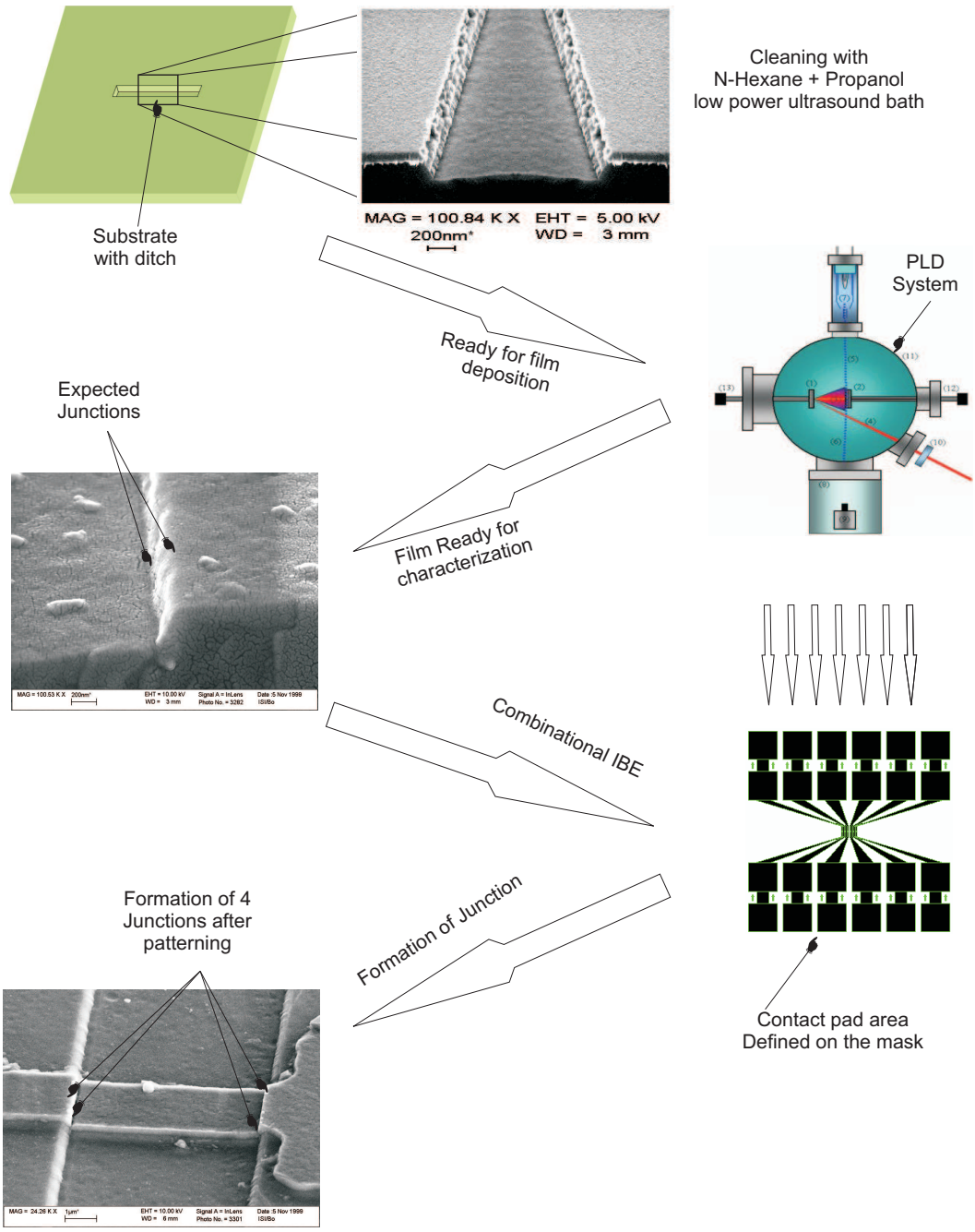

Figure 2.3: Stepwise explanation of the device fabrication process.

2.3.1.2 General characteristics of Sharp step structures

The IBE process is one of the key parameters in obtaining high quality SEJs. While relatively sharp steps can be made using conventional normal incident IBE process, the normal ion beam is also found to cause high re-deposition of presumably the substrate material at the step edges, resulting in very low yield and unstable noisy devices [68], [4]. The sensitivity of the junction properties to the IBE process is found to differ strongly from one substrate material to another mainly due to re-deposition of material at the steps during the IBE [25]. The re-deposition is observed to be much higher on $LaAlO_3$ substrates, as compared to $SrTiO_3$ substrates [68], [4]. The re-deposition is observed to be the highest when a normal incident ion beam is used to develop the steps. A 270 nm deep step structure etched using 500 eV normal incident argon ion beam is shown in Figure 2.4(a). As shown in the figure, the re-deposition can clearly be seen on the side wall of the step (at the broken edge) with a thickness of less than about 100nm and a height of a few hundred nm extended about the edges of the step. A clean sharp step made using an optimized developed IBE process is given in Figure 2.4(b).

Figure 2.4 shows the structures obtained by using a combination of angled rotating and stationary (along the step edges) ion beam. The step structures showed high sensitivity to all the parameters of the ion beam, when prepared using angled ion beam along the step edges. This approach could also lead to rough step structures or light re-deposition of the substrate material at the steps, when unoptimized IBE parameters were used as for the sample shown in Figure 2.4(a). A shallow ramp-type surface with a height up to about 20% of the step height was also observed to form at the bottom of the steps in this IBE process [5]. These shallow ramp type steps can cause relatively high I_c and hence high optimal operating temperature for the SQUIDs close to the T_c of the films [69]. Defected film on the bottom of the trench close to the step edges in case of ramped surfaces resulted as shown in Figure 2.4(c). It has been found that the height of the ramped surfaces at the steps shows dependence on the intensity of the ion beam and the step height, reducing when the beam intensity or the step height

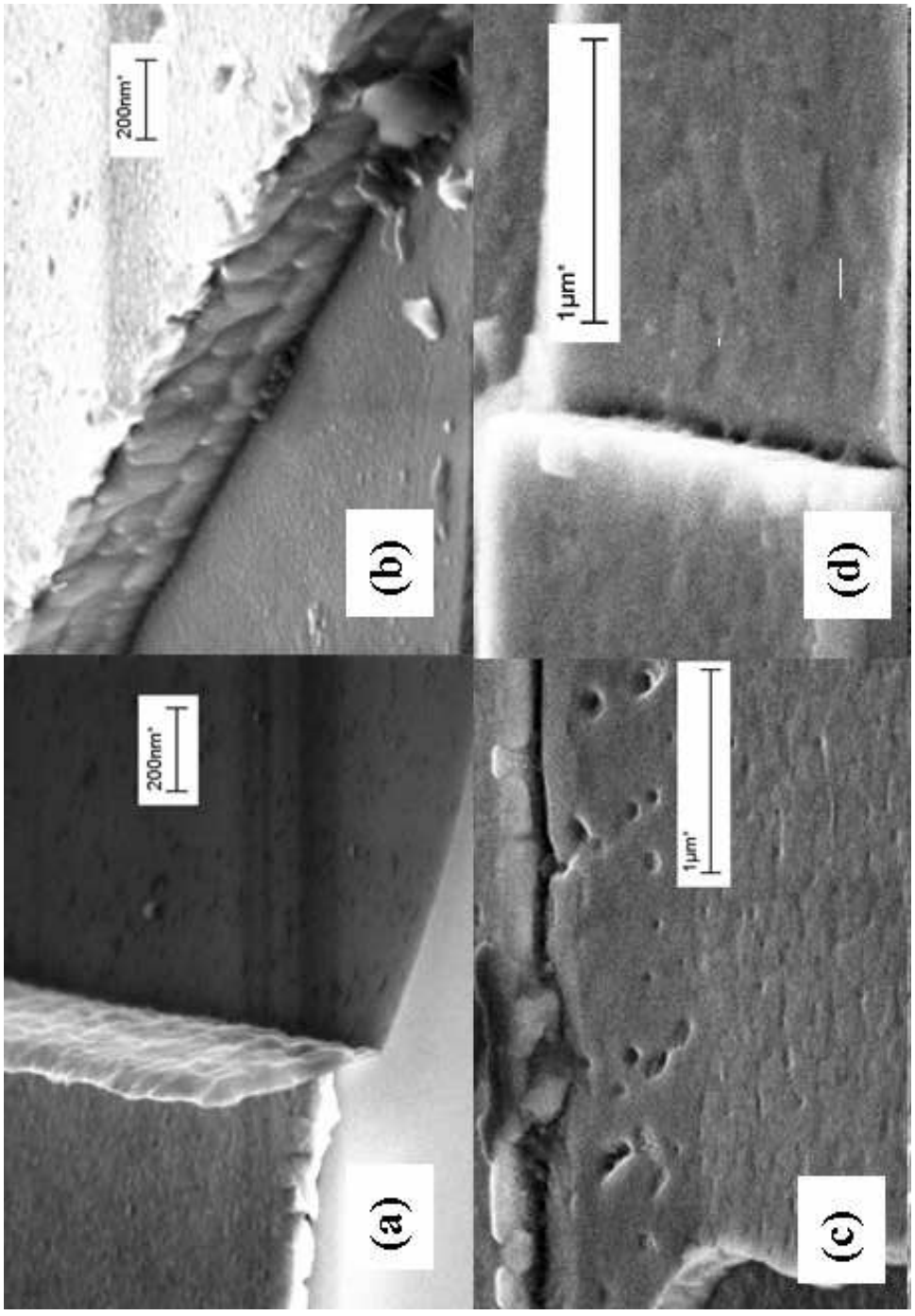

Figure 2.4: SEM pictures of step structures on $LaAlO_3$ substrates; a) etched using normal incident ion beam (left), b) etched using "Combinatorial IBE" process(right)

was reduced.

Sharp clean steps with flat surfaces at the steps were obtained on $LaAlO_3$ substrates using an optimized "combinational IBE" (CIBE) process. This was made using a relatively low intensity ($0.1mA/cm^2$) and high energy ($\sim 600eV$) stationary 40^o angled ion beam along the step edges to reach the approximate desired step height, and using a lower energy ($\sim 300eV$) rotation 45^o angled ion beam to get surface modified steps shown in Figure 2.4(b). High quality films in Figure 2.4(d) with smooth morphology at the steps were obtained on $LaAlO_3$ substrates carrying steps prepared using the above CIBE process.

2.3.2 Bi-crystal Grain Boundary Josephson junction (BG-BJs)

Bi-crystal substrates have been widely used in bi-crystal GB JJ based devices such as SQUIDs [63], [43], [70], [71]. This technology is favored over other possible high-T_c superconducting GB JJ's fabrication techniques due to its straightforward fabrication using thin films across the bi-crystal substrate [70], [71]. This type of JJs has been widely used in fabrication of dc-SQUIDs since the extended GB across the substrate does not impose major limits in the designs [71], [72], [73]. But the applications of the bi-crystal GB JJ's in rf-SQUID's are limited by the extended bi-crystal GB across the substrate [25], [64]. Application of bi-crystal JJ for rf-SQUID requires better quality of the substrate GB as well as the film quality across the GB. This is due to the need to control junction parameters through the fabrication process to obtain proper operation of the rf-SQUIDs, such as for the devices in this work [25]. For determining the limits and characteristics of such devices and to find their optimal designs made using the bi-crystal GB technology, better understanding of the characteristics of the used GB JJ's is also very essential. In this chapter we will investigate the characteristics of the fabricated bi-crystal GB JJ's on bi-crystal $SrTiO_3$ substrates. The junction width, magnetic field, and temperature dependencies of the junction parameters will be discussed.

2.3.2.1 Sample preparation

Bi-crystal GB junctions and rf-SQUIDs were made on symmetric 36.8^o angled bi-crystal $SrTiO_3$ substrate. The samples were made of 200 nm thick YBaCuO films deposited using pulsed laser deposition techniques. The device patterns were developed using conventional photolithography technique and low energy IBE process [4]. In order to investigate the characteristics of the BGBJs, arrays of single junctions were made with junction width of 3, 5 and 8 μm and characterized versus temperature as well as applied magnetic fields. Also arrays of $5\mu m$ wide, 3 to 25 serial BGBJs were made in order to be compared to the characteristics of SEJs with inevitable 4-serial junctions forming at the edges of the steps. The arrays were made of $5\mu m$ wide and 200 nm thick meander-line patterns across the substrate GB.

2.4 Characterization Setup

A Helium dewar based characterization setup with a two layer μ-metal magnetic shield and a temperature stability of better than $\pm$0.1K was used to characterize the samples. Temperatures above $\sim$5K were obtained by elevating the samples above the liquid Helium level using the stabilized temperature gradient in the dewar [4].

In order to measure the critical current of the Junctions or SQUIDs, the $I-V$ characteristics were measured using 4-probe configuration with battery powered electronics which was developed at Institute of thin film and ion technology (ISI), Forschungszentrum Juelich, Germany. Four-Probe measurement technique has been used in order to reduce the effect of contact/lead resistance and thermocouple effect. Current to the sample was applied using low noise current source and read out voltage were fed to the pre-amplifier with amplification range of 10 to 1000 [74]. The leads to the sample were provided with special care to reduce the electromagnetic pickup loops by twisting and with double rf-shielding.

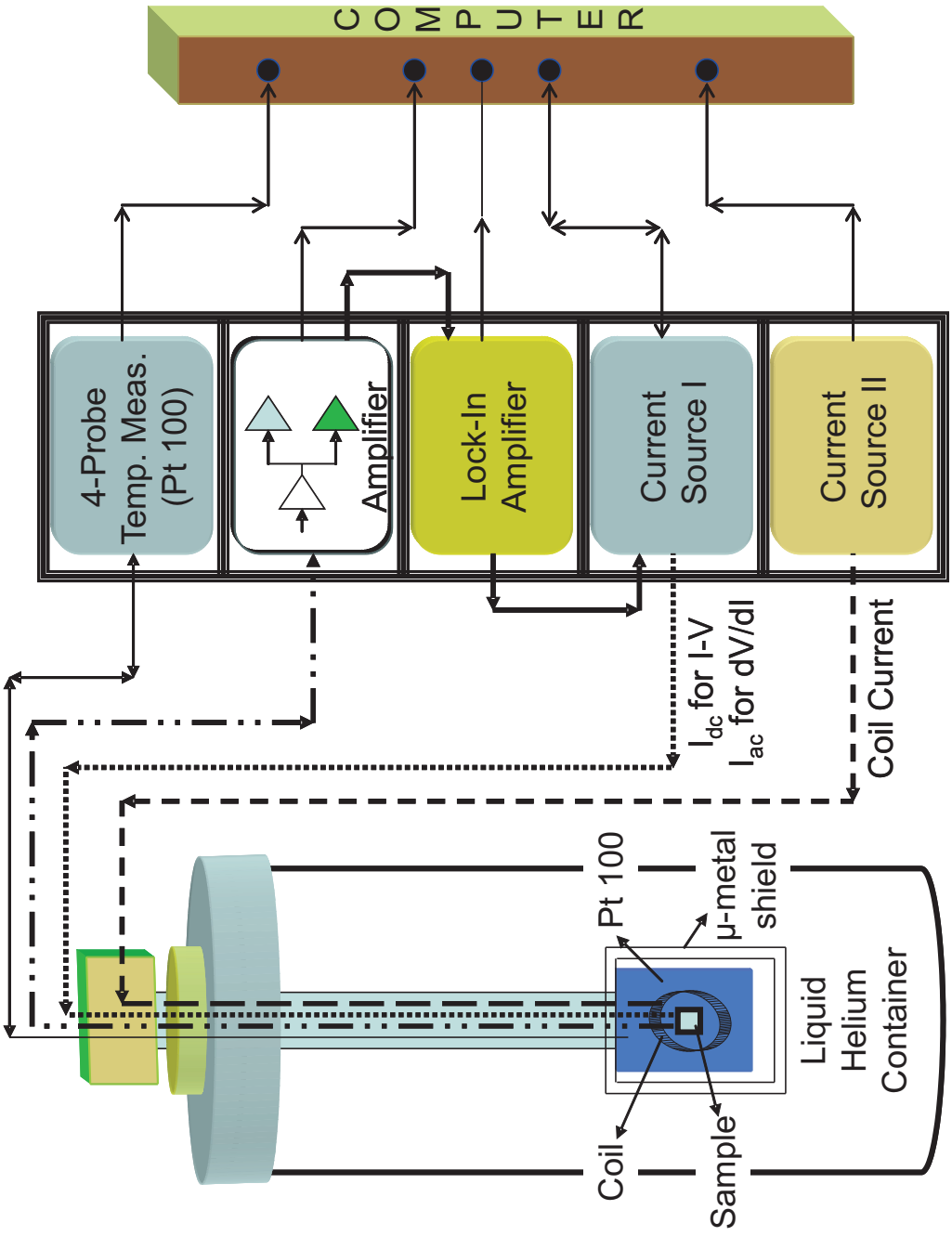

Figure 2.5: Characterization setup using liquid Helium/Nitrogen as coolant.

Due to the fact that Josephson Junctions are quite sensitive to the static loadings, attention must be paid when dealing with the sample either while mounting it on the cold head or by switching between the samples on the same chip that both the equipment and the experimenter must be grounded to the same ground. Characterization setup has been shown in Figure 2.5 and the system with the used electronics is shown in appendix.

The junctions were characterized by making contacts of gold wire bonds directly onto the surface of the films resulting in contact resistances in the range of a few ohms at low temperature. A non-magnetic chip carrier was used to interface the samples to the characterization electronics. To determine I_c and β_L in the presence of large thermal fluctuations ($\Gamma > 1$) at 77 K, measurement of the differential resistance, $R_d = dV/dI$, were performed with standard lock-in techniques. The dynamic resistance, dV/dI, of the samples were measured using an approximate 1% modulation of the bias current through the junction in four-probe configuration. In order to investigate the effect of applied field, all measurements were performed inside a 3-layer μ-metal shield.

Computer program (Messknecht) written in pascal at Forschungszentrum has been used to characterize the samples (JJ and SQUID) for $I - V$ characteristics, dynamic resistance and magnetic field measurement [75]. This has been achieved by controlling the current sources for ramping the bias current via DA convertors and reading the voltages via AD converter.

In order to produce the magnetic field perpendicular to the sample, a coil with 500 turns on a cylindrical core with a inner diameter of 21 mm has been used. This is mounted on the cold finger encapsulating the chip-carrier. With the help of the second low noise current source with an output of 35mA, magnetic field with magnetic flux density of up to 1.2 mT has been produced. The calibration of the coil was accomplished with a Hall probe sensor (Gass meter 912, RFL Elec. INC.). The error in the field measurement was investigated and was found to be of the order of 5% at most.

As for the measurement of magnetic field period ΔB_0 of the critical current

and/or the magnetic field dependence of the $I-V$ characteristics, different magnatizing field levels was required, which was obtained with the computer controlled current incrementation technique through a coil. At each step of applied field, current through the sample has been increased till it showed some voltage, or in other words, reaching the critical current of the junction. Here an appropriate criteria for the voltage should be defined to find out the critical current and in our case we have selected a voltage criteria of 30μV. After obtaining the reading of critical current, current through the coil has been ramped to next value and the procedure has been repeated to find the critical current for the whole range of available field. At high temperatures, i.e. $\sim$77 K, measurements of the critical current is very difficult due to very low critical current values (order of few μA) and strong rounding of the $I-V$ characteristics at the I_c.

Another possible way to measure the critical current is to find the differential resistance, dV/dI. In order to measure the dV/dI, an AC signal with low frequency ($\sim$ 220 Hz) and amplitude of about 0.1- 1μA, has been modulated with the DC current through the sample and the voltage after pre-amplifier and low noise bandpass filter has been fed to the Lock-in Amplifier, which measures the slope of the changing voltage with respect to the applied AC signal. The output of the lock-in amplifier corresponds to differential resistance and is measured together with $I-V$ characteristics of the JJ using a computer. It has been observed that applying AC modulating current does not effect the $I-V$ characteristics of the junction.

In order to monitor the sample temperatures, a crystal diode DT470 with "cryogenic thermometer 820" electronics from Lake shore has used. The temperature sensor possesses an absolute accuracy of $\pm$0.5K with the range of 4 - 90K.

In order to determine the appropriate position of the temperature sensor with respect to the sample for accurate temperature measurement, both R vs. T and inductive vs. T measurement of the film has been done to see the difference in the temperature shift and it has been found that they were quite in agreement [76]. Considering these results and the measuring accuracy of the temperature

sensor ±0.5K, it was said that under 4-probe measurement, an accuracy of about 0.1K can be achieved.

2.5 Investigation of Current Voltage Characteristics of Josephson Junctions

2.5.1 $I-V$ Characteristics of Step Edge Junctions

SEJs were made using $LaAlO_3$ with different steps structures, step heights, and junction widths. These steps were typically made by making up to 10 μm wide ditches on the the substrate. Four serial junctions can be principally obtained in this configuration when a superconducting film bridges a ditch with sharp trenches, resulting in two junctions at each step. In this section, we will discuss in detail the dc characteristics of SEJs based on measurement of $I-V$ and dV/dI characteristics for effect of junction height, temperature effect, and junction width dependence.

Critical current of the junctions showed very high sensitivity to the uniformity of films and micro structures of the steps, investigated by high resolution SEM [5], [4]. It has been observed that average I_c of our SEJs decreased as the step heights increased from about 150nm to about 270nm and there is a systematic change in this decrease with respect to temperature. Quality SEJs made on sharp steps with step heights above 200 nm, showed mostly RSJ like characteristics.

2.5.1.1 Junction width and Temperature characteristics of SEJs

SEJs and SEJ rf-SQUID studied in the following were made on sharp clean CIBE step structures on $10\mu m$ wide ditch onto the substrates [59], [25], [58].

In order to investigate the $I-V$ characteristics of the SEJs, the temperature dependence of the $I-V$ curves and the corresponding dV/dI curves of a $2\mu m$

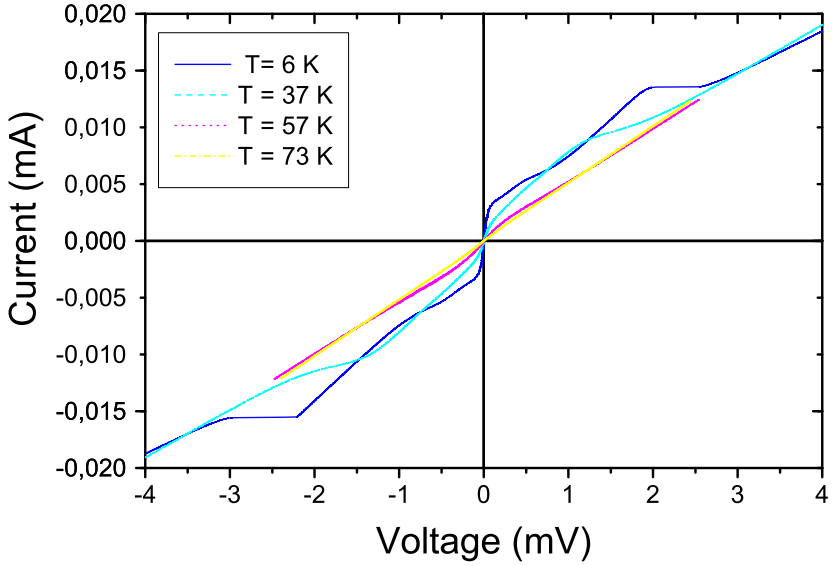

Figure 2.6: Temperature dependence of $I-V$ curve versus bias current of the junction of an rf-SQUID magnetometer made on $LaAlO_3$ substrate with 260nm deep CIBE steps.

wide junction of a low noise rf-SQUID on 270nm deep ditch are shown in Figure 2.6 and Figure 2.7, respectively. While the $I-V$ curves in Figure 2.6 show an RSJ-like behavior, some junctions showed mixed behavior of RSJ and non-RSJ type characteristics. SEJs made on quality 200nm thick films on sharp steps with step heights above 200nm showed resistively-capacitively-shunted junction (RCSJ) characteristics.

Arrays of up to $8\mu m$ wide SEJs were made to investigate the temperature dependent dc characteristics and magnetic field dependencies on the junction width (W_j) of the junctions. It has been found that I_c of the arrays of SEJs increased as the junction widths increased. But a systematic dependence of I_c on W_j was not obtained and the spread of the junction of parameters were higher than that of the BGBJs. It has been found that I_c of the SEJs compared to BGBJs are quite low which makes SEJ being more favorable for fabrication of rf-SQUIDs due to the need for very low I_c for obtaining optimum SQUID parameter at 77K.

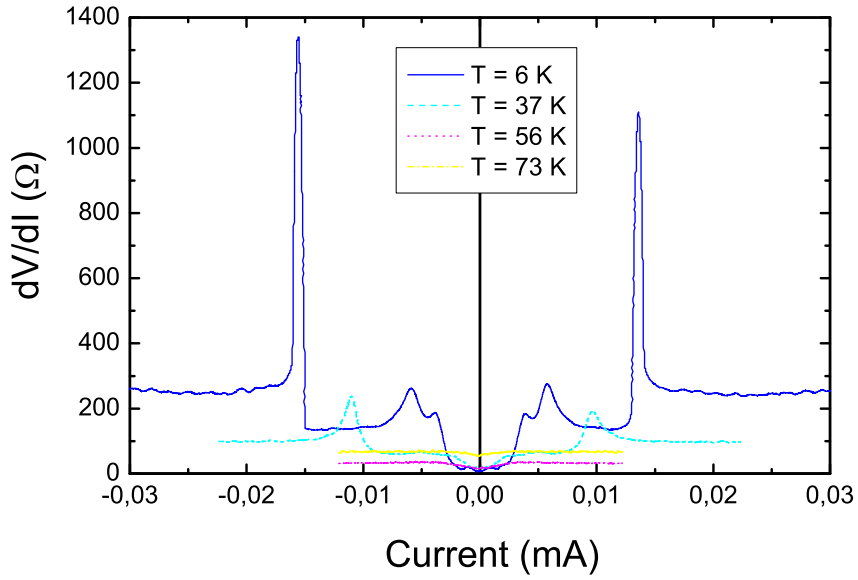

Figure 2.7: Temperature dependence of dynamic resistance (dV/dI) versus bias current of the junction of an rf-SQUID magnetometer made on $LaAlO_3$ substrate with 260nm deep CIBE steps.

2.5.1.2 Behavior of Dynamic resistance of SEJs

It was observed that, R_n values, as shown in Figure 2.7, are relatively high for the samples used in this study [77]. The R_n of the SEJs was in the range of a few 10s of Ohms for junction widths, W_j, in the range of a few micro meters. Characteristic resistivity, ρ_n, of the SEJs are measured to be relatively high compared to BGBJs.

Scaling of R_n and I_c of the SEJs with the W_j, resulted in close I_cR_n products in the junctions and were also decreased with increase of the temperature as shown in Figure 2.7. While the R_n values of RSJ-like behavior SEJs decreased with increase of temperature further than that of the BGBJs, the typical higher ρ_n of the SEJs is interpreted to be a major advantage of the SEJ technology in obtaining lower white noise. Figure 2.8, shows the typical dc characteristics discussed in above.

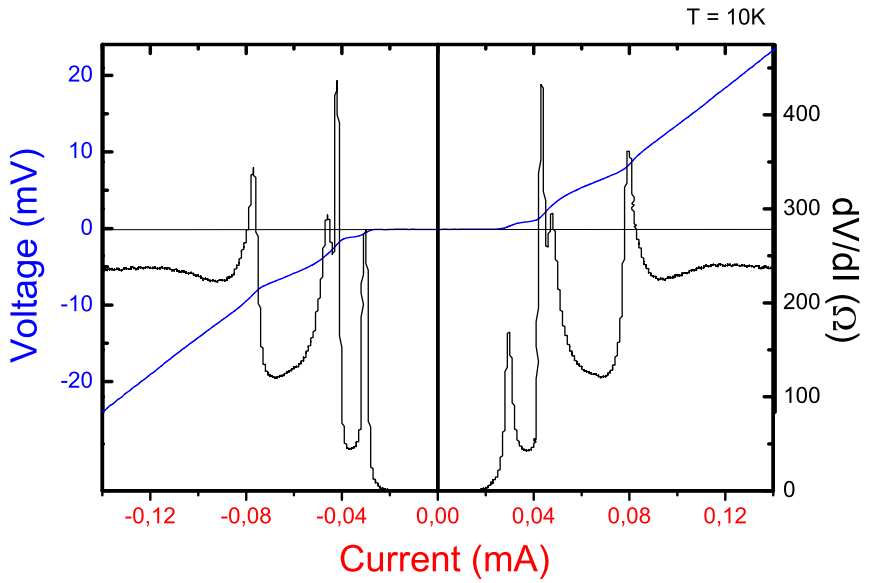

Figure 2.8: $I-V$ characteristics and corresponding dV/dI at $\sim$ 10K of the $2\mu m$ wide SEJ of an rf-SQUID magetometer made on $LaAlO_3$ substrate with 255nm deep steps.

2.5.1.3 Nonlinear behavior of SEJ's characteristics

The $I-V$ curve of a $3\mu m$ wide junction with low hysteretic behavior ($I_{c-min}/I_{c-max} = 0.95$ at $B_a = 0$) is shown in Figure 2.9.

The $I-V$ curves were obtained by ramping the current from negative value to the maximum positive value as shown by the arrow. The measurement were done in the figure by increasing the temperature from $\sim 6K$ to $\sim 77K$.

The slight hysteretic behavior shown in Figure 2.9 can also be seen in Figure 2.8 and at low temperatures of Figure 2.6. The associated Steward McCumber parameter, $\beta_c = 4\pi e I_c C R^2/h$ [78], resulted in a junction capacitance of about 0.5 to 2fF. This results in a junction capacitance in the range of 0.5 to a few $\mu F/cm^2$, well below the expected typical reported values for Y-Ba-Cu-O JJs [79], [80],[78], [81], [82] ,[83], [4], [84] [85]. The observed relatively low capacitance and high R_n values of our SEJs, as shown in Figure 2.10, suggest effective junction areas much

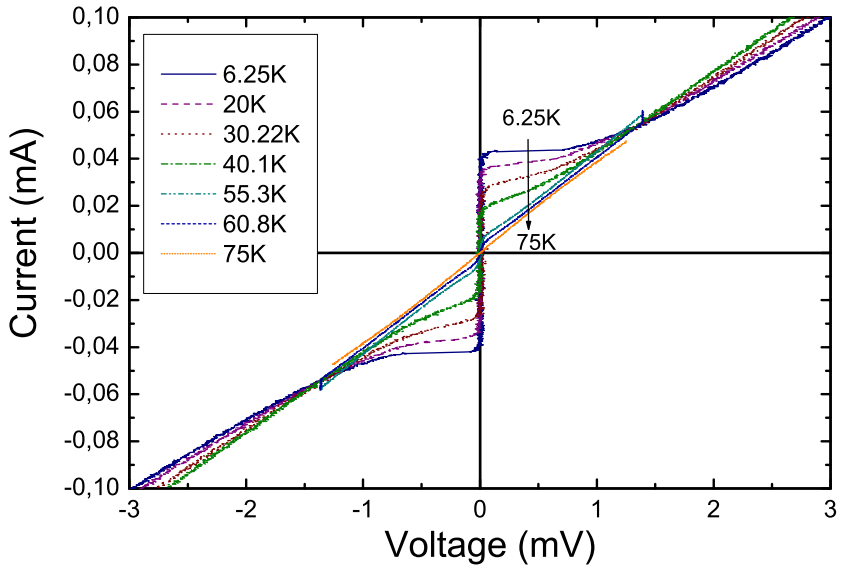

Figure 2.9: Typical temperature dependence of $I-V$ characteristics of a RSJ-type Single SEJ on 260nm deep step ($3\mu m$ wide)

smaller than the geometrical "area" of the junctions [62], [77]. The SEJs with low I_c do not show hysteretic $I-V$ characteristics which can be associated with low ratio of Josephson coupling coefficient to the thermal fluctuations or simply high junction noise parameters, $\Gamma = 2\pi K_B T/I_c\phi_0$ [62]. This characteristics of low I_c and C_j properties of SEJs make it much more suitable for the fabrication of the rf-SQUID [86].

$I-V$ curves of the junctions showed slight nonlinear behavior at $V \approx I_c R_n$ with deviation from the simple RSJ-model at low temperatures as shown in Figure 2.9. This is similar to that associated with the Josephson flux motion effect happening in junctions with widths of about 4 times larger than the Josephson penetration depth, $\lambda_j = (h/4\pi e J_c \mu_0 (2\lambda + d))^{0.5}$ [78], [81]. In order to calculate W/λ_j for our SEJs, geometrical widths of the junctions have been used. The ${}^{W_j}/_{\lambda_j} <\sim 2$ was obtained as the criterion for the linear $I-V$ curves for our SEJs as the limiting factor for both types of junctions in obtaining low noise devices [69]. The usage of ${}^{W_j}/_{\lambda_j} <\sim 2$ from geometrical widths of the junction rejects the possibility of having micro-short structures for the investigated SEJs in this

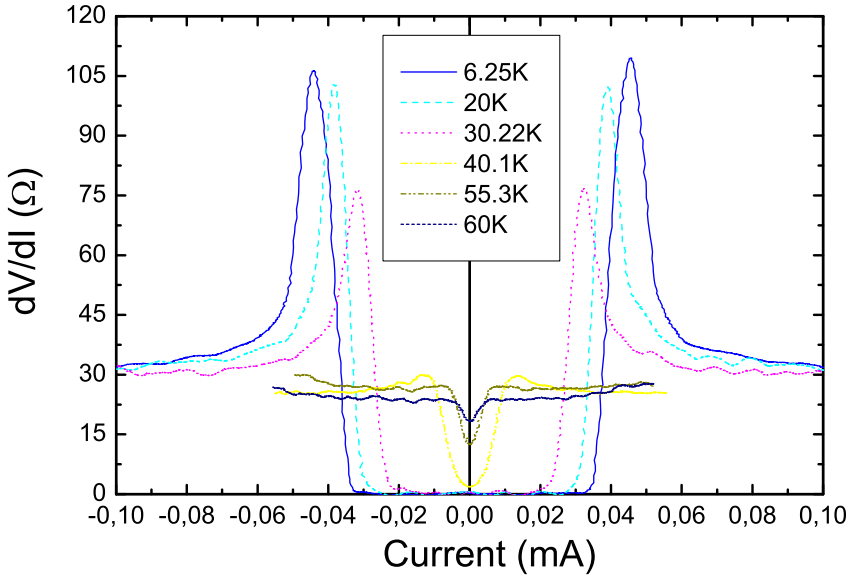

Figure 2.10: Typical temperature dependence of dynamic resistance of a RSJ-type single SEJ on 260nm deep step ($3\mu m$ wide)

study, which might be concluded from their low I_c and C_j values. The above suggests an effective junction area proportional to "W_j" for both types of our junctions, as also confirmed by the dependence of the I_c on the junction widths as shown in Figure 2.11.

2.5.2 $I-V$ characteristics of Bi-crystal Grain boundary junctions

For determining the limits and characteristics of such devices and to find their optimal designs based on the GB technology, better understanding of the characteristics of the used GB JJs is very essential. Arrays of single junctions were made with a junction width of 3, 5, and $8\mu m$ in order to investigate the characteristics of the BGBJs, with respect to temperature and applied magnetic fields. An example $I-V$ and dV/dI curve is shown in Figure 2.12 for junction widths of 3, 5 and 8 μm.

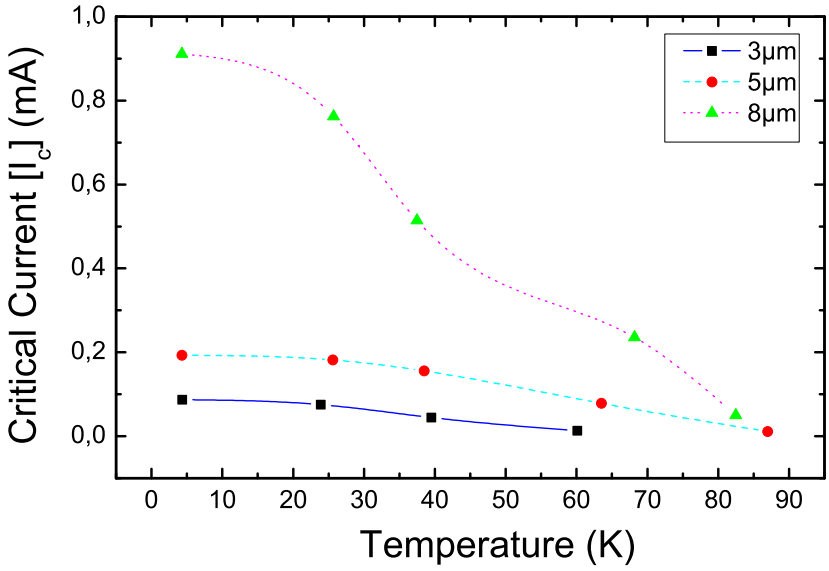

Figure 2.11: Typical temperature and junction width dependence of critical current of SEJs on a 200nm deep ditch on $LaAlO_3$ substrate.

All bi-crystal GBJs fabricated during the course of this study, showed resistively-capacitively-shunted junction (RCSJ) type behavior with hysteretic $I-V$ curves at low temperatures [77]. At low temperatures, $I-V$ curves of all the junctions shows clear RCSJ type behavior with slight hysteretic curve. At low temperatures, $I-V$ curves showed steps corresponding to the number of the junctions in the arrays, while smooth $I-V$ curves were obtained at 70K and above [77].

The critical current density, J_c, of the junctions ranged within about 20-40 kA/cm^2 at 7K decreasing as the geometrical junction width, W_j, decreased.

The sheet resistance of the junctions, ρ_n, at 7K, ranged within about 48-95n$\Omega - cm^2$ increasing with the decrease of W. I_c ratios decreased further than the W_j ratios, which might be due to the side defects or slight non-uniformity of the barrier being more effective for smaller W_j [87], [88].

In order to find out the reason for the unexpected spread of critical parameters,

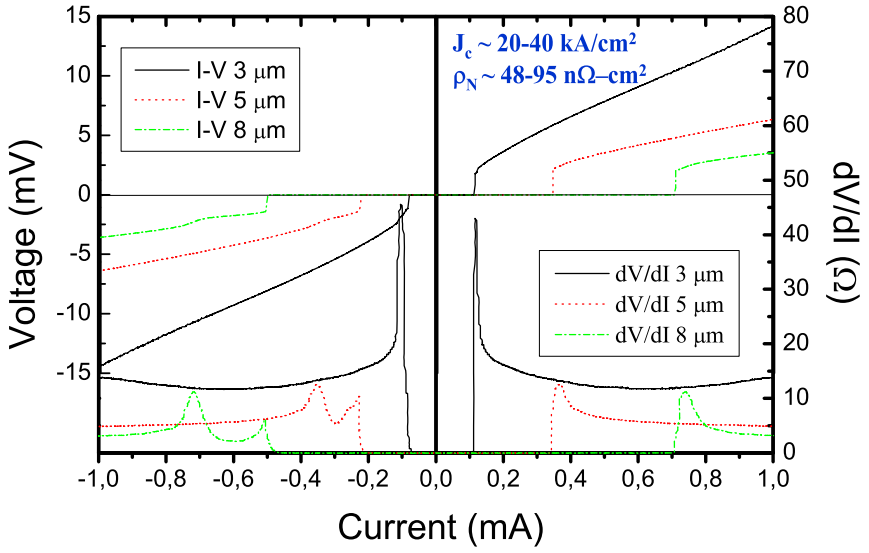

Figure 2.12: $I-V$ and dV/dI curves of 3-8μm wide BGBJs on 36.8^o bicrystal $SrTiO_3$ substrate.

arrays of junctions have been studies [89]. According to observation spread of the junction parameters can be partial reason for the unexpected decrease of I_c ratios compared to respective W_j ratios. These junctions show systematic behavior with respect to number of junctions showing hysteretic behavior with $\beta_c \sim 2.3-2.5$. The spread of I_c of our BGBJs is within the reported values [87], [88] and possibly caused by the optically observable defects at the substrate GBs [69]. The I_c of the junctions at around 77K decreased to very low I_c values proper for application in our typical rf-SQUID designs [86].

2.5.2.1 Dynamic Resistance of BGBJs

Behavior of the normal resistance, R_n, of the junctions were found to be inversely scaled with I_c or width of the junctions, leading to almost similar I_cR_n (or $J_c\rho_n$) values for the junctions on one chip as shown in Figure 2.13.

The R_n of the 3, 5, and 8 μm wide junctions was measured to be about 14,

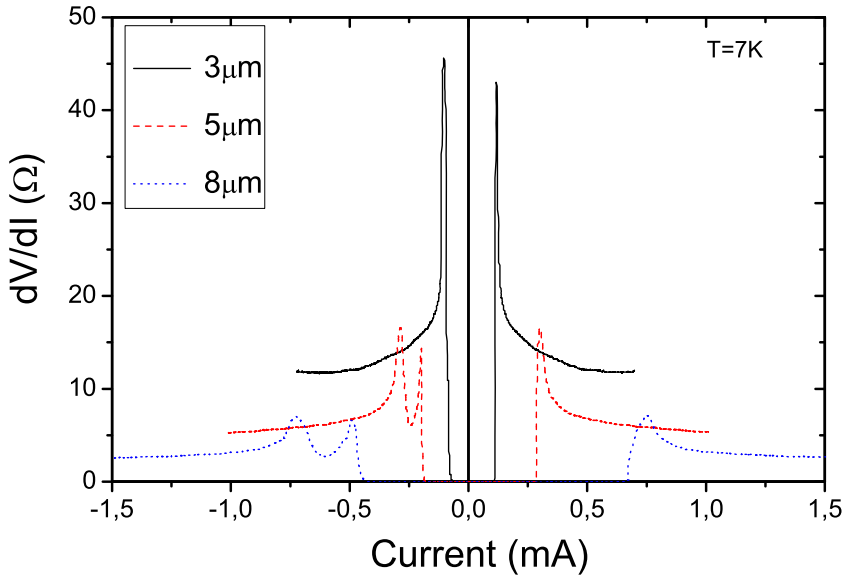

Figure 2.13: Effect of junction width on the dV/dI characteristics at low temperature of 7K.

6, and 2.5 Ω, respectively, leading to I_cR_n in the range of 1.8 - 2.1mV at 7K. This is in the range and slightly higher than the reported values for this type of the junctions [63], [71]. The measured R_n of most of our bi-crystal GB junctions showed slight temperature dependence decreasing by a maximum of about 5-10%, as the temperature increased from 7K to their T_c as shown in Figure 2.14.

The obtained values for the J_c and ρ_n of our samples are close to and slightly better than the typical reported values [79], [80], [87]. While the I_c of the junctions made on one chip decreased as junction width decreases, a systematic change of the I_c was not observed. The I_c ratios decreased further than the junctions width ratios, which is interpreted to be due to the side defects or slight non-uniformity of the barrier being more effective for smaller [87]. We associate the defects at our GB junctions to the optically observable imperfection of the substrate GB's, which deteriorates the film growth at the junctions.

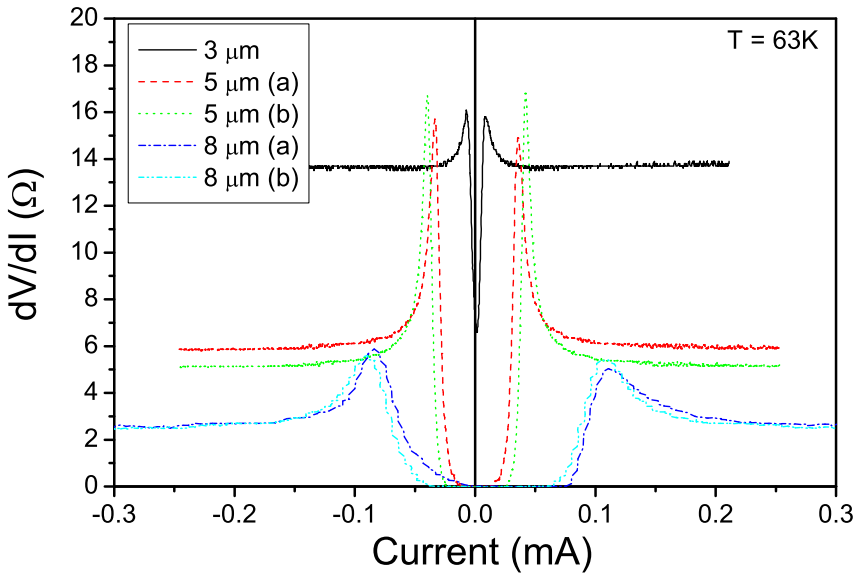

Figure 2.14: Effect of junction width on the dV/dI characteristics at high temperature of 63K.

2.6 Investigation of Magnetic Field Dependent Characteristics of JJ

2.6.1 Principles

The dependence of the applied magnetic field, B_a, on the I_c of the junctions was used to investigate the environmental field sensitivity limits imposed on the SQUIDs. This was also to investigate the characteristics of the junctions, dependent on the physical structure. Investigations of the dependence of the maximum Josephson current on the B_a, provide useful means to make evident spatial variation of the J, since these are reflected in peculiar features of the I_c vs. B_a patterns. A classical magnetic field dependence of the I_c of a JJ is shown in Figure 2.15 for BGBJ of 3-5μm junctions and typical SEJ of 1μm junction.

In order to measure the effect of the B_a, all measurements were performed inside a 3-layer μ-metal shield. The quasi dc field was produced by a calibrated

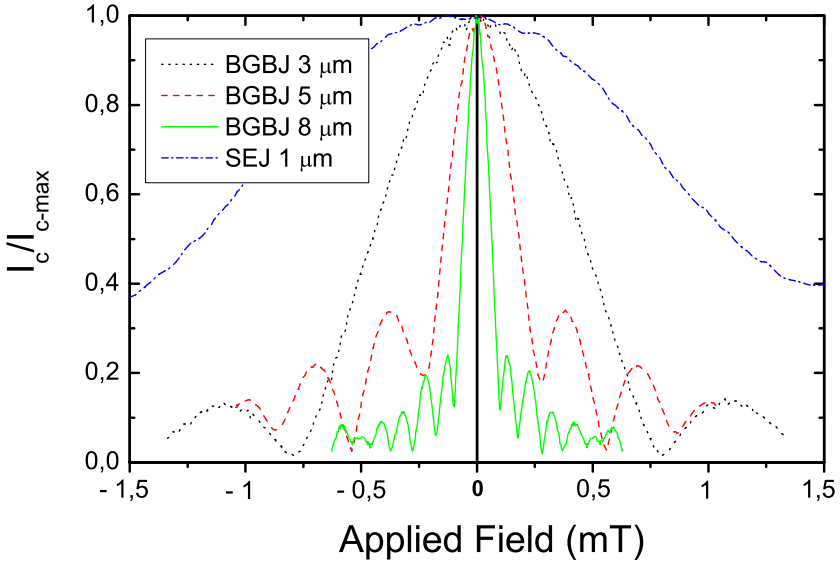

Figure 2.15: Classical magnetic field dependence of I_c of both type of the junctions.

solenoid. $I_c(B)$ was measured in a magnetic field normal to the film surface using a 30μV criterion. To determine I_c and β_L in the presence of large thermal fluctuations ($\Gamma > 1$) at T = 77K, measurements of the differential resistance, $R_d = dV/dI$, were performed with standard lock-in technique. As described in [90], I_c can be derived from the analytic expression of the normalized differential resistance $r_d(i) = 1 - \{1/[2(i^2 + \Gamma^2)] - i^2/(i^2 + \Gamma^2)^2\}$ at zero bias current where $i = I/I_c$ denotes the normalized current and $\Gamma = 2\pi k_B T/(I_c\phi_0)$ is the junction noise parameter.

2.6.2 Characteristics of SEJs under applied magnetic field

2.6.2.1 High field sensitive SEJ characterization

A mixed relatively low and high B_a dependency of the I_c was observed for our SEJs made on sharp steps. The field dependence of a high field sensitive junction

is shown in Figure 2.16.

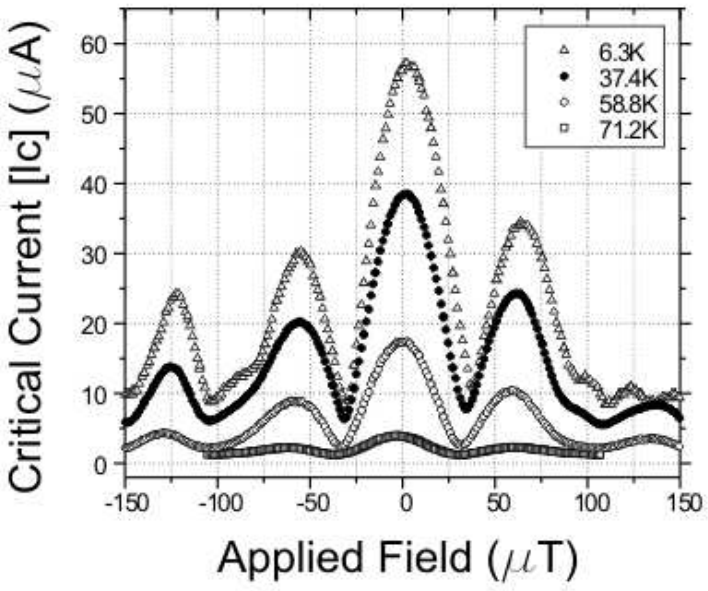

Figure 2.16: Effect of applied field on the critical current, I_c, and temperature dependence of junction of rf-washer SQUID measured after opening the SQUID washer loop.

These junctions has been measured by opening the SQUID washer area of the SQUID mechanically with a diamond cutter. Analysis of this figure will be discussed in detail latter when discussing the characterization of rf-SQUIDs. Here we present the fact that the high field sensitive junctions show Fraunhofer-like pattern. The measurement of I_c(B) at different temperatures (Figure 2.16) demonstrate that there is no strong temperature dependence of the period ΔB_{0-V}. Therefore, The I_c(B) curves were acquired at low temperatures to reduce measuring errors, as the determination of I_c using a voltage criterion is difficult in the presence of high thermal fluctuations at 77K for I_c values of a few μA.

Effect of the junction width on the values of I_c showed inverse proportionality, decreasing from 59.5 - 12.7μT by increasing junction width from 1.4 - 2.7μm [62]. As shown in Figure 2.17, rf-SQUID fabricated by these kind of junctions showed the same field dependence, which makes the device unsuitable for un-shielded applications.

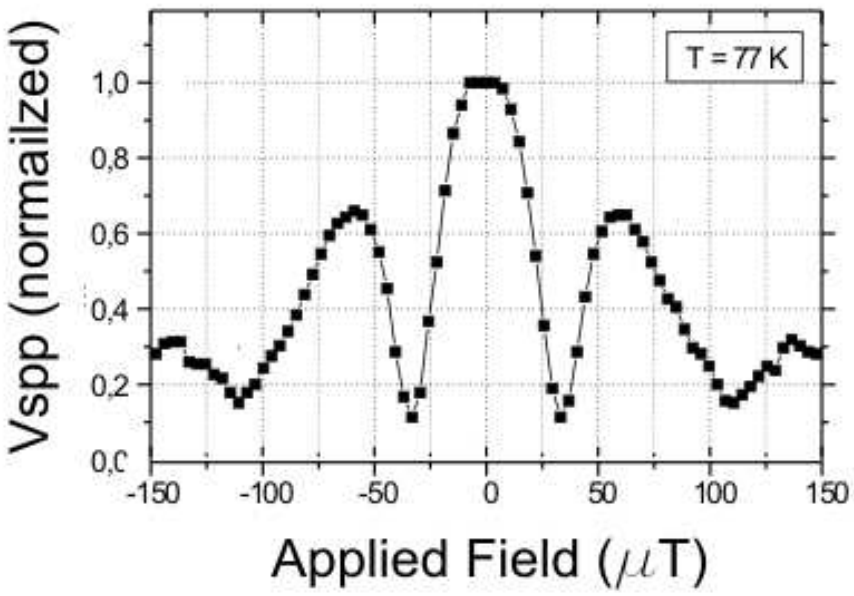

Figure 2.17: Field Dependence of the V_{spp} of rf-SQUID whose junction is shown in Figure 2.16.

The measured dependence of the field period ΔB_{0-V} of the high field sensitive SEJs versus W_j also showed close $1/W^2$ dependence with the consideration of $\lambda \sim 180nm$ at $T < 10K$ [62], [82]. While the ΔB_{0-V} of these junctions scaled closely with $1/W^2$ ratio, a $\Delta B_{0-V} = 6.1\phi_0/(W_j - \lambda)^2$ also gave the best fit to our data for the 3μm wide SEJs as shown in Figure 2.16.

2.6.2.2 Low field sensitive SEJs characteristics

As shown in Figure 2.19, the I_c of the 3μm wide low field sensitive SEJ gave very low I_c modulation ($\sim 25\%$) versus B_a up to about 1.5mT which is well below that expected for such a wide junction. The above mixed low and high B_a dependency of the I_c was observed only for SEJs made on sharp CIBE.

The magnetic field dependence for the low field-sensitive SEJs could not be correlated to the I_c or the geometrical width of the junctions. This might be associated to be due to the physical position of the low I_c junctions at the steps

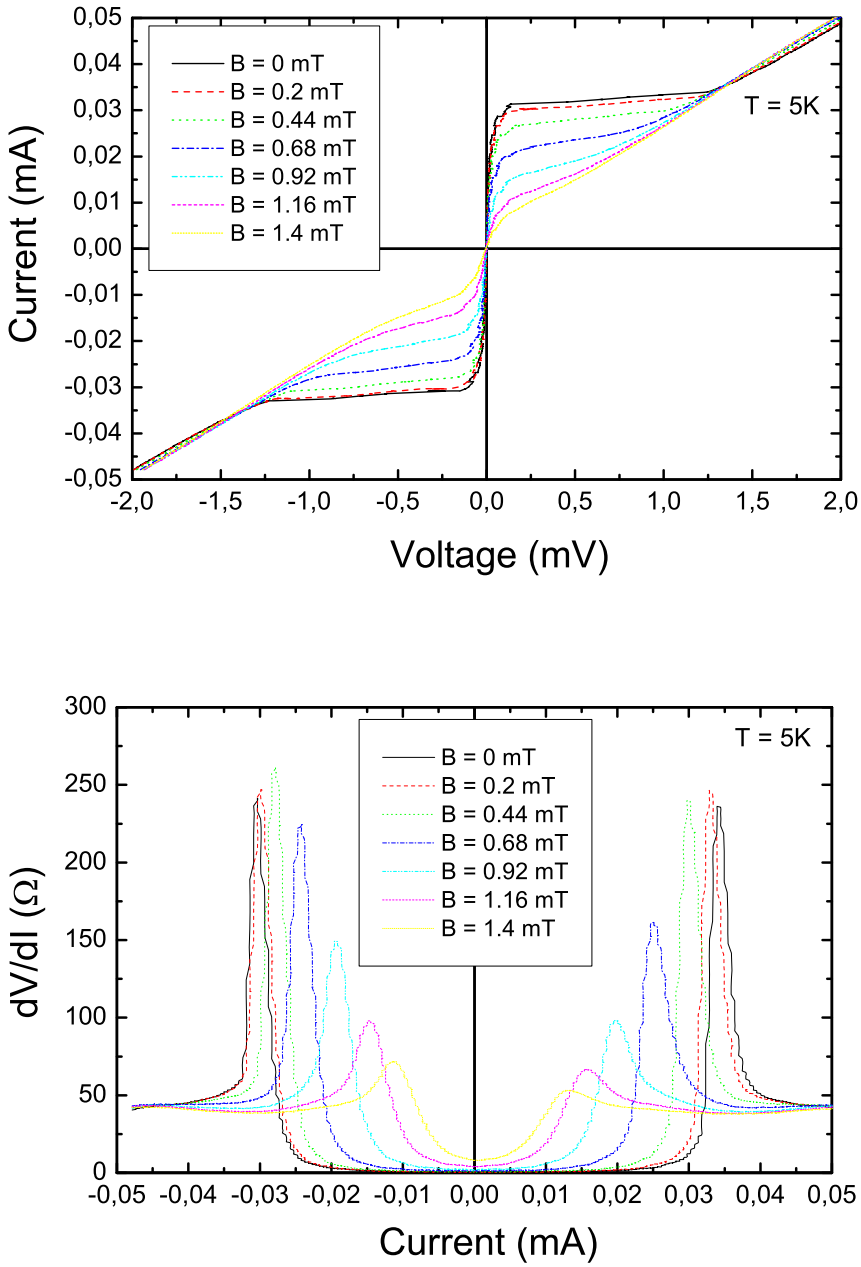

Figure 2.18: Magnetic field dependence of the $I-V$ and dV/dI curves for a high field-sensitive 1μm wide junction made on CIBE step.

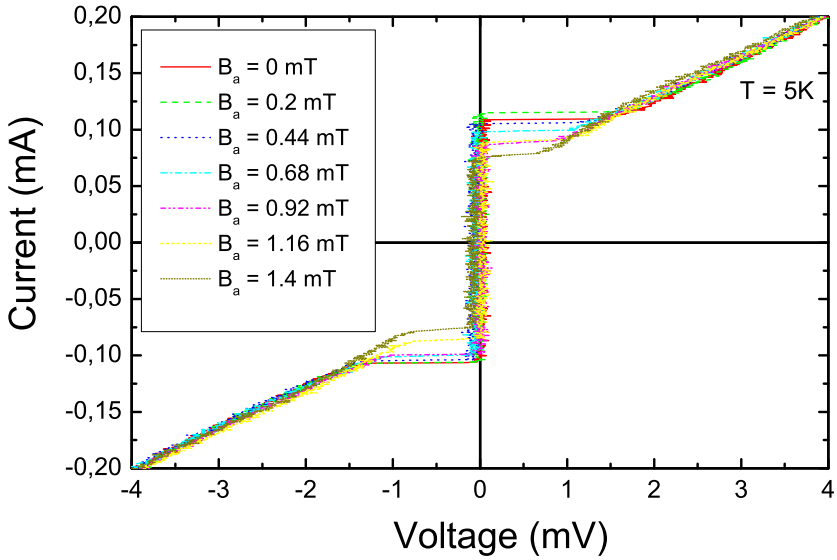

Figure 2.19: Magnetic field dependence of the $I-V$ curves of a low field-sensitive 3μm wide junction made on 260nm deep CIBE steps.

and their orientation with respect to B_a. In order to further investigate the main reason for such a field dependence of the SEJs, single step junction has been made and studied for field dependence. Typical $I-V$ and dV/dI curves of such junctions under magnetic field is shown in Figure 2.18.

The field dependence for the junctions versus temperature was also investigated and the high field sensitive SEJs show *Sinc* type function characteristic with a slight change of the ΔB_{0-V}, associated with the variations of the penetration depth, λ [62], [83]. Typical Field dependent I_c vs. applied magnetic field for such single junction devices is shown in Figure 2.20. These results predict that most active junctions are at the lower corner of the junction and the upper corner junctions are not working, so this film of upper corner provides shielding from magnetic field to lower junctions.

In order to improve the quality of the junctions with respect to the field dependence with the above stated speculation, new junctions have been made after improving the film properties and CIBE process. New SEJs showed almost no

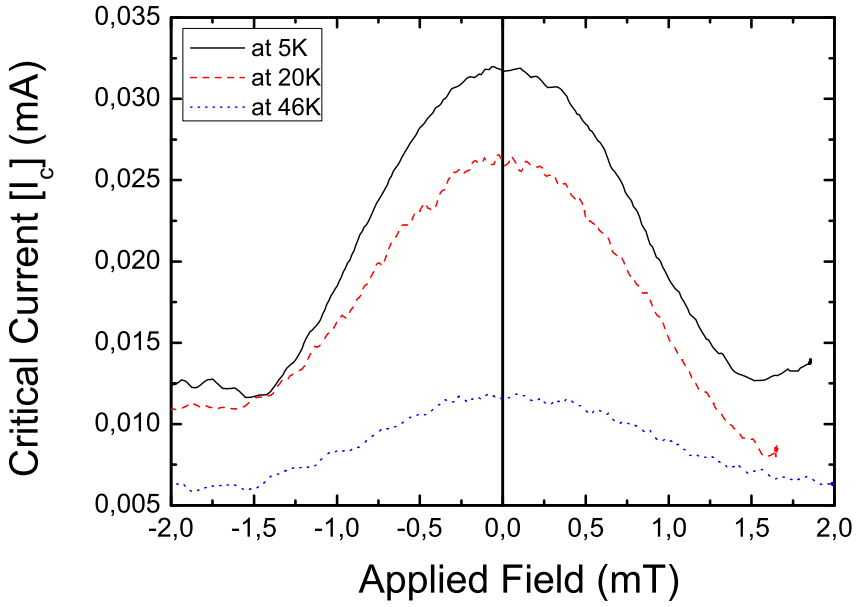

Figure 2.20: The applied magnetic field dependence of a field dependent 3μm wide junction.

dependence on the field, while they show appropriate junction width dependence.

Field dependence of the junctions versus temperature was also investigated and it showed quite systematic change in the decrease of field independent critical current as shown in Figure 2.21 for 8μm junction. ΔB_{0-V} for these new SEJs was found to be infinite for low temperature (Figure 2.21(a)) and high temperature (Figure 2.21(b)) with applied fields up to levels limited by the characteristics setup.

This field dependence behavior might be associated with the physical position of the low I_c junctions at the steps and/or their orientation with respect to the normal incident onto the substrate as well as the B_a. This is while the junction at the bottom of the steps, presumably shielded by the upper relatively thicker films at the edges of the steps [60], are considered to be the effective (lower I_c)junctions among the four serial junctions resulting from the crossing microbridge across the ion beam etched ditch in the substrates [25].

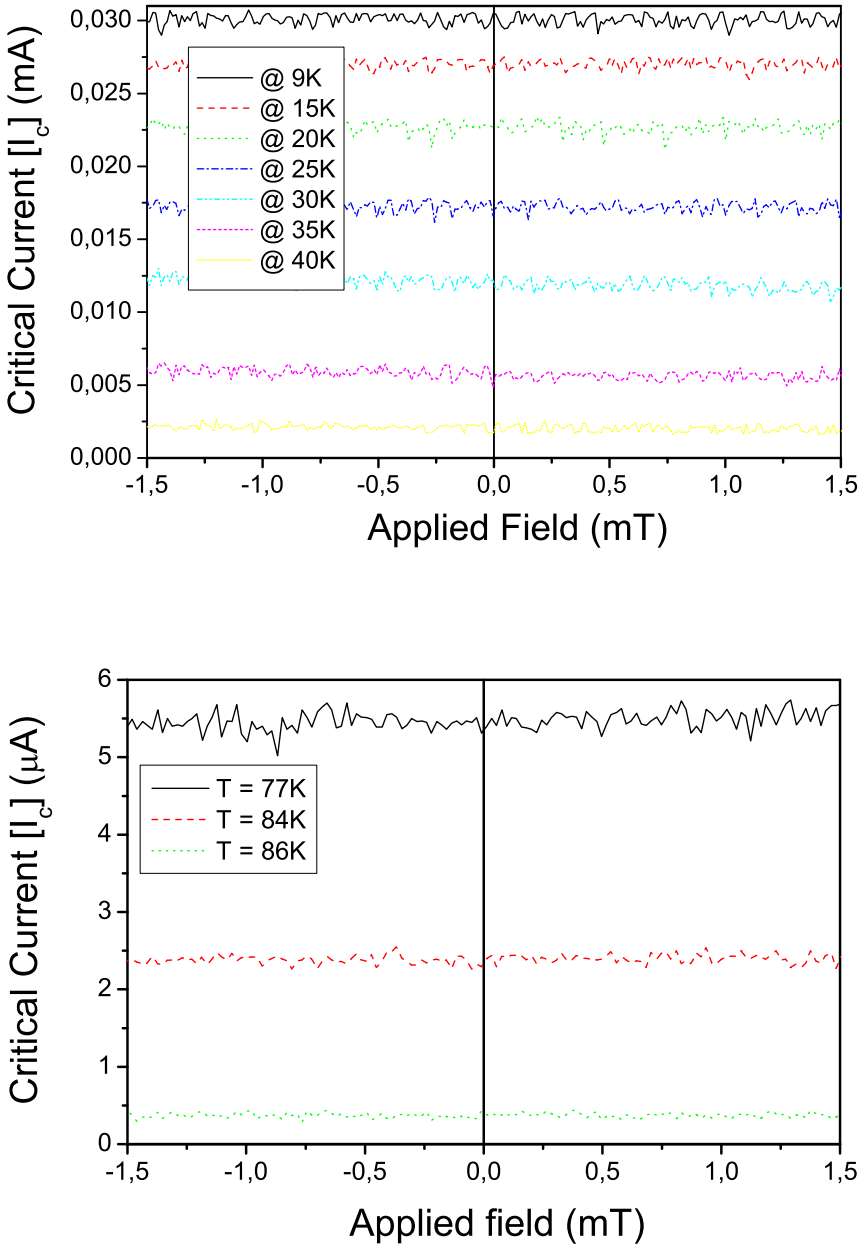

Figure 2.21: Applied magnetic field dependence of the 8μm wide junction versus bias current at various temperatures (top:) Low and (bottom:) high temperature limits.

2.6.3 Characteristics of BGBJs under applied magnetic field

The I_c versus B_a of the junctions in this work revealed a well-defined Fraunhofer-pattern like behavior scaled with the I_c of the junctions showing proportionality to the junction widths. The field dependence of the I_c of three junctions with widths of 3, 5 and 8 μm at 7K is shown in Figure 2.22.

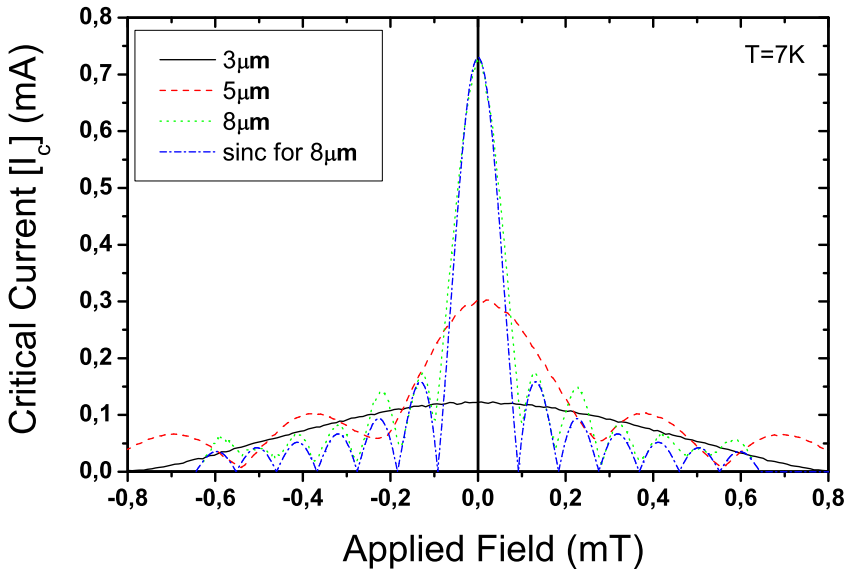

Figure 2.22: Magnetic field dependence of I_c of 3, 5, and 8μm wide GB junctions on bi-crystal $SrTiO_3$ substrates. The calculated classical field dependence of the I_c is shown for the 8μm wide junction.

The measured field dependence of the junctions is very close to the calculated results from the classical field dependence for uniform current through the junctions as shown for the 8μm wide JJ in Figure 2.23. The Sinc function type form of the field dependence of the I_c [69] and its deep modulations in the Figure 2.23 indicate an almost uniform current distribution through the areas of the junctions. This result was closely the same for all the 5μm wide 3 to 25 serial junctions arrays made on one chip. A maximum voltage modulation versus applied magnetic field of about 30mV was obtained for the 25 serial junctions array.

This voltage modulation was made by magnetic field amplitude of less than 0.4 mT, corresponding to about 70 V/T. This is also in agreement with the magnetic field dependence of the I_c for the 5 μm wide junction in Figure 2.22.

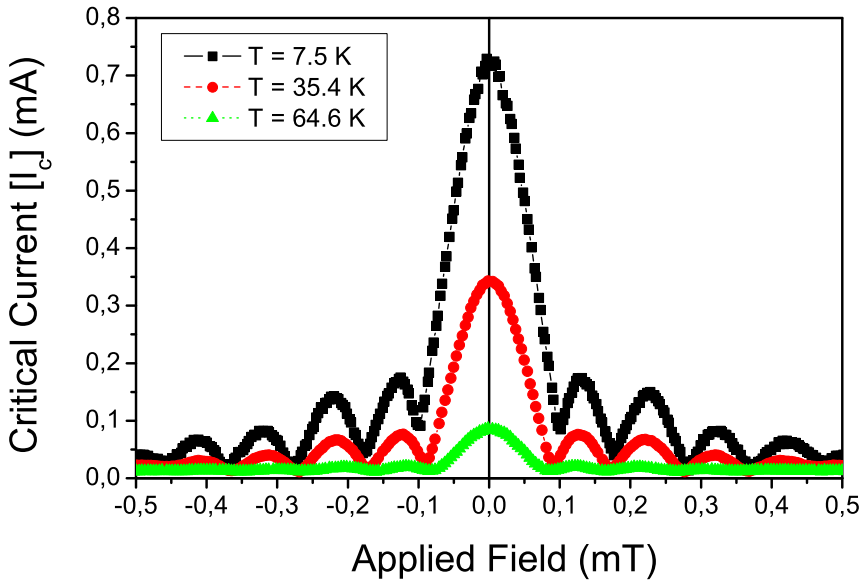

Figure 2.23: The applied magnetic field dependence of the 8μm wide junction versus bias current at various temperatures. The measured field dependence closely follows the calculated magnetic field modulation at all temperatures.

The measured dependence of the field period, ΔB_{0-V}, of the above junctions versus W showed $1/W^2$ dependence [62], [82]. This is mainly associated with the effect of the field focussing factor of the film areas of the patterns. While the ΔB_{0-V} of the junctions scaled with $1/W^2$ for $\lambda \sim 300nm$ [62], [82], it was larger than the expected values. The ΔB_{0-V} of these junctions scaled closely with $1/W^2$ ratio with a deviation of 4% at low temperatures, but a $\Delta B_{0-V} = 6.1\phi_0/\left(W_j - \lambda\right)^2$ gave the best fit for our junctions with width above $\sim 3\mu$m. The $\Delta B_{0-V} = \alpha\phi_0/W_j^2$ fitting approach to our junctions resulted in larger α for smaller junctions at low temperatures. Similar field dependence versus temperature was obtained for all the junctions with a slight change of the ΔB_{0-V}, associated with the temperature dependence of λ_L [62], [83]. A systematic and detailed study of the $\lambda(T)$ dependence of the ΔB_{0-V} has not yet been obtained due to the difficulty of fitting parameters at high temperatures.

Chapter 3

rf-SQUID Fabrication and Characterization

3.1 Introduction

In this chapter, the dependencies of both operating temperature range (ΔT_{op}) and the magnetic field sensitivities of the flux-voltage transfer function (V_{spp}) of the SQUIDs on the device junction types are investigated. The ΔT_{op} and the B_a dependencies of the V_{spp} of the bicrystal grain bounday junction, BGBJ, and step edge junction, SEJ, based SQUIDs is studied based on the dc-characteristics and the B_a dependencies of the I_c of the device junctions. The SQUID signals were measured using the Juelich 1 GHz rf-electronics with a white noise level of less than $10\mu\Phi_0/\sqrt{Hz}$. The noise spectra of the SQUIDs were measured using both the liquid Nitrogen based setup with three-layer μ-metal shield, and the liquid Helium based temperature variable setup with two layer μ-metal shield. The later setup allowed the characterization of the devices versus temperature down to 5K with temperature stability up to 0.5K. Temperature fluctuation has been the source for the 1/f noise below 10Hz of the noise spectra of the samples.

3.2 Fabrication techniques and important parameters

3.2.1 Step Edge Junction rf-SQUID

Among the known technologies used to make Josephson junction (JJ) for high-T_c devices such as rf-SQUIDs, the step edge junctions (SEJs) are highly favorable with respect to the fabrication of complex layouts. While the SEJs provide very high flexibility in the layout designs, they also have relative simple fabrication process e.g. when compared to the multi-layer ramp type junctions, and low cost when compared to the bi-crystal grain boundary junctions. The SEJs are also shown to provide lower critical current (I_c) JJs in micron size dimensions easing the fabrication process by avoiding the need to very small dimensions in devices where small I_c of junction (I_{cj}) is required. This is in particular for the typical high-T_c rf-SQUID layout designs where a very small I_{cj} in the range of a few μA is required at 77K.

A high quality step is the first requirement for any SEJ based device such as SQUIDs . The effects of the steps structure and the superconducting film on the noise, operating temperature range, as well as the yield and stability of the SEJ rf-SQUIDs were investigated. Operating temperature range of the SQUIDs was investigates using the amplitude of the flux-voltage transfer function signal, V_{spp}. The optimal operating temperature of the grain boundary (GB) junction based SQUIDs is well known to be adjustable to a desired temperature (typically 77K) by further oxygen treatment. This is associated to the change of the oxygen content of the GB junction and is found to be unstable if the final oxygen content is far from its equilibrium determined by the junction structure on the growth. The focus of this work has been on the reduction of the 1/f type noise, increasing the yield, and control of the operating temperature range of the SQUIDs without oxygen treatment. In this chapter we will discuss the results on the SEJ rf-SQUID magnetometers and gradiometers on substrates with steps prepared using developed IBE processes and covered with various YBCO film structures to obtain

high yield of stable low noise devices with optimal operating temperature of 77K.

3.2.1.1 SEJ Gradiometer design

SQUID gradiometer were made using YBCO films deposited on the $LaAlO_3$ (100) and $SrTiO_3$ substrates. The step structure on the substrates were made using argon IBE process with the beam energy ranges of 250-600eV and the beam intensities of 0.125-0.5 mA/cm^2 as explained in earlier section.

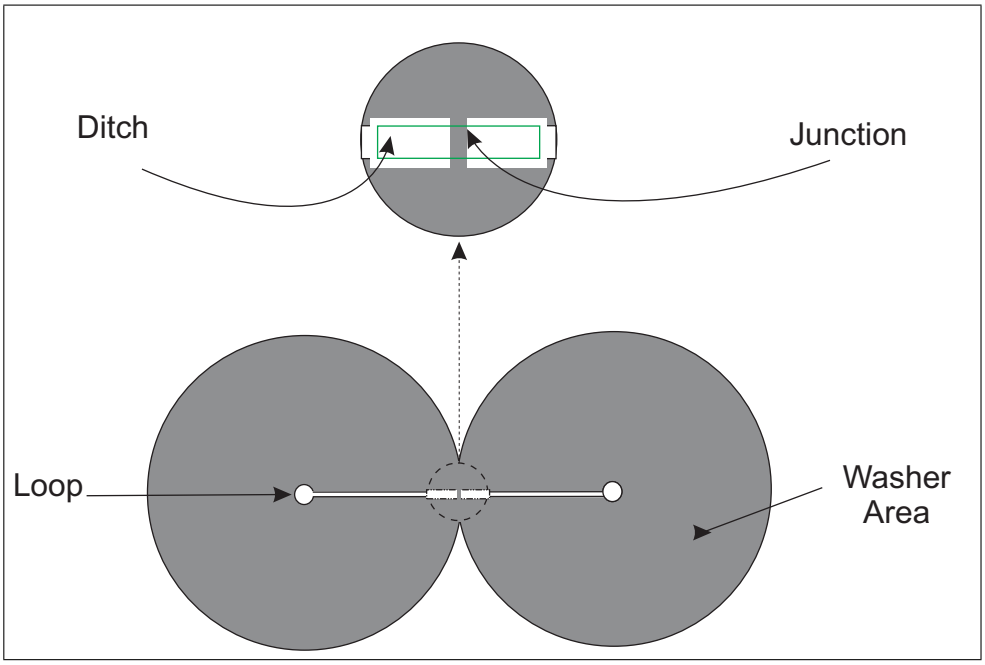

Figure 3.1: SEJ rf-SQUID gradiometer layout.

The gradiometers were made typically using layouts with **washer areas with 1.5mm diameter**, **loop areas of** $75 \times 75\mu m^2$ and a **baseline of 1.5 mm** as shown in Figure 3.1.

3.2.1.2 SEJ Magnetometer design

The used Step-Edge Junction rf-SQUID magnetometer design is shown in Figure 3.2. The magnetometer were made using a layout with a **3.5mm diameter**

washer and typically a **loop size of** $100 \times 100\mu m^2$ **or** $150 \times 150\mu m^2$ giving an inductance of 156pH and 235pH, respectively.

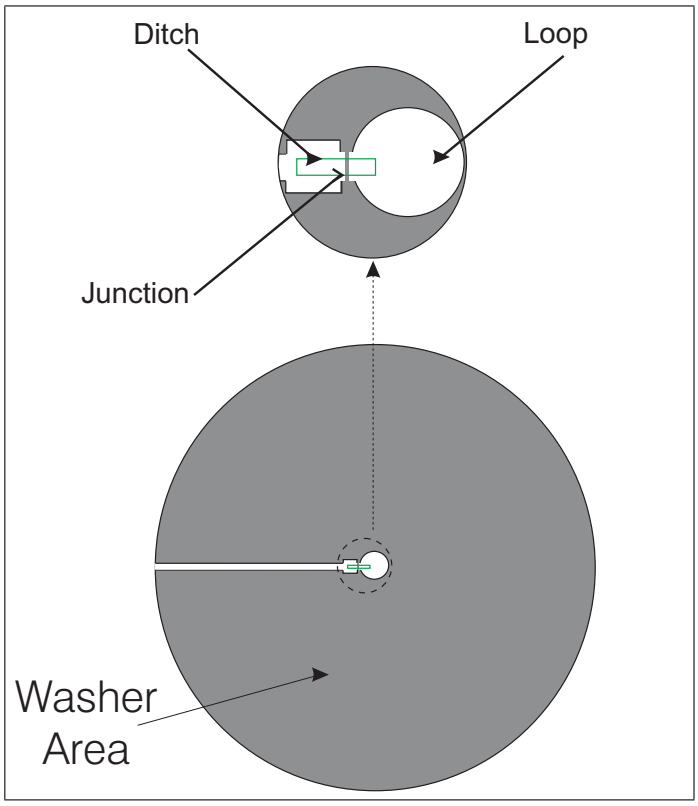

Figure 3.2: SEJ rf-SQUID magnetometer.

The control of parameters of the SEJs and the SEJ rf-SQUIDs is interpreted to be partially difficult due to unwanted serial junctions obtained in this structure as shown in the following Fig. 3.3(b). The shown configurations in the Figure results in four junctions at the sides of a ditch with sharp step structures. The corresponding twin junctions on the sides of the ditch (junctions 1 compared to 3 and 2 compared to 4 shown in Fig. 3.3(b) will have close values for a perfectly symmetric step structure. This will further complicate the control of the critical current of the junction, I_{cj}, for the SQUIDs or any device based on this type of the JJs. The asymmetric SEJ design shown in Fig. 3.3(a) [66], prevents this further complication of the close I_c values of the junctions easing the further control of the operating temperature range of the devices by controlling the I_{cj}.

The asymmetric design determines the working junction of the SQUID by

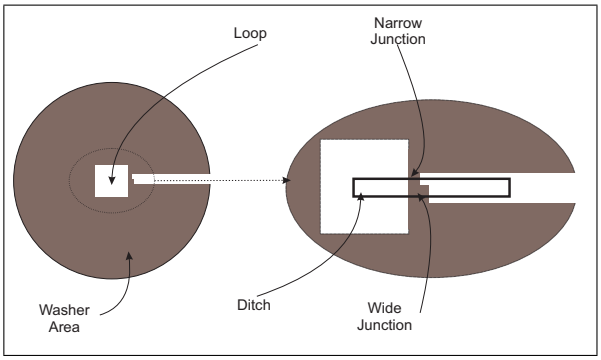

(a)

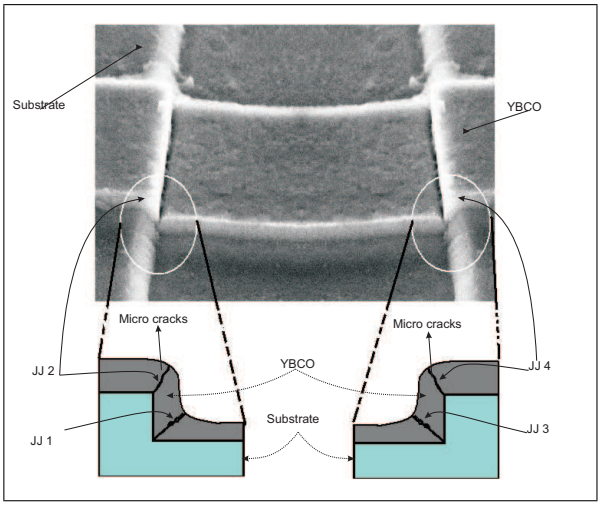

(b)

Figure 3.3: SEJ structure and the asymmetric grain boundary junctions shown for a rf-SQUID magnetometer.[2]

separating the I_c of the junctions at both sides of the ditch carrying similar structure. The I_c of the properly prepared SEJs on a chip (e.g, prepared using CIBE process) are found to be proportional to the junction width. Hence the narrower junction in Fig. 3.3(a) will be the determining junction when the film thickness and the step height are also tuned for that (i.e., the other junctions will not see a current above their I_{cj}). This is while the width of the wider junction is still small enough (less than a few μm) to prevent additional noise caused by flux flow along the GB. Also some rf-SQUID magnetometers have been made using the above design (i.e asymmetric SE-junction pattern). The junction of

the SQUIDs could be characterized by opening their magnetic field concentrating washer area using micro-scriber (will be explained latter in this chapter). The optimal operating temperature of the SQUIDs could be tuned to 77K by control of the step height as explained in the followings.

The SQUIDs were designed to be characterized by a conventional L-C tank circuit while the designs could further be modified to obtain lower inductance value when combined with coplanar resonators and flux focusers. SQUIDs were also made with dc-SQUID layout designs including option for the $I - V$ characterization of the junction types using four-probe configuration as shown in Fig. 3.7(a) at the same time as shown in Figure 3.4.

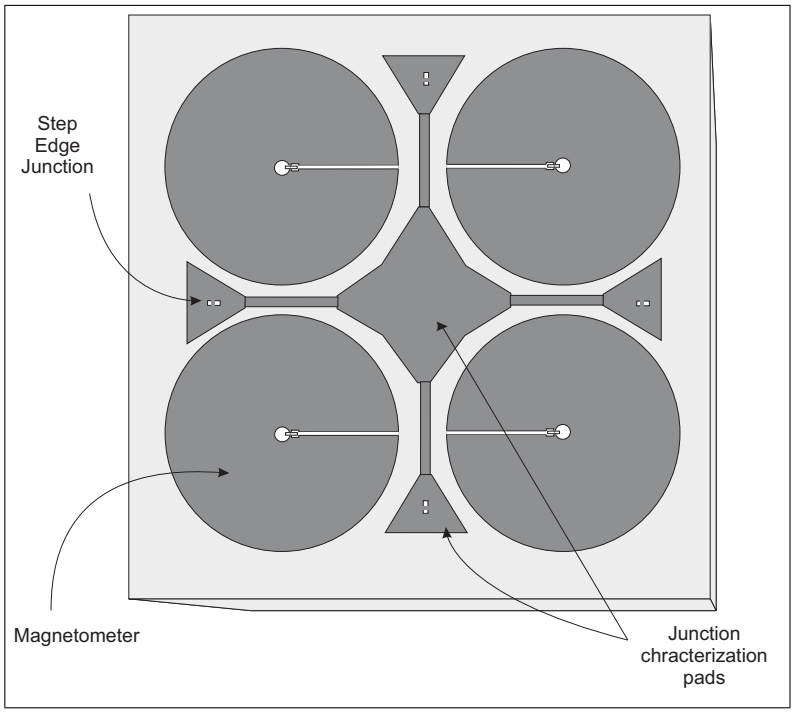

Figure 3.4: Chip layout of the SEJ magnetometers with separate SEJs in dc-SQUID configuration in order to characterize the junctions for dc characteristics in parallel to rf-SQUID characterization [2].

3.2.2 Bi-Crystal grain boundary Junction rf-SQUID

An extensive use of Bi-Crystals has been in making devices such as SQUIDs where narrow bridges of the YBCO across the substrate grain boundary (GB) serves as a weak link, Josephson Junction (JJ). While the Bi-crystal substrates offer very simple fabrication for the mono-layer SQUID structure, the layout design for the rf-SQUIDs on them is limited by the long GB across the substrate. The extended GB across the substrate creates unwanted weak links such as in the washer areas of the conventional thin film planar rf-SQUID magnetometer and gradiometer layout designs [63]. The large YBCO weak link across the GB of the substrates is a major source for low frequency or $1/f$ type noise in the SQUIDs due to the motion of fluxons along the GB [63], [43]. This is in particular when the SQUIDs are operated outside the magnetic shield or under applied magnetic fields making the bi-crystal unfavorable substrates for the rf-SQUIDs. There have been some efforts to reduce this noise by making artificial pinning sites at the GB to prevent the flux motion along the weak link [63], [43]. The artificial pinning sites were reported to be effective for certain magnetic field values [63]. This is while there have been contradictory reports on the effectiveness of the artificial pinning sites as pinning centers for fluxons [71], [70]. In this work we report on the results of developed YBCO rf-SQUID magnetometers and gradiometers made using proposed layout designs on the bi-crystal substrates. The goal is to reduce the $1/f$ noise of the SQUIDs associated with flux motion in the film along the substrate GB, while avoiding the implementation of artificial pinning sites. The effect of the design parameters on the noise of the SQUIDs as well as the $I-V$ characteristics of the junctions of the SQUIDs is discussed here. Also the flux to voltage transfer function (V_{spp}) modulation by the applied B_a as well as the characteristics of the junctions of the rf-SQUIDs are discussed in the following.

3.2.2.1 Bi-crystal Gradiometer design

rf-SQUID layout designs based on asymmetric multi-junction structures for BGBJ, on symmetric 36.8^o angled bi-crystal $SrTiO_3$ substrates, were used to reduce the $1/f$ noise of the devices [69], [91]. The SQUIDs were made with about

0.8 to 1 μm wide narrow junctions, and 2-4 μm wide dummy junctions, resulting up to 4/1 junction width ratios [69], [92]. The used layout designs for the BGBJ rf-SQUIDs magnetometers and gradiometers on bi-crystal substrates are shown in Figure 3.5. As it is shown in the figure, the gradiometer layout has three junctions in parallel across the GB. The smaller middle junction of the gradiometer layout is considered to be the determining JJ of the device.

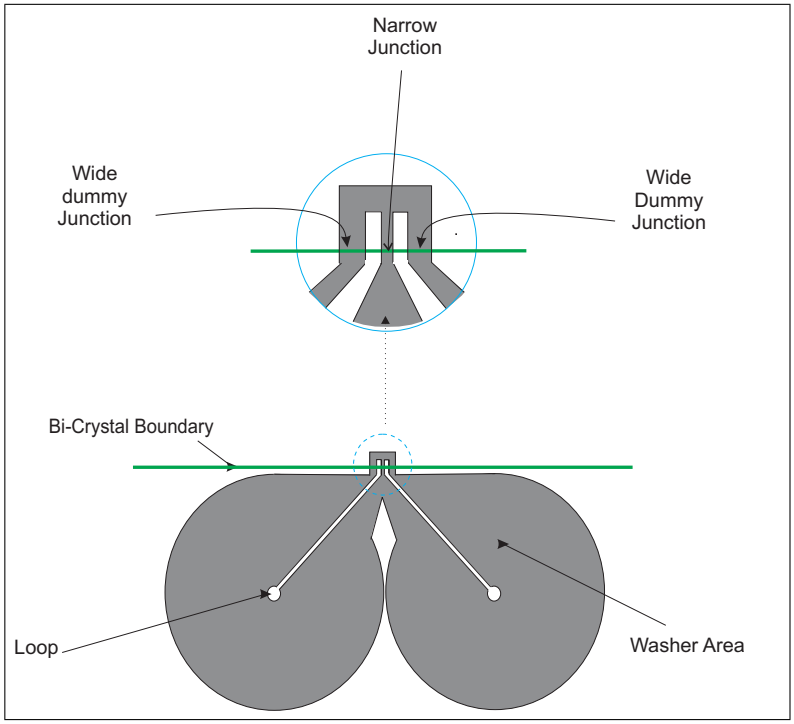

Figure 3.5: Asymmetric rf-SQUID layout design of tri-junction gradiometer. [3]

The gradiometer design has washer areas of **1.7** mm^2 **(1.5mm diameter)**, **1 mm long slit** , and **75** μ**m diameter loop** leading to an inductance of about 590 pH. As shown from the figure, the washer area of the design has been modified compared to conventional designs in order to reduce the length of the slits while avoiding major reduction of the coupling coefficient between the SQUID and the tank circuit.

3.2.2.2 Bi-crystal Magnetometer design

Layout designs based on asymmetric multi-junction structure for rf-SQUID magnetometers on bi-crystal substrates have been used as shown in Figure 3.6.

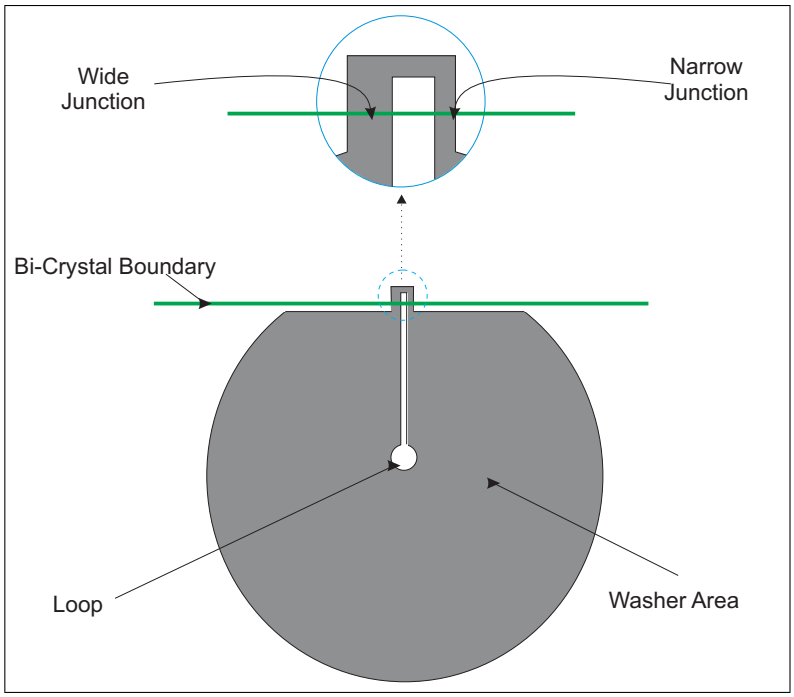

Figure 3.6: Asymmetric rf-SQUID layout design of bi-junction magnetometer.[3]

The magnetometer layout has two asymmetric junctions across the substrate GB. Where in this configuration wider junction works as dummy and narrow junction is the working junction. In both designs the wider junctions are the undesired weak links minimized to reduce the associated flux noise. the magnetometer design has a washer area of $\mathbf{7}mm^2$ **(3mm diameter)**, **200 μm long slit**, and **50 μm diameter loop** leading to an inductance of about 180 pH.

3.2.3 SQUID-junction characterization methodology

In order to measure the critical current of the JJ of the SQUID, we required to open washer area of the SQUIDs. Much care should be taken while opening the

washer area because it may affect the critical current of the JJ changing the β_L. This way the measurement for ΔB_0 and ΔB_{0-V} will not be reliable. Opening the SQUID washer area using photolithography process makes it tricky as heating $YBa_2Cu_3O_{7-\delta}$ can cause reduction in oxygen contents which will lead to a change in the characteristics of JJs so one needs to avoid heating the under observation sample, which can not be the case due to the requirement of soft bake and hard bake for photolithography. Secondly while having Gold contacts it is required to clean the sample surface which introduces mechanical stresses directly affecting the junction propertied.

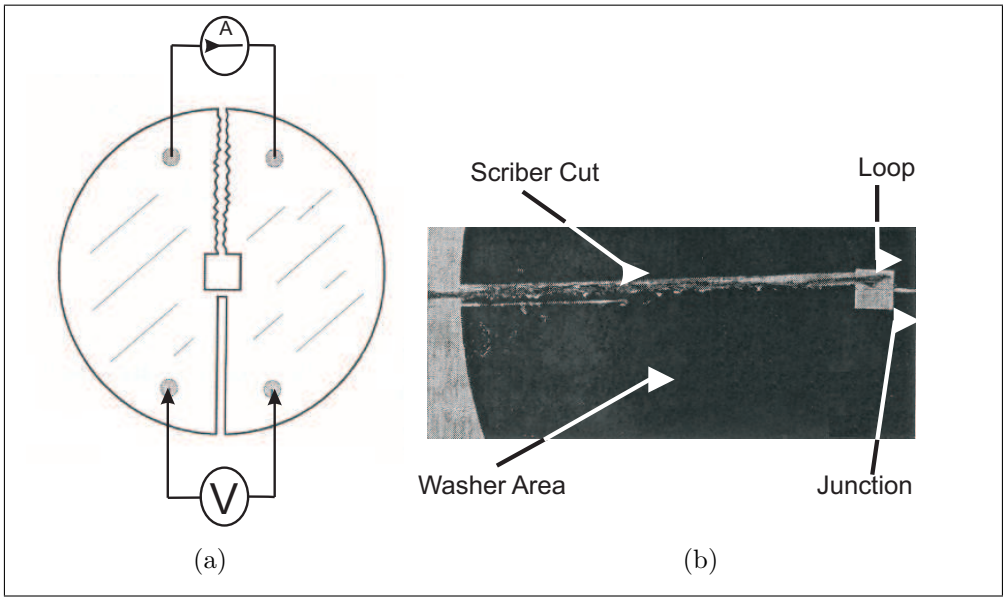

Figure 3.7: (a) Schematic diagram of an rf-washer-SQUID with open ring and ohmic contacts for characterization of $I-V$ characteristics in four-probe configuration. (b) A photograph of the washer of SQUID, which is mechanically opened using diamond scriber.

Due to these considerations the SQUID was mechanically opened with a diamond scriber under a microscope at ambient temperature. The diamond needle could be positioned with an accuracy of $\sim$ 20 μm in vertical direction and $\sim$ 50 μm in horizontal direction. This way SQUID washer was opened successfully with out having any of the problems stated above. A photograph of an opened rf-SQUID magnetometer is shown in Figure 3.7(b).

Ohmic contacts were made using 25 μm gold wire with ultrasonic bonder at room temperature directly on to the surface of the YBCO with optimized parameters of wedge bonder. this way evaporation of the Gold contact pads were avoided. Samples were wire bonded with a non magnetic chip carrier. In order to improve the thermal contact and for the stability of the temperature during measurements, samples were attached with chip carrier using either Epizon N grease or silicon vacuum grease. It has been shown that aluminum wire bonding provides semi-conducting contacts with contact resistance up to 100Ω where as Gold wires provide metallic contact with resistance down to $< 5\Omega$. Each contact used for four-probe measurement was wire bonded with 5-6 gold wires in order to improve the mechanical stability. It has already been shown that characteristics of the SQUIDs and, their JJs parameters are not affected by using this mechanical scriber and wedge bonder [93].

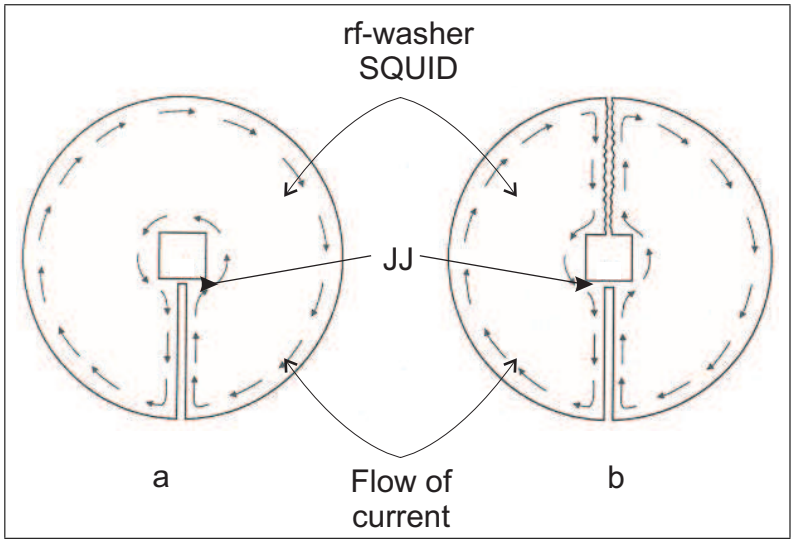

Figure 3.8: Schematic sketch of the current flow in a) SQUID and b) SQUID with opened SQUID washer area

Another consideration related with washer area is the behavior of circulating current density through the junction. This can directly affect the period of the magnetic field, ΔB_0 and would make it impossible to compare the $I_c(B)$ and $V_{spp}(B)$ of the rf-SQUID before and after cutting. But as shown in Figure 3.8 it can be seen that the current density across the junction remains the same by canceling the effect of current along the cut areas due to their opposite directions,

as shown in Figure 3.8(b). So the over all current density across the junction remains the same as it was in the condition of unopened case shown in Figure 3.8(a). This conclusion is important and helps to safely investigate the correlation of ΔB_0 and ΔB_{0-V} of the SQUIDs.

3.3 Characterization setup

Schematic sketch of the characterization setup is shown in Figure 3.3. Cryostat bath is made of Glass fiber reinforced Plastic, GfK with an opening of 55 mm diameter and it has the capacity to hold the sample at 77K for about three days. In order to avoid the effect of magnetic field, the measurements have been done in a dewar with three layer μ-metal-cylindrical shield with wall thickness of 1mm.The shielding container has outside diameter of 560mm and height of 1050mm, with an interior diameter of 500 mm and height of 990 mm. This way earth magnetic field can be reduced down to < 20 nT.

Sample holder for both types of rf-coupling techniques, LC tank circuit and coplanar resonators, have been developed and attached with GfK. The 50Ω inlets for rf-electronics were protected for high frequency electro-magnetic influence with proper shielding and for electro-static shielding by appropriate grounding. rf-Electronics is operated with low noise, battery powered voltage supply of $\pm$15V. Amplitude and frequency of the external current modulation for the SQUID sensors was produced with the help of function generator FG 1617. SQUID signal which indicates the flux to voltage transfer function, V_{spp}, was measured by a digital oscilloscope (Tektronix TDS420A). Spectrum analyzer (HP 35670A) with frequency range of 100 KHz has been used in order to measure the noise characteristics of the SQUID, using the phase lock loop technique.

In order to produce an homogeneous magnetic field at the samples two Helmholtz coils A and the coil B were designed and used as shown in Figure 3.3. Coil B with diameter of 48 mm is attached with the sample holder in order to produce magnetic field parallel to the sensor surface with $\alpha = 0^o$ to $\alpha = 6^o$,

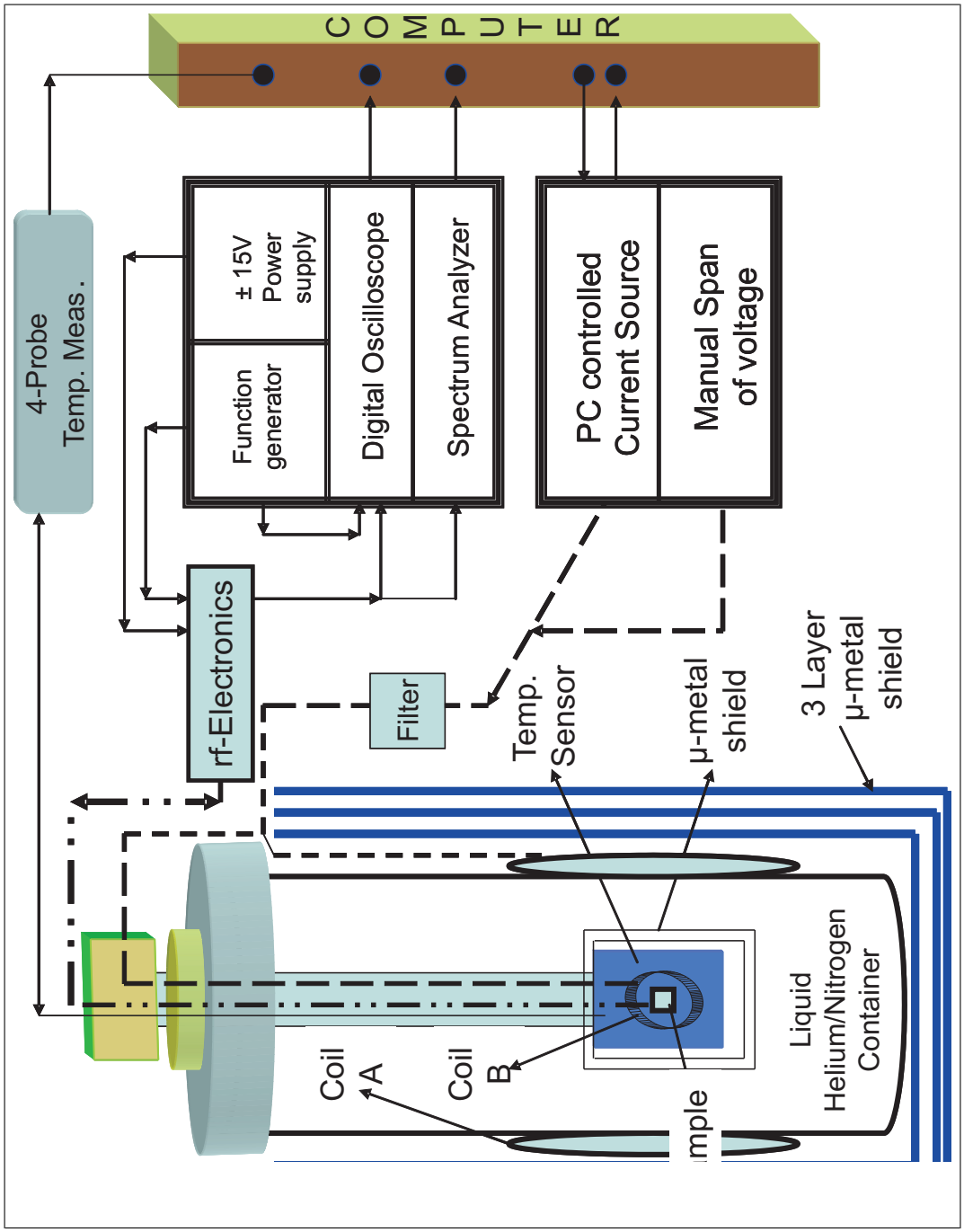

Figure 3.9: Schematic sketch of the measurement setup for the characterization of rf-SQUID at liquid Nitrogen/Helium temperatures.

while coil A with coil diameter of 380 mm was attached to dewar to produce magnetic field with angle of 90 degree [93]. Current to the coils to adjust large fields was applied by using either computer controlled current supply or manually adjustable voltage source with a maximum output voltage of ±30V (Voltcraft TNG 235). In this way maximum magnetic flux densities up to 700 μT were achieved with type A coil and 6 mT with coil B. In order to measure the amount of the applied field, voltage across a series resistance with the coil was measured. Where as for small amount of fields, computer controlled power source [74] is used, which supplies a maximum current up to 38 mA. This way characterization of SQUID signal, V_{spp}, with respect to applied field can be automated by recording the output using the LabView program written at the institute of Thin Film and Ion Technology [94].

The calibration of the the Helmholtz coil was done by using flux gate magnetometer [95] and with Hall probe (Gauss meter of 912, RFL Electronics), which gives the sensitivity of measurement of magnetic field at the location of SQUID with an error of approximately 5%. This way electromagnetic disturbances, which are produced in particular by line frequency (50 Hz), can be reduced and the reliability of the data accusation for voltage to transfer function of the SQUID and noise measure can be increased.

3.4 Measurements and Analysis of SEJ YBCO rf-SQUIDs

3.4.1 Step structure and JJ width dependence of SQUID characteristics

Effects of different step structures on the V_{spp} and the junction $I-V$ curves of the SQUIDs were investigated. Three major step structures were reproducibly made namely the ramp type, smooth ramp type, and the sharp steep CIBE step structures where as the last one is shown in Figures 2.4 [5], [67]. The JJs on both the types of the ramp type steps had relatively high I_c. The sharp step structures, in particular the CIBE steps, favorably provided very low I_{cj} compared to that of the ramp type steps. This allowed reproducible fabrication of the rf-SQUIDs with the desired operating temperature ranges using a few micron wide bridges and 200 nm thick superconducting films.

While the I_c of the JJs made on the ramp type junctions were not considerably controllable by the depth of the ditch, the I_c of the junctions on the CIBE steps were found to be strongly sensitive to the step height. For a film thickness of about 200 nm, the I_{cj}s were found to systematically decrease as the step height increased from about less than 150 nm to over 300 nm, the investigated range. This step height dependence of the I_{cj} allowed the controlled shift of the operating temperature range of the SQUIDs to the desired window as shown for the junctions widths of 3 μm in Figure 3.10.

SQUIDs with junction widths up to 5 μm were made of 200 nm thick films on $LaAlO_3$ substrates with CIBE steps. For SQUID junction widths of 1 μm and less, very low yield and noisy devices were obtained. This is interpreted to be caused by the precipitates in the narrow bridges across the ditch. While the operating temperature range of the SQUIDs with 3 μm and 5 μm bridge widths were typically close, the operating temperature range of the 2 μm wide bridge SQUIDs were considerably lower as shown in Figure 3.10. This could also be

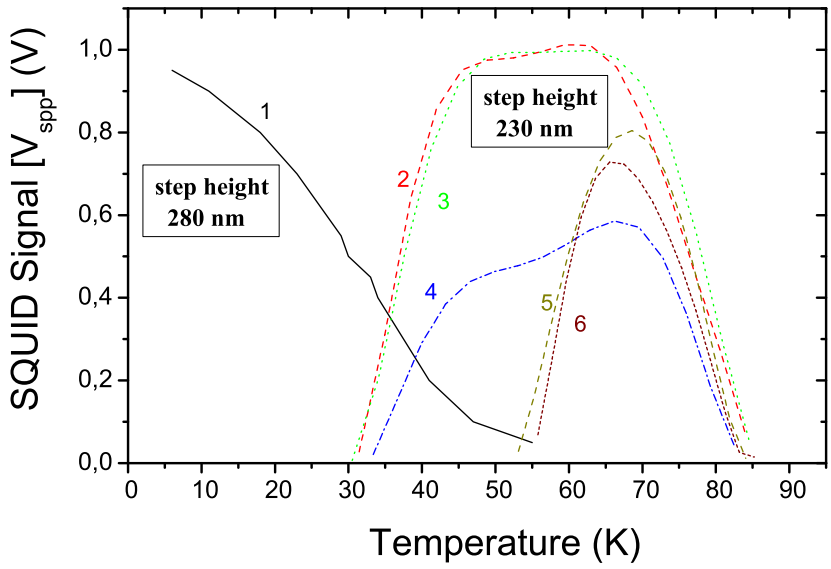

Figure 3.10: V_{spp} vs. T of SQUIDs made of 200nm thick YBCO films on $LaALO_3$ substrates with CIBE steps. The solid lines show the V_{spp} of 2-5 μm wide junction gradiometers for step heights of 230 nm (rigt) and 280 nm (left). The dashed lines show the V_{spp} of 3 μm wide junction magnetometers on 260 nm deep steps.[4]

associated with the density and size of the precipitates in the films. Junctions made of 200 nm thick films showed a systematic increase of I_{cj} from about 50 μA to about 1 mA at 4.3 K for junction widths of 3 μm to 8 μm.

3.4.2 Step height dependence of SQUID characteristics

The dependence of the operating temperature range of the SQUIDs on the step height was investigated by measuring the amplitude of the flux-voltage transfer function signal, V_{spp}, of the devices versus temperature. The dependence of the operating temperature rang on the junction structure for magnetometers are also shown in Figure 3.11.

The V_{spp} of rf-SQUID magnetometers with 2 μm to 3 μm wide junctions on $LaAlO_3$ with various CIBE step structures are shown in Figure 3.11. "SQUID 1"

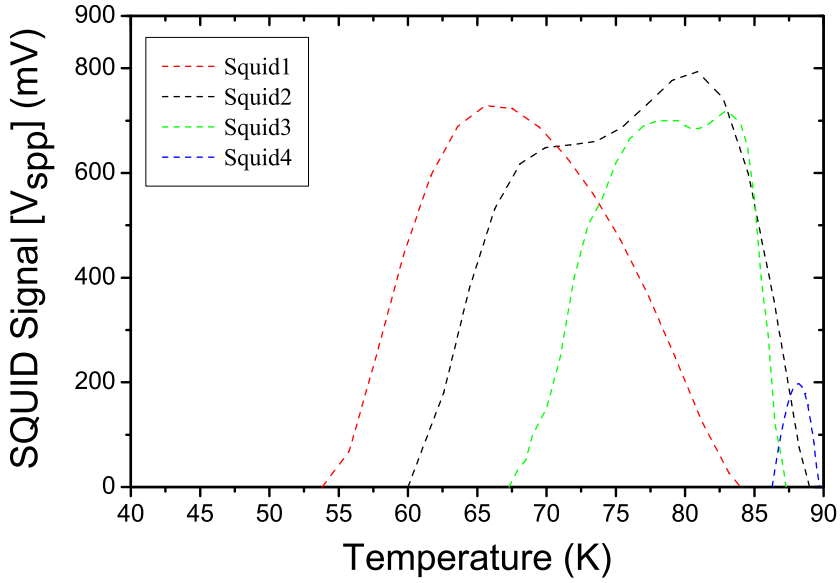

Figure 3.11: Flux to voltage transfer function signal, V_{spp}, versus temperature of rf-SQUID magnetometers with 100 μm $\times$ 100 μm loops. "SQUID 2" has a 205nm deep ditch and SQUIDs 3 and 4 have 135nm deep ditches, made using the optimized CIBE process. "SQUID 1" has a 275nm deep ditch, made using un-optimized CIBE process. The junction width of "SQUID 3" is 2 μm, and the other devices have 3 μm wide junctions [5].

with a 275nm deep ditch, showed an operating temperate range close to "SQUID 2" with a 205nm deep ditch. Both devices have 3 μm wide junctions. This is interpreted to be due to the ramped surfaces at the bottom of the ditch, close to the step edges of "SQUID 1" made using un-optimized CIBE parameters, leading to a step height close to that of "SQUID 2". The ramp type substrate surfaces at the steps of "SQUID 1" also led to similar defected film growth as shown (Figure [1.5c]) 2.4(c) [5], leading to a higher $1/f$ noise of about 40 $\mu\Phi_0/\sqrt{Hz}$ at 10Hz.

Decrease of the step height to 130nm, using optimized parameters, resulted in a narrow and high operating temperature range for the SQUIDs, close to the T_c of the YBCO films, as shown for "SQUID 4" in Figure 3.11. Decrease of the junction width for the same step height reduced the operating temperature range to the desired temperature window around 77K. "SQUID 3", made on 130nm

deep CIBE steps with 2 μm wide junction, showed an operating temperature range close to that of SQUID 2, with 205nm deep step and 3 μm wide junction. The flat surfaces of CIBE step structure of SQUID 3, obtained using lower ion beam in the IBE process, also led to uniform high quality film inside and outside of the ditch, leading to lower white noise and low $1/f$ noise. The noise spectra of the sample measured at liquid nitrogen temperature using conventional LC tank circuit, is shown in Fig. 3.12, and white noise level of about 15 $\mu\Phi_0/\sqrt{Hz}$ (135 $ft/\sqrt{Hz}$ for the bare SQUID) was measured.

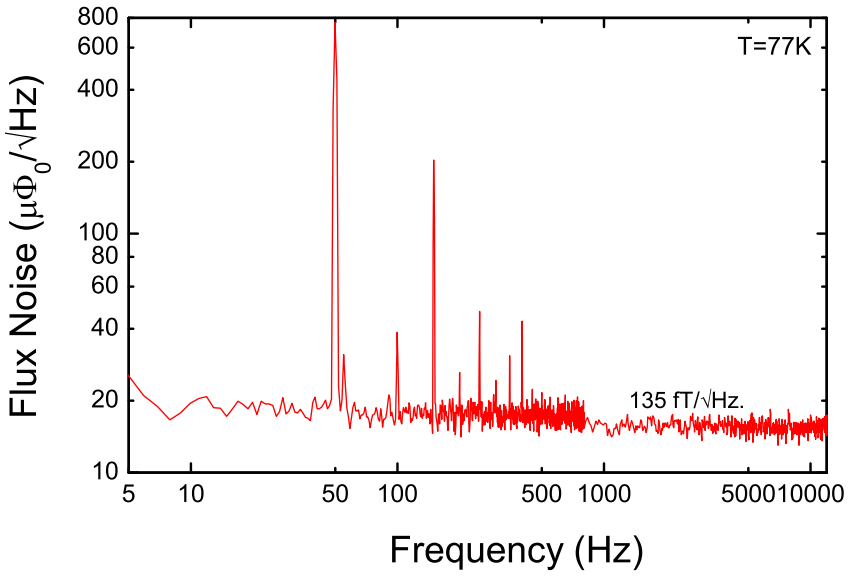

Figure 3.12: The noise spectra of the sample measured at liquid Nitrogen temperature using conventional LC tank circuit [5].

3.4.3 Film properties dependence of SQUID characteristics

The I_{cj} of the CIBE SEJs and consequently the operating temperature range of the SQUIDs was also found to be dependent on the film thickness. The I_{cj} of the SQUIDs increased with increase of the film thickness for the investigated film thickness of 120 nm up to 300 nm. This with the observed increase of the I_{cj}

by the increase of the junction width led to an effective area for the junctions proportional to the geometric junction area. While the $I-V$ characteristics of junctions on one chip showed an increase of the I_{cj} as a function off about the geometry of the junction area, the I_cs from one chip to another varied considerably showing high sensitivity to the growth of the films.

Film morphology affects the $1/f$ type noise, higher for non homogeneous structures which come from conventional IBE, where as step produced by CIBE process shows low $1/f$ noise due to smooth films on these steps. This is mainly due to the fact that conventional IBE causes rough substrate surface at the bottom of the step due to which high quality film morphology can not be obtained. This also reduces the yield and causes instability in the SQUID characteristics, where as the working temperatures range also shift towards low temperature showing degradation of the I_{cj}.

3.4.4 $1/f$ noise and the temperature dependence of the noise characteristics of SEJ SQUIDs

Two temperature dependencies for the low frequency $1/f$ type noise are observed for the SQUIDs made on the CIBE steps. One type of $1/f$ noise was found to decrease as the temperature was decreased and the 2nd type decreasing as the temperature was increased.

The increase of the low frequency noise by decrease of the temperature is interpreted to be due to the increase of the I_{cj} and its associated fluctuations. This type of noise characteristics is mostly observed in the SQUIDs with very smooth and precipitate free films but having minor structural defects right at the step edge. The second type of the $1/f$ noise increased with decreasing the temperature. The source for this noise is interpreted to be due to the flux hopping mechanism in the film of the washer area of the SQUIDs close to the loop. The increase of the noise at high temperatures is associated to the increase of the thermal activation energy for the fluxons and lowering of the barrier heights. This noise characteristics is mostly observed in the samples made of the films

with relatively high density of precipitates and is found to increase as the density of the precipitates in the film increased. For SQUIDs with high quality films on the CIBE steps none of the above low frequency noise behavior was observed while the white noise was mainly determined by the V_{spp}.

3.4.5 Magnetic Field Dependence of SEJ SQUIDs

The stability of the amplitude of the flux voltage transfer function of the SQUIDs, and the suppression of I_c of their junctions by the magnetic field suppressing their signal to voltage transfer function, is studied in this section. The obtained results of the investigation on the influence of external magnetic fields on V_{spp} depending on the junction width of SEJ rf-SQUIDs is presented in the followings. The V_{spp} was measured at the output of the SQUID read out electronics as a function of an external magnetic field applied to the zero field cooled (ZFC) SQUIDs at 77K.

The field was produced by a calibrated solenoid explained in the setup section. The SQUIDs were also operated in flip chip configuration with two different coplanar resonators with integrated flux concentrator [61]. This was done with either a 8mm rectangular (SR8) or a 13.4 mm circular (SR13) shape resonators. Two distinct relatively high and low B_a sensitivities were observed for the field dependence for I_c of the isolated test junctions, showing two distinct B_a dependencies. The field sensitivity of the test junctions was correlated to that of the SQUID junctions through the effective area of their patterns [96]. The field dependencies of V_{spp} of 2-3 μm wide junction rf-SQUIDs with high and low B_a sensitivities are shown in Figure 3.13(a) and (b), respectively. The B_a dependence of the I_c of the SQUID junction also followed that of the V_{spp} of the SQUIDs [77], [69]. Four probe $I-V$ measurements of some of the already characterized SQUIDs were performed. $I_c(B)$ of the SQUID junction was measured in a magnetic field normal to the film surface using a 30 μV criterion. To determine I_c and β_L in the presence of large thermal fluctuations ($\Gamma > 1$) at T = 77K, measurements of the differential resistance, R_n= dV/dI were performed with standard lock-in technique as discussed in detail before.

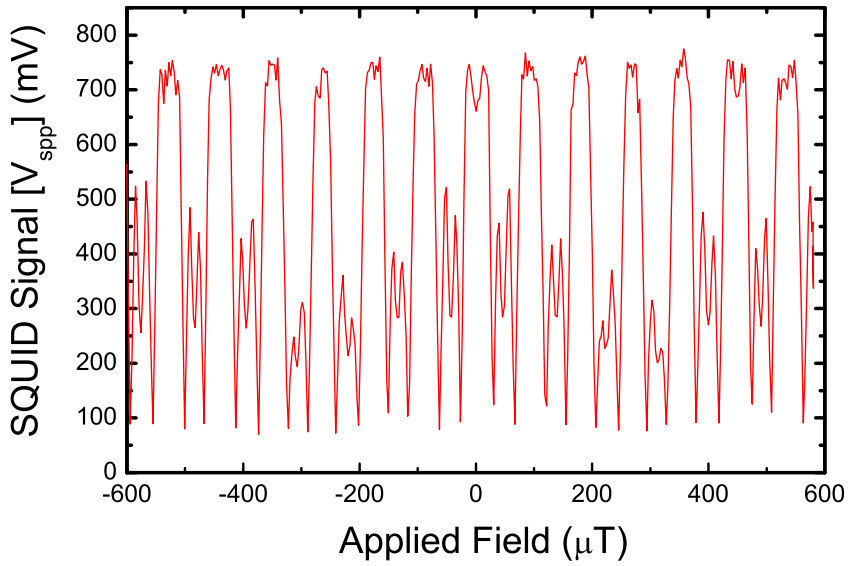

(a)

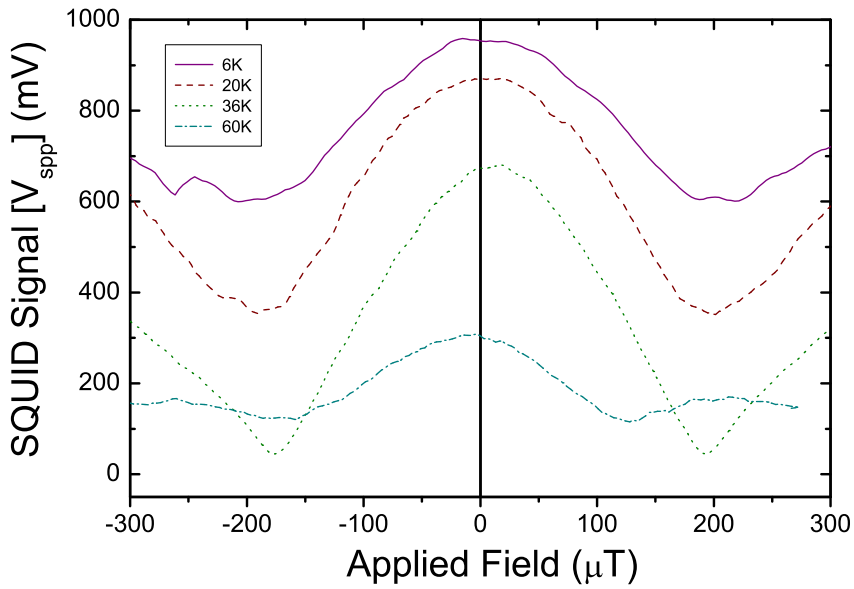

(b)

Figure 3.13: a) Normalized magnetic field dependence of V_{spp} of a high field-sensitive 2μm wide junction SEJ rf-SQUID b) Magnetic field dependence of V_{spp} versus temperature of a low field-sensitive SEJ rf-SQUID.

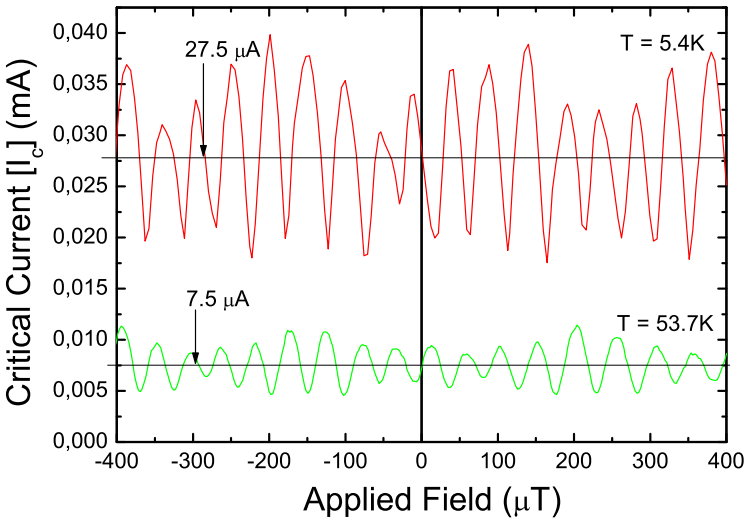

Figure 3.14: Magnetic field dependence of I_c of the junction of high field-sensitive rf-SQUID at low and high temperatures.

The magnetic field dependence of the I_c of the SQUID junction with high field sensitivity shown in Fig. 3.14, followed that of the V_{spp} of the SQUID with a slight discrepancy associated to calibration accuracy of the fields. The magnetic field dependence of the transfer function V_{spp} of the sensors showed one main maximum enabling determination of the value of the magnetic field at the first minimum, ΔB_{0-V}. For about 30 % of the field-sensitive devices, a Fraunhofer-like dependence of V_{spp}(B) was observed. As observe from Fig. 3.13(a), there is also a lower modulation of the V_{spp} indicating also the existence of the effect of a low B_a sensitive junction in series. This modulation follows the trend with the W compared to that of the 3μm wide low B_a sensitive SEJ device in Fig. 3.13(b). The multiple modulation types in Fig. 3.13(a) is interpreted to be due to the field dependent interferences in the V_{spp} of the inevitable serial junctions in the SEJ rf-SQUIDs [59], [60], [5]. The study of the high B_a sensitivity of our SEJ rf-SQUIDs and its correlation with their junction parameters is previously reported [62], [77].

The V_{spp} of the low B_a sensitive devices dropped by less than about 10% under $B_a \sim 50\mu T$ and as also observed from Fig. 3.13(b), did not lead to any systematic

temperature dependence associated to $\lambda_L(T)$. The field dependence of the I_c of the junctions of the SQUIDs with similar low B_a sensitivities also showed low B_a dependencies in agreement with the field dependencies of the corresponding SQUIDs [77].

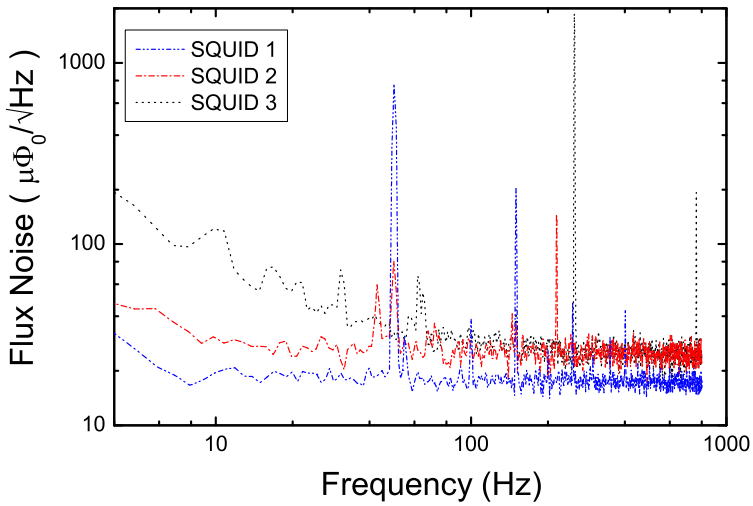

Figure 3.15: Noise spectra of rf-SQUIDs with high field-sensitivity (SQUID 1) and low field-sensitivity (SQUIDs 2 and 3) characteristics. SQUID 3 is measured in liquid Nitrogen using optimal LC tank circuit.

The study of the drop of the V_{spp} of high B_a sensitive devices led to the need of rf-SQUID layout designs with junction widths in the range of 0.6-1.2 μm to obtain magnetically stable devices for applications in unshielded environment [62], [77]. This is while low B_a sensitive SEJs resulted in 2-3 μm wide junction magnetically stable rf-SQUIDs proper for operation under earth magnetic field. With the consideration of the typically lower J_c and higher ρ_N of the SEJs compared to that of the BGBJs, the low field-sensitive SEJs led to the preference of the use of SEJ technology for fabrication for the rf-SQUIDs for operation at 77K. Though a systematic investigation for obtaining a higher yield for low field-sensitive SEJs is further needed. As shown in Fig. 3.15, the studied SEJ rf-SQUIDs in this work with low B_a sensitivities also showed lower $1/f$ noise levels compared to that of the higher B_a sensitive devices.

3.5 Measurements and Analysis of Bi-crystal YBCO rf-SQUIDs

3.5.1 General characteristics related to working temperature and $1/f$ noise

Here we present an overview of the general observed characteristics without going in details. For further detail see the published work or scheduled publications.

- $I-V$ characteristics of the junctions were measured and all the characterized junctions showed resistively shunted junction (RSJ) behavior.
- Based on the I_c versus temperature and the effective width of the BG-BJs, an approximate optimum working temperature range close to 77 K was expected for our devices with 0.8 to 1 μm wide operating junction in the designs [69]. This was based on optimum rf-SQUID parameter $\beta_L = 2\pi LI_c/\Phi_0$, where L is the SQUID inductance, for the used layouts and the expected I_c for the smaller junction of the SQUIDs.
- Relatively large variation of the critical currents from one SQUID to another was observed which is associated to the non-uniformity of the GB of the substrate showing many imperfections along the grain boundary.
- The normal resistance of our bi-crystal GB JJs, R_N, were also measured and found to decrease consistently as the temperature increased contrary to some previously reported results [69]. The R_N of the 1/4 width ratio parallel junctions of the characterized magnetometer decreased almost linearly from 0.67 Ω to 0.64 Ω when the temperature was increased from 5 K to 87 K. The R_N of the characterized gradiometer junctions with 3/1/3 width ratios (measured in parallel) also decreased from 5.9 Ω to 4.2 Ω when the temperature was increased from 8 K to 76 K.
- The $1/f$ noise of the samples decreased from 120 $\mu\Phi_0/\sqrt{Hz}$ to about 70 $\mu\Phi_0/\sqrt{Hz}$ at 10 Hz frequency when the junction ratios were decreased from

4/1 to 2/1. The decrease of the low frequency noise with decrease of the width of the 2nd junction down to 2 μm is interpreted to be due to the reduction of the unwanted large weak link across the GB. The large YBCO weak link across the GB is a potential path for flux trapping and flux motion along the weak link being a major source of low frequency flux noise in the SQUIDs [43], [64].

- The two types of the temperature dependencies of the $1/f$ type noise behavior have also been observed the BGBJ for rf-SQUIDs [25], [4]. Normaly one is found to decrease as the temperature is decreased, associated with flux hopping mechanism in the YBaCuO film, and the 2^{nd} type noise is measured to decrease with increase of the temperature, associated to the quality of the junction and the critical current fluctuations. This is discussed in further details in previous section.

- The white noise level of all the devices were measured to be minimum at middle of the operating temperature range of the SQUIDs where the V_{spp} was maximum.

3.5.2 Magnetic field dependence of bi-crystal based SQUIDs

A SQUID based imaging system application requires stable sensor operation in a moderately shielded or unshielded environments. This is especially important for SQUIDs which might be exposed to a fraction of magnetic field variations of up to 50μT in the Earth's magnetic field. This magnetic field variation may result in an increased white noise level due to Josephson vortex penetration into the junction as well as $1/f$ noise increase. To obtain SQUIDs for stable operation in a given magnetic field, it is important to determine the range of the required junction width, W.

The stability of the amplitude of the flux-voltage transfer function, V_{spp}, is the

direct criterion for stable SQUID operation. A suppression of I_c leads to a reduction of the parameter $\beta_L = 2LI_c/\Phi_0$ (rf-SQUIDs), where L is the SQUID inductance. A suppression of I_c leads to a reduction of the parameter $\beta_L = 2\pi LI_c/\Phi_0$ (rf- SQUIDs). V_{spp} has a maximum at about $\beta_L = 1$ where for smaller values, $V_{spp}(\beta_L)$ is monotonically decreasing. Therefore, in the case of $\beta_L \sim 1$, a suppression of I_c should also lead to a suppression of V_{spp}. In this section the obtained results of the investigation on the influence of external magnetic fields on V_{spp} depending on the junction width of BGBJ rf-washer SQUIDs is presented. The width dependence of B_{0-V} is compared to different model predictions. Finally, the suppression of I_c will be correlated to the suppression of V_{spp} by direct measurements of I_c, β_L, and $I_c(B)$ using samples with opened SQUID loops. To achieve stable operation in magnetic fields, the junction width has to be small as concluded from the study on the BGBJs.

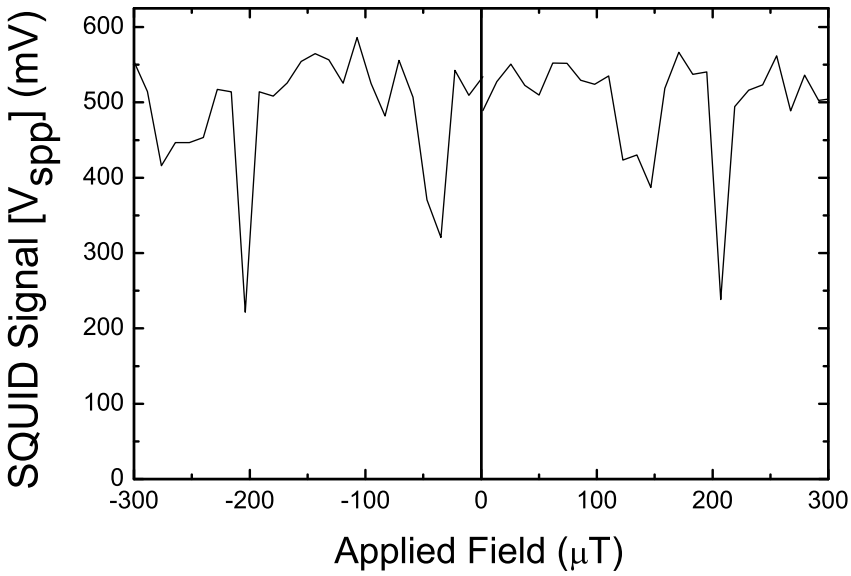

Figure 3.16: Magnetic field dependence of flux voltage transfer function signal, V_{spp}, of asymmetric junction bicrystal-GB rf-SQUID.

Based on the B_a dependence of the I_c of the BGBJs, a very low suppression of V_{spp} of zero-field cooled BGBJ SQUIDs were expected under the earth magnetic field. This was also verified by the direct field sensitivity measurements of the

devices. This was based on the consideration of the width of the narrow junction of the devices and the estimated flux focusing factor effect due to the SQUID layouts [69]. As also expected from the test junction characteristics, there was no major systematic suppression of the V_{spp} by the fields well above the earth magnetic field. The symmetric notches at about 200μT are associated to the possible interference of the field dependence of the I_c of the 4μm wide dummy junction of the device. The incompleteness of these notches is associated to be due to a favorable possible slight non uniformity of the J_c of the 4μm wide junction. The favorable non-uniformties might also be made intentionally which is being further studied. The notches at the 40μT and 150μT in Figure 3.16 might be associated to the penetration of vortices close to the junctions [80] occurring at the larger magnetic fields during the cycling of the measurements.

Chapter 4

Impediments and Related Solutions Associated to Front-end Assembly of Scanning SQUID Microscope

4.1 Introduction

For the sensitive applications of rf SQUID based magnetic imaging systems, where high magnetic field sensitivity with high spatial resolution is required, two important issues to be considered are the front-end assembly of the SQUID microscope, and the SQUID signal level, V_{spp}. Another important consideration is, how to couple the sensor and sample, while the sensor is to work at liquid nitrogen temperature and sample is to be at room temperature. This is while both field sensitivity and spatial resolution are highly dependent on the distance between the sensor and the sample.

Bottlenecks allied to this kind of applications of the SQUID based systems requires to be highlighted and investigated for any such system designs. In the following chapter, we will probe into some of these limiting factors, which not only

provide insight to improve the sensitivity and field resolution, but also helps the development of new configurations for high resolution magnetic imaging systems.

4.2 System Oriented Hurdles

4.2.1 rf-coupling techniques

Both field sensitivity and spatial resolution are highly dependent on the distance between the sensor and the sample. Hence some approaches to couple the rf-SQUID sensor and samples have been investigated in this work as one of the first steps towards the development of a system for high-resolution magnetic field imaging.

With respect to the system design, use of high-T_c SQUIDs is superior compared to the low-T_c devices. Lift-off distance (LOD), the distance between the SQUID and the sample, plays a vital role for front-end assembly. LOD is inevitably widened for Helium based systems, where as in Nitrogen based systems, it can be decreased by using a thin window. Consequently, several tens of microns of short order lift-off distances can be achieved allowing high spatial resolution to be realized when using high-T_c SQUIDs. Designing such a system offers serious challenges especially when it is required to keep the sensor at cryogenic temperature and sample at room temperature. This by itself would be a hindrance to achieve close proximity, as we need a very precise separation adjustment system.

4.2.1.1 Lumped element LC tank circuit configuration

High field sensitivity of high T_c SQUIDs is associated with its large area layout where this inherited limitation hinders the high spatial resolution. Though washer area of the SQUID can be optimized for minimum area needed for efficient coupling to the LC tank circuit. The requirement of close coupling of the tank circuit introduces additional limits for the possible structural configuration for

front-end of rf-SQUID based microscope system configuration.

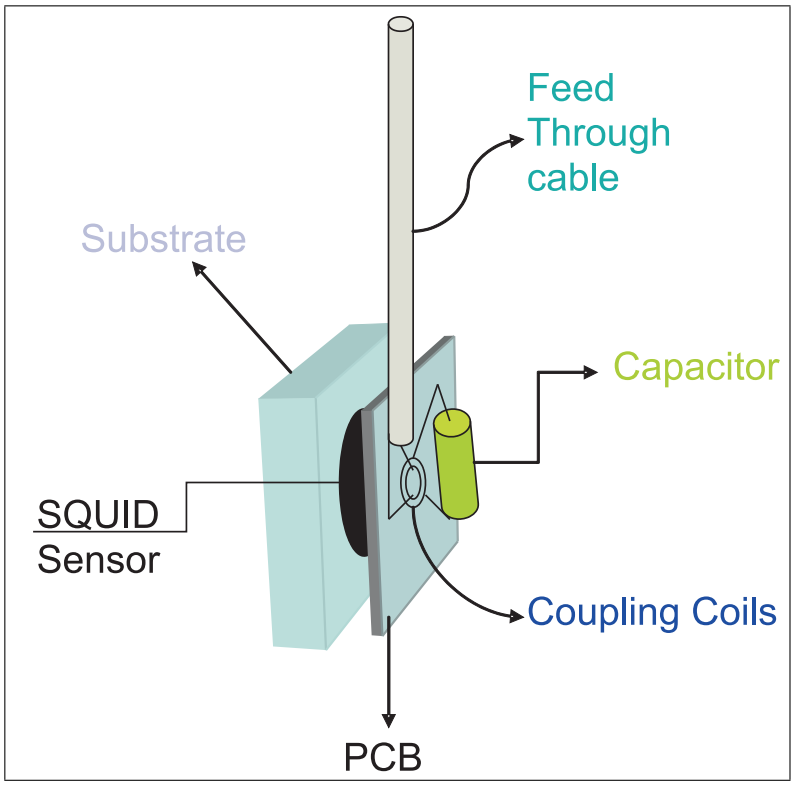

Figure 4.1: Direct coupling limitations due to size of the capacitor and coupling coil.

Direct coupling method and its limitation with respect to the size of the SQUID washer for the used typical magnetometer and gradiometer designs is shown in Figure 4.1. Their configuration with the lumped element tank circuit, which plays a role in the field sensitivity and puts a restriction on the minimum possible size of the front-end assembly, is also shown in Figure 4.1.

As a replacement for the conventional LC tank circuit, thin film superconducting coplanar resonators can also be used instead of the lumped elements tank circuit in flip chip configuration [61].

4.2.1.2 Coplanar resonator configuration

The need for the LC tank circuit introduces limits for the possible structural configuration for the head of rf-SQUID based microscope preventing simple design configurations to be further discussed here. This is while thin film superconducting coplanar resonators can also be used instead of the lumped element tank circuit in the flip chip configuration [61] as shown in Figure 4.2. Here we discuss the effect of coplanar resonator as biasing technique compared to conventional LC-tank circuit.

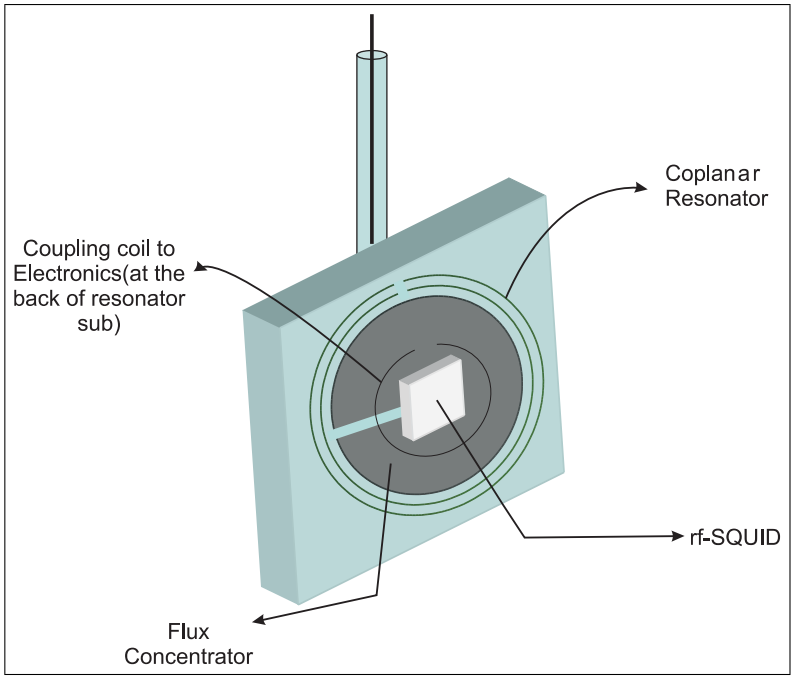

Figure 4.2: A flip chip configuration for rf-SQUID and circular coplanar resonator with integrated flux concentrator.

In the case of the coplanar resonator, we initially used either 8mm rectangular (SR8) or a 13.4mm circular (SR13) layout designs with integrated flux concentrators [61]. The difference in the performance of the SQUID using the above couplings was investigated. While the white noise level of the SQUIDs could be decreased by about four times when using the coplanar resonators, a relatively higher low frequency noise was observed in the noise spectra. This is while use of coplanar resonators with integrated flux concentrators introduces serious limitations in the spatial resolution. The designs without the flux concentrators were

used in the following. As in case of resonator, there are a couple of different possibilities in the way the SQUIDs can be coupled with a co-planar resonator as shown in Figure 4.3.

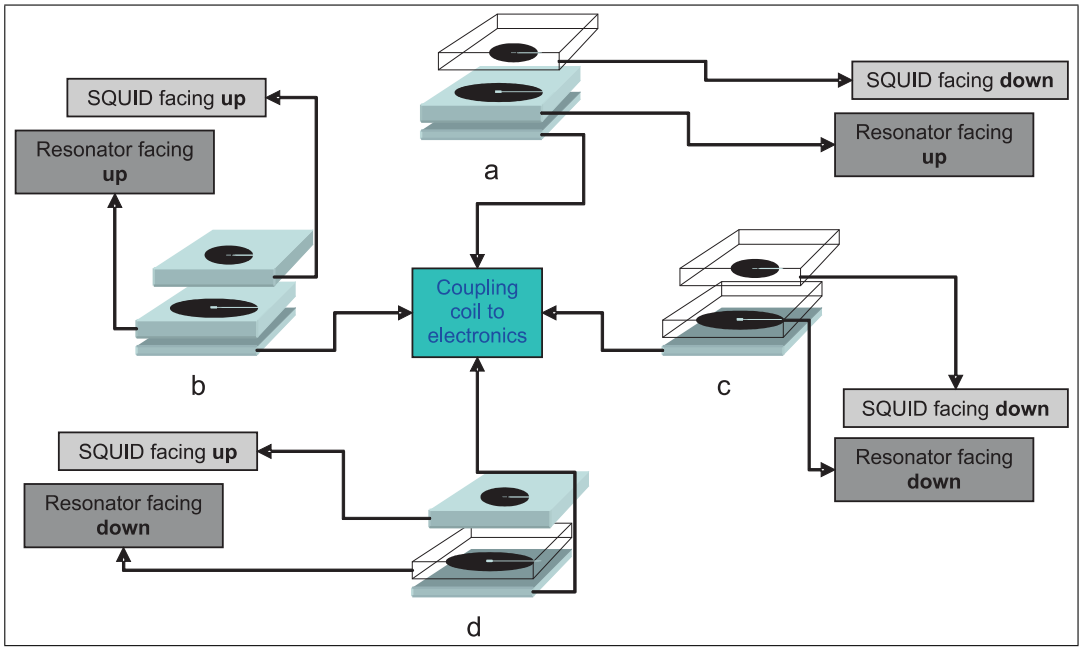

Figure 4.3: Possible coupling configurations between SQUID and the coplanar resonator.

Systematic study on coupling techniques for resonator, SQUID, and pick up coil of the electronics revealed that the best configuration is one in which there is a substrate between the resonator and the SQUID. The results obtained from other configuration are listed in Table 4.1.

Type	Description	Vspp level	Quality
a	S-R-Sub-C	900 mV	Lockable
b	S-Sub-R-sub-C	1.18 V	Lockable and noisy
c	S-Sub-R-C	400 mV	Lockable and clean
d	S-Sub-Sub-R-C	350 mV	Barely lockable and noisy

Table 4.1: Possible SQUID and the coplanar resonator coupling configurations with their relative signal and signal locking states. (S: SQUID, R: Resonator, sub: substrate, C: pick up coil electronics)

In type '*b*' configuration, where there is a substrate between the SQUID and the resonator and a substrate between the resonator and the pick up coil, it has

been observed that high SQUID signal level, and noise reduction can both be achieved. The improvement in the signal level from the worse case, d, is about 3.4 times, which is quite promising. The above results provide insight to two important facts: a) Distance between resonator and the coupling coil provides better signal coupling with electronics; b) Dielectric material between the SQUID and the resonator is beneficial to achieve high SQUID signal level.

The noise spectra of a SQUID made of high quality film grown on $LaAlO_3$ substrate with clean sharp CIBE steps is shown in Figure 4.8. Similar SQUIDs have been integrated in a second order 9-channel SQUID gradiometer system working over many thermal cycles and for about one year to date [97].

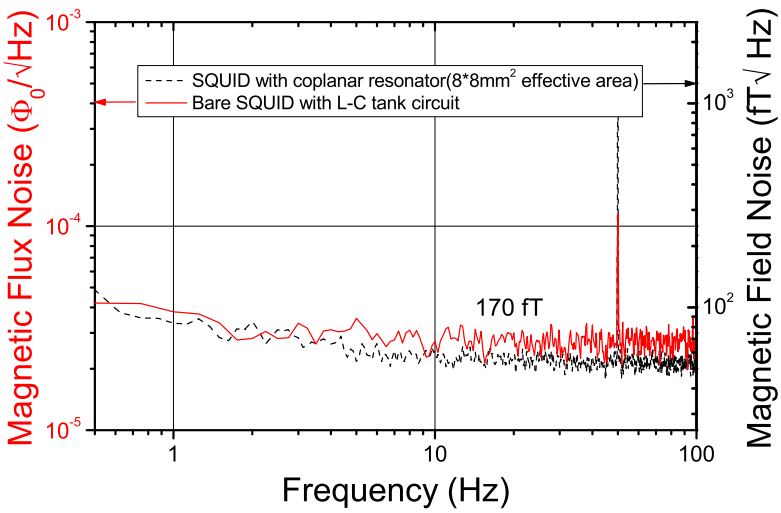

Figure 4.4: Noise spectra of low $1/f$ noise rf-SQUID magnetometer measured with conventional L-C tank circuit and superconducting coplanar resonator. The field sensitivity of the bare SQUID at white noise level is $170fT/\sqrt{Hz}$.

The noise spectra of the samples was measured with both conventional LC tank circuit and superconducting coplanar resonators [61]. While the white noise level of the SQUIDs could be decreased by about four times when using the coplanar resonators, a relatively higher $1/f$ type noise is revealed in the noise spectra, determining source of which is under further investigation [4].

A general comparison of the LC tank circuit with respect to resonator is shown

in Figure 4.5. Here we see that resonator as compared to tank circuit provides better signal level even under shielded environment and this will be discussed in this section.

This study provides insight for the possible flexibility for front-end assembly with respect to use of conventional tank circuit or Co-planar resonator. Further comparison between LC tank circuit and resonator with respect to other aspects is discussed in following section.

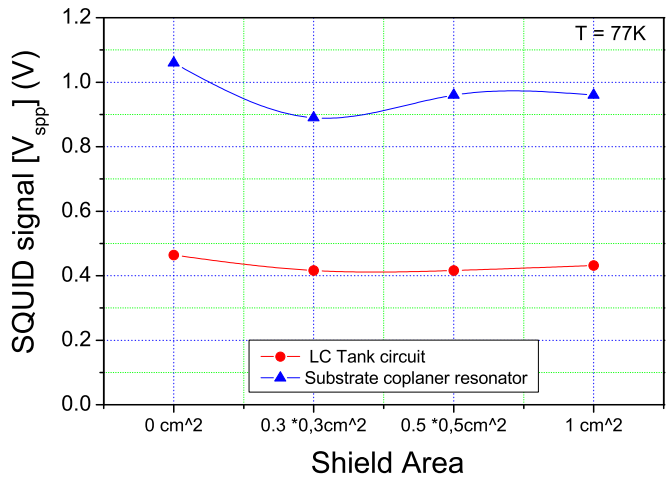

Figure 4.5: Effect of shielding on the maximum SQUID signal level under shielded condition with different rf coupling techniques.

4.2.2 Effect of LC tank circuit

Although it has been stated in detail that the substrate resonator has an advantage over tank circuit with respect to maximum achievable SQUID signal level its use for microscope application prospect is compromised, due to its limitation from parasitic pick up point of view. One requirement is to investigate how to improve the signal level by using the conventional tank circuit without affecting its size. The investigation on inductor loop diameter shows that by decreasing the loop diameter of the inductor, reducing the inductance or in other words increasing resonance frequency, the signal level is not only improved but also the

suppression due to shielding is reduced by a factor of 1.32 times under $1cm^2$ applied shield condition. This leads to the possibility that by optimization of the conventional tank circuit one can achieve better V_{spp} comparable with resonator while avoiding the effect due to the shielding and other problems associated with resonator.

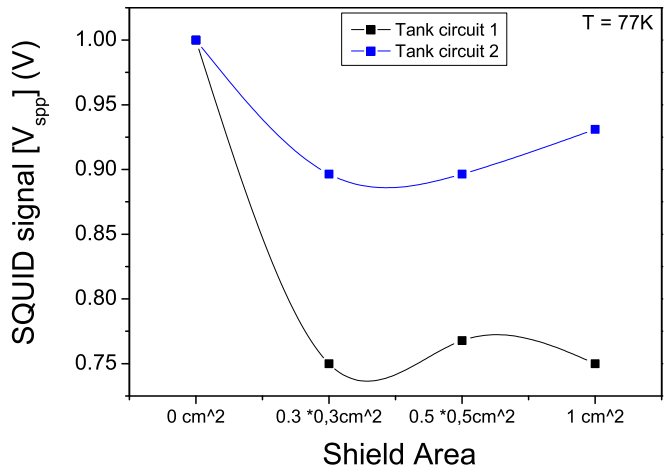

Figure 4.6: Effect of LC tank circuit on the SQUID signal level, where tank circuit 1 has small and tank circuit 2 has large loop diameters for the inductor.

4.2.3 Effect of the employed electronics

Figure 5.13 also attracts attention to the fact that use of the SQUID read out electronics plays a considerable role in signal suppression. Shifting the read out electronic circuits from working at high to low frequency range, with no shield applied, the signal gets suppressed by as much as 27% but the phase gets affected by an amount of 29%.

As shown in Figure 5.13, applying the shield causes a decrease in the signal level by 16.2% for high frequency range electronics and 22% for low frequency range electronics; thus it is better to use electronics working with a higher frequency range. This is while, shielding causes an increase of phase of the SQUID signal by 82% for high frequency electronics and 70% for the other case. So the

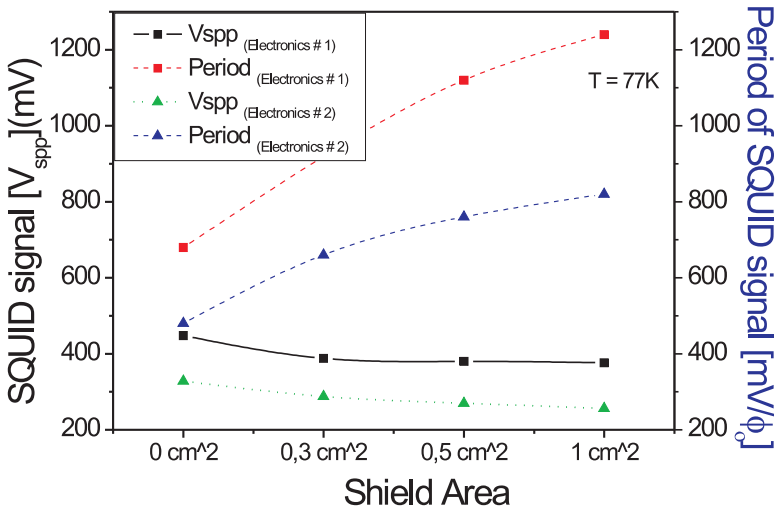

Figure 4.7: Effect of shield area on V_{spp} and period of SQUID signal vs. the employed electronics (electronics 1 = 1 GHz, electronics 2 = 400 to 700 MHz).

read out electronics must be appropriately selected taking into account both the frequency effects and the shielding effects.

4.2.4 Effect of high frequency electromagnetic interference

It has long been known that SQUIDs are very sensitive to high frequency electromagnetic interference (EMI). EMI can severly degrade the performance of SQUID systems which are operating in unshielded environment. Normal conducting shields, placed around each individual SQUID, substantially reduced EMI. But this is at the expense of an increased thermal magnetic noise [98], reduced bandwidth, and a frequency dependent phase shift due to eddy currents in the shield.

Recently, Ishikawa et al. [99] and Koch et al. [100] investigated the effects of EMI on dc SQUIDs, and Mück et al. [49], on rf SQUIDs. They found that EMI of sufficient intensity can reduce the modulation depth of SQUIDs as well as induce low frequency excess noise, especially if the EMI has an amplitude modulated part.

The physical dimensions of SQUIDs in most cases are small compared to the wavelength of the EMI. Radiation applied to the SQUID can thus be considered to be a pure rf flux bias [100], i.e., the SQUID senses only the magnetic component of the EM field. Indirect coupling can occur by pick up of EMI in the tank circuit and SQUID signal carrying leads. Besides, since the tank circuit is a resonant structure, substantial pick up of the electrical EMI component will take place only at frequencies at or close to its resonant frequency.

Depending on the shape of the transfer function, the SQUID response of the ac flux stays sinusoidal with increasing Φ_{EMI} for a sinusoidal transfer function, or becomes somewhat flat-topped for a triangular transfer function. With increasing Φ_{EMI}, a dc offset is superimposed on Φ_{ac} , which can be attributed to a rectifying of the EMI flux.

In summary, high frequency EM interference leads to a reduction of the SQUID modulation voltage if the EMI-flux is of the order of a flux quantum or larger. The only way to ameliorate this problem is by using a flux-locked loop with very high bandwidth (larger than ω_{rf}, which in most cases is impossible), or to prevent EMI flux from leaking into the SQUID by proper shielding [101].

4.3 Sensor Oriented Hurdles

4.3.1 Substrate selection (literature survey)

For a good epitaxial growth of HTc SC the choice of the substrate is quite crucial, as it must be compatible with the superconductor material both structurally and chemically. There is a wide range of substrates; most commonly used for YBCO growth are perovskites such as $LaAlO_3$, $SrTiO_3$ and $NdGaO_3$, but also ZrO_2, MgO, and Sapphire when buffered with thin films of CeO and MgO. The detailed properties of the substrates have been discussed in Appendix.

Excellent superconducting properties with a good epitaxial growth of the YBCO are result on such provskite substrates due to similarity of the crystal

Material	Lattice parameter (nm)
YBCO	a = 0.382, b = 0.389, c = 0.1169
$LaAlO_3$	0.379
$SrTiO_3$	0.391
$NdGaO_3$	0.386
MgO	0.421
Al_2O_3	a = b = 0.476, c = 0.13

Table 4.2: Lattice parameters for the YBCO and the related substrate compounds.

structures and the low lattice mismatch. When there is little lattice mismatch, then the crystal cut of the substrate affects the orientation of the films. As an example (100) or (001) oriented YBCO films can be achieved on (100) $SrTiO_3$ and $LaAlO_3$ substrate. According to a general understanding, it is assumed as a common rule that, low substrate temperature, high oxygen pressure, and high deposition rates during film deposition favor in-plane alignment of the YBCO c-axis. Some of the possible material choices for substrates are listed in Table 4.2.

All these substrates are informally standardized to the $10 \times 10mm^2$ and 0.5 or 1 mm thickness. In spite of very high dielectric losses in $SrTiO_3$, an excessive damping of Josephson oscillations and the resulting quantum interference has not been noticed. However, the high tangent delta of $SrTiO_3$ prevents its use in superconducting resonant tank circuits of rf SQUIDs, while the high dielectric constant leads to parasitic resonances, especially in multilayered flux transformers. The $LaAlO_3$ is suitable for rf tank circuits and reduce the parasitic resonances, especially in multilayered flux transformers. The $LaAlO_3$ is suitable for rf tank circuits and the parasitic resonances are less of a problem. But when cooling from the deposition temperature to below the transformation point of about 500^oC, the well known $LaAlO_3$ twinning causes uncontrollable displacements of patterned features, not acceptable in fine multilayered structures where lower and upper layers must remain well aligned. The effect of $LaAlO_3$ twinning on the $1/f$ noise in SQUID has not been investigated in details, but is suspected to be detrimental. An ideal substrate material for SQUID fabrication has not been found yet [102].

4.3.2 SQUID sensor selection

There is a trade off between achieving high field resolution and high spatial resolution due the fact that, for high spatial resolution, small dimension sensor configuration at the sensing tip is required. This is while for high field sensitivity a high pick up area is required. Two basic types discussed for rf-SQUID configurations in Section 2.4.4, magnetometer and gradiometer, can be optimized to achieve the best results. In our case, we have used both sensor configurations but have found gradiometer to be more suitable for microscope applications based on the fact that it provides low noise level due it its self noise cancellation property. The noise comparison for magnetometer and gradiometer is shown in Figure 4.8.

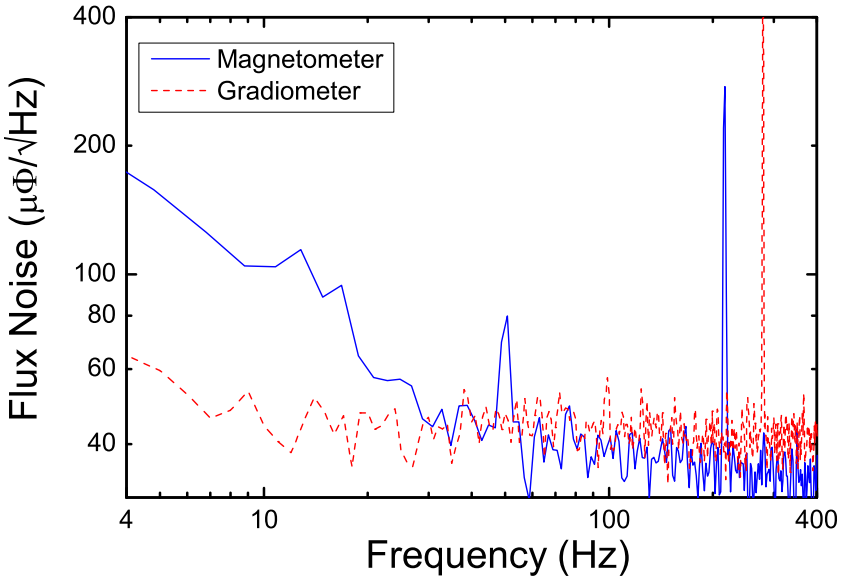

Figure 4.8: Noise spectra of bicrystal GB magnetometer and gradiometer designs on bicrystal $SrTiO_3$ substrate at their optimal operating temperatures.

Other possible advantages of using rf-SQUID gradiometer configuration on magnetometer is that it is much more easy to use it in integrated format with transformer assembly, which will be discussed at the end of this chapter. This provides us a chance to reduce the pick up area without reducing the signal level due to back side coupling of the SQUID with tank circuit.

4.3.3 Effect of substrate thickness

Another important aspect in the coupling coefficient between the SQUID and the LC tank circuit is substrate thickness dependence as the space in between. Theoretically SQUID signal should be improved by introducing dielectric materials in the gap which has been investigated by introducing the substrate material between the SQUID and LC tank circuit [31]. The basic principle is shown in Figure 4.9, where T_{sub} is the thickness of the substrate to be changed between SQUID and the rf coupling device.

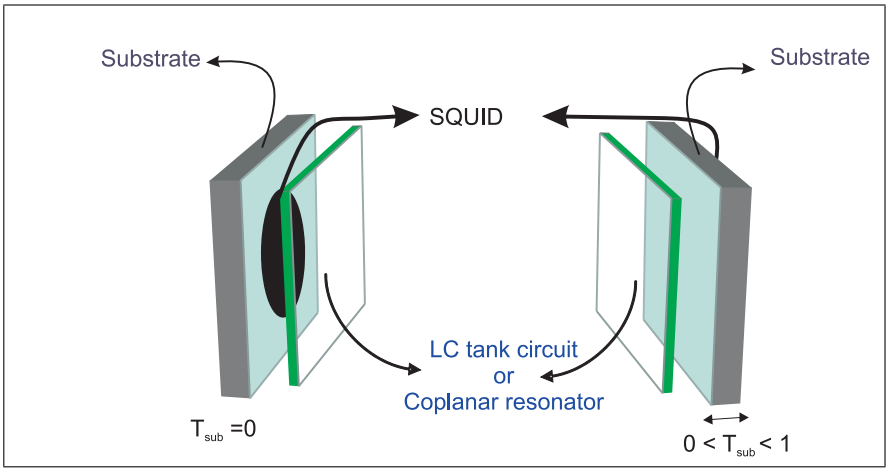

Figure 4.9: Conceptual picture for substrate thinning effect.

This investigation has been done on two types of the used substrate material, namely $LaAlO_3$ and $SrTiO_3$. This study on the optimum thickness of respective substrate material revealed that for $LaAlO_3$ it is about 0.4 mm as shown in Figure 4.10(a). The same investigation has been performed for the $SrTiO_3$ to compare with that of the $LaAlO_3$ material. The optimum thickness for the $SrTiO_3$ was found to be about 0.5 mm as shown in Figure 4.10(b).

Table 4.3 lists the effects of substrate thickness in terms of ratios compared to direct coupling, 4.10 (left), where the SQUID directly faces the tank circuit, and indirect coupling, 4.10 (right), where 1mm substrate is present between the SQUID and the tank circuit to the obtained signal from optimum thickness.

These observations imply that we need to have a system where we can thin

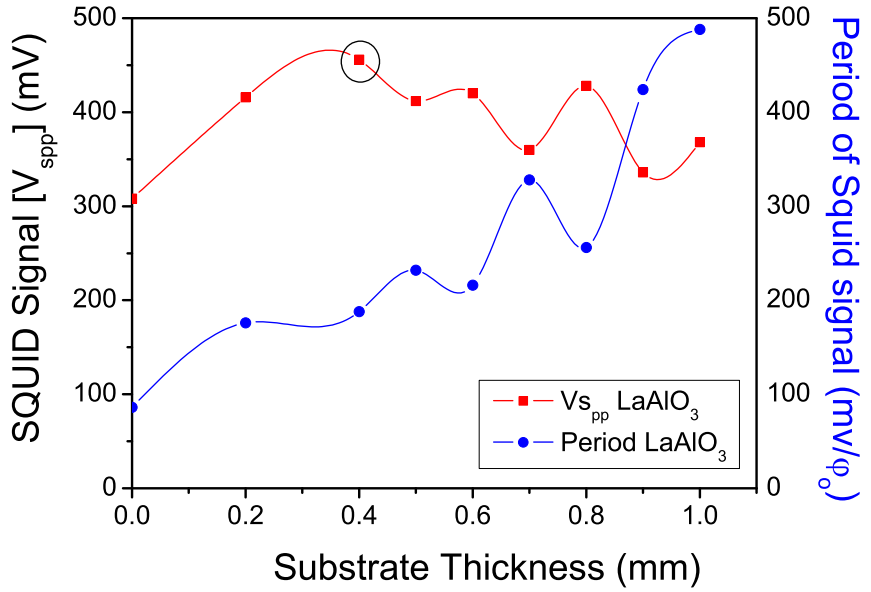

(a) $LaAlO_3$

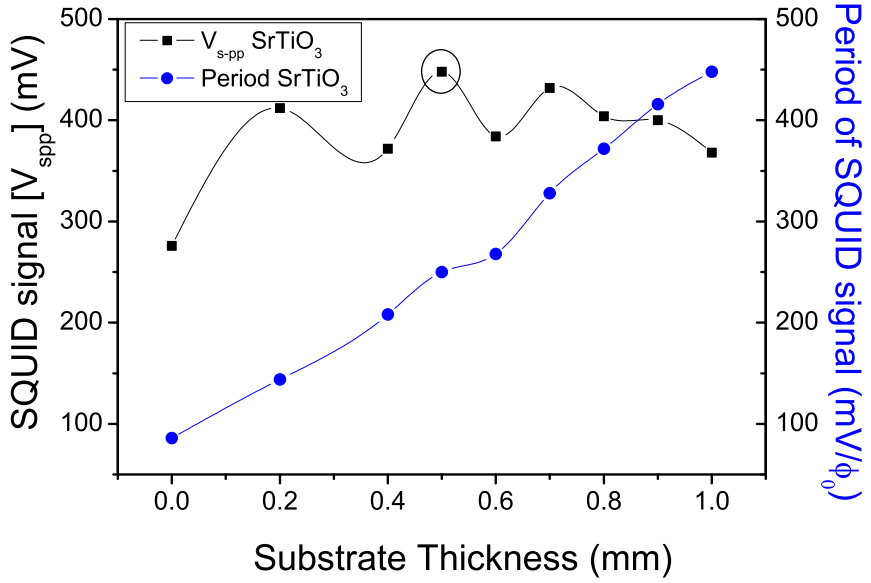

(b) $SrTiO_3$

Figure 4.10: Effect of substrate thickness between SQUID and LC tank circuit.

Coupling type	Sub. thickness	Compared to maximum achievable V_{spp}	
		$LaAlO_3$	$SrTiO_3$
Direct	0 mm	67.5 %	61.6 %
Optimum Thickness	0.4 mm	100 %	—
	0.5 mm	—	100 %
Indirect	1 mm	80.7 %	82.1 %

Table 4.3: Substrate thickness effect on the V_{spp}. Here the ratios have been taken by dividing the maximum signal level which is at optimum thickness level, to either 0mm (direct) or 1mm (indirect) coupling.

the substrate either prior to the SQUID fabrication or after, where both have been proven to be possible. Devices with various substrate thickness were made and characterized and presented in [6], [103].

4.3.4 Shielding effect

In most of the applications, it has been observed that noise coupling from the resonator circuit is very much influential, especially in the case when pick up transformers are being used to increase the spatial resolution. In such cases field sensing is not only due to the SQUID but also the resonator and the transformer legs serving as sensing devices, which add up to noise and cause reduction in the spatial resolution. For such a hurdle, the solution of shielding the unwanted area has been investigated in detail applying a superconducting film as a shield as shown in Figure 4.11.

In order to determine the shielding factor, the SQUID has been covered with $1cm^2$ YBCO thick film acting as shield. Magnitude of the ac magnetic field applied to the normal of the SQUID surface and shield under locked condition has been recorded and plotted in Figure 4.12.

Theoretical expectation for shielding factor of a $1cm^2$ shield applied to SQUID through a substrate of about 1 mm thickness is about 10, whereas experimentally obtained data shows a best results of 8.67 for small washer area SQUID. Shielding factor shows the SQUID's washer area inverse dependence leading to

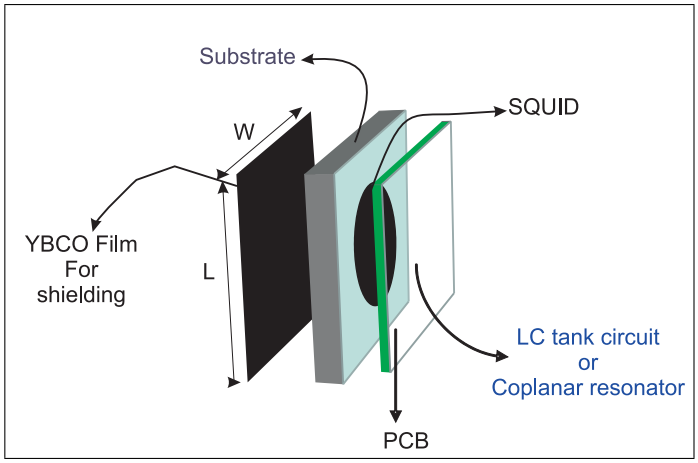

Figure 4.11: Schematic illustration of application of shield with width, W, and length, L; the thickness of the YBCO shielding film was 200 nm.

the conclusion that for the case when a transformer is used to pickup the signal, proper shielding of the SQUID can be achieved by having smaller washer area. As shown in Figure 4.12, the shielding is quite a linear function with respect to applied signal level. This gives us freedom to use shielding to shield the fields up to quite high levels without any nonlinearity caused by applying extra superconducting ground plane.

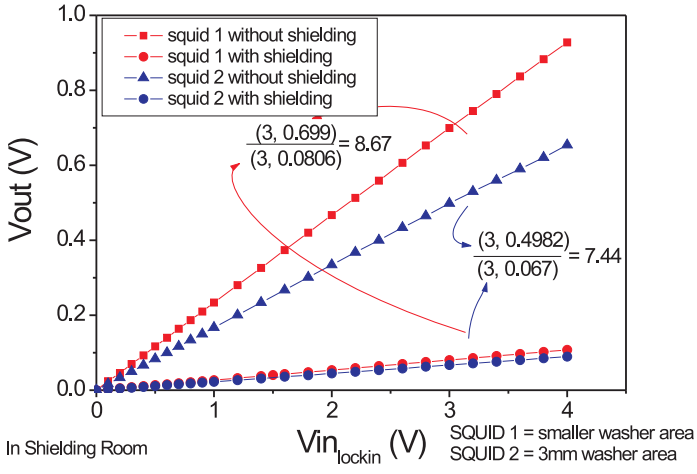

Figure 4.12: Determination of shielding factor.

The possibility of suppressing the SQUID signal by applying a shield has been investigated by covering the SQUID washer area with 200 nm YBCO film. It is

well known that for better shielding, a thicker film can provide better shielding as it can withstand higher shielding currents while being enhanced Meissner effect. The measured unlocked signal of the test SQUID is shown in Figure 4.13.

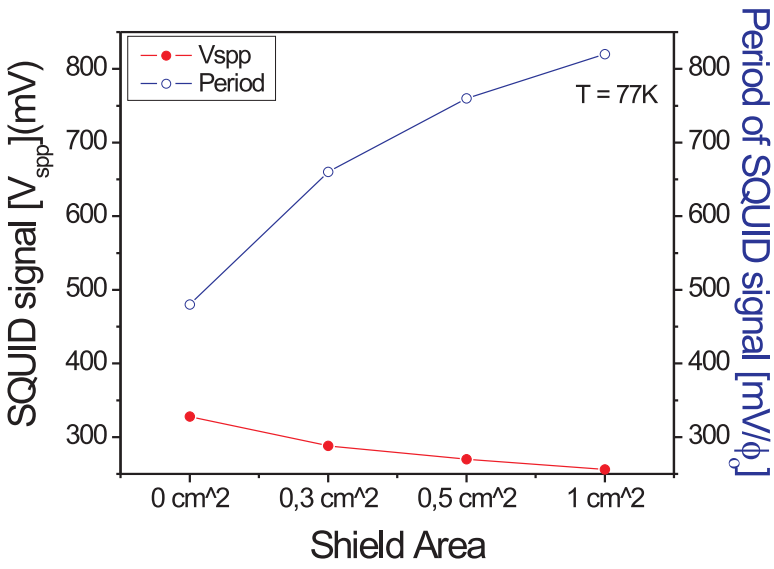

Figure 4.13: Effect of shield area on V_{spp} and period of the SQUID signal.

From the above graph it is clear that an increase of shield area from 0 to $1cm^2$ causes about 16.2% decrease in V_{spp}, but the phase of the SQUID signal is increased by 82%. Therefore, for the applications, where V_{spp} is being observed as a main entity, shielding does not affect the over all measurement much.

It has also been measured and observed that application of rf-coupling type not only affects the SQUID signal level but also causes suppression in signal by application of a shield. It is clear from Fig. 4.14 that resonator provides 2.28 times better signal level compared to that obtained by tank circuit. But on the other hand, shielding affects adversely the resonator coupling by decreasing the signal level by 10-20%, whereas in LC tank circuit it is just 7% depending on applied shield area. Hence from this aspect, it is better to use resonator for obtaining better SQUID characteristics, while for imaging purposes and the possible configurations it might not be the best choice.

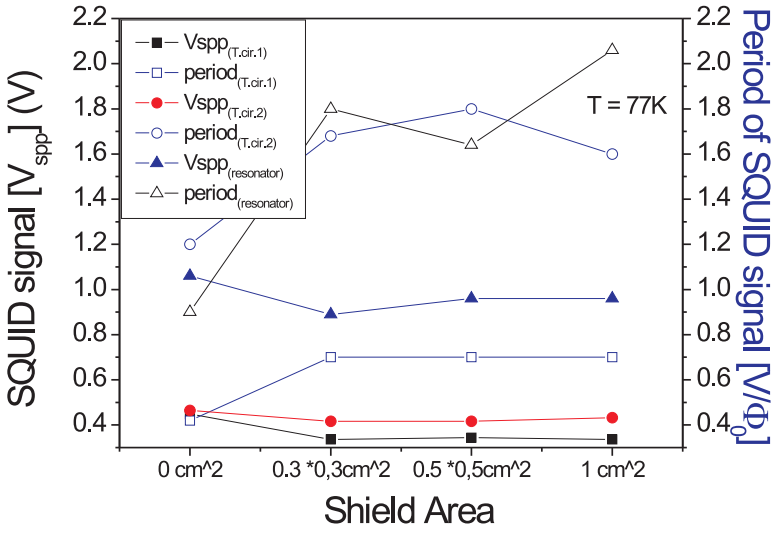

Figure 4.14: Effect of the tank circuit, while measuring the effect of shielding on the SQUID characteristics. a) Tank circuit 1 and 2 are conventional LC tank circuits but the loop diameter of inductor for tank circuit 1 is small compared to the tank circuit 2. b) Resonator circuit.

A resonator also has unwanted (parasitic) pick up because of not being shielded and can cause an additional background noise to the measurement, which is not suitable for high sensitive applications like Scanning SQUID microscope. So it would be preferable to use a small diameter conventional tank circuit optimized for high V_{spp} (comparable with resonator one) and avoid the effect due to shielding.

In order to investigate the reason for reduction in the signal of the SQUID, temperature sensitivity vs. shielding effect on V_{spp} has been investigated and shown in Figure 4.15. Theoretically, it can be stated that by applying a shield, inductance of SQUID changes and this inductance change of loop causes a change in the bias point. In such a situation, if increase of temperature reveals the SQUID signal back, it refers to the need of a SQUID with higher J_c. This way, inductance and current product would remain optimal under shielding for optimum temperature, which in our case is 77K. It is clear from Figure 4.15 that such an intersection point can be found, by increasing the temperature, where

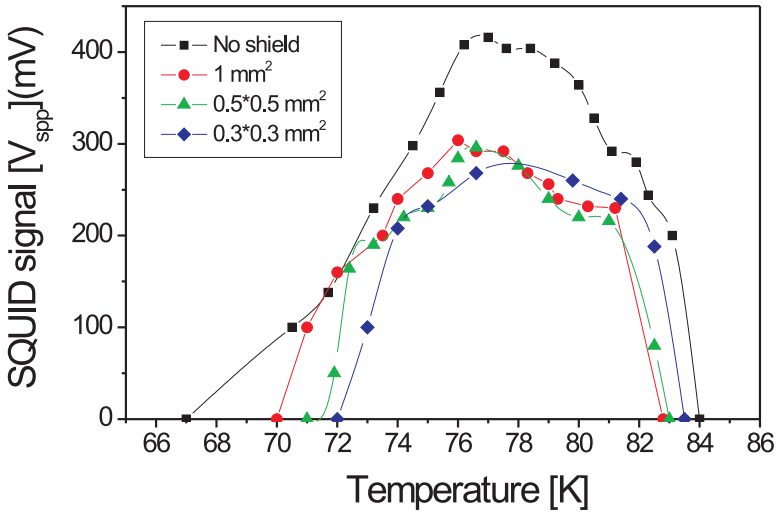

Figure 4.15: Effect of working temperature range on the shielding area.

signal with shield is equal to that of without shielding. This leads us to optimize the SQUID such that its J_c should be relatively high for optimum operation under shielding conditions.

4.3.5 Flux transformer

In the flux transfer configuration, the magnetic field of the samples is sensed with a superconducting pickup coil coupled to the rf-SQUID through the arms of the transformer. One simple configuration for the integration of the SQUID and the transformer with the tank circuit is shown in Figure 4.16. In such a configuration, there are few considerations, which should be taken into account as follows:

- How to couple the SQUID with the transformer loop most efficiently while there is an inevitable substrate material between the SQUID and the transformer.
- How to reduce the pick up from the arms of the transformer.

- What should be front-end structure in order to increase the spatial resolution of the microscope?

Some measurements have been performed in order to address the above problems as presented in the previous section and is further discussed in the following section. But before that, we consider some other possibilities, which can also be achieved with this kind of integration.

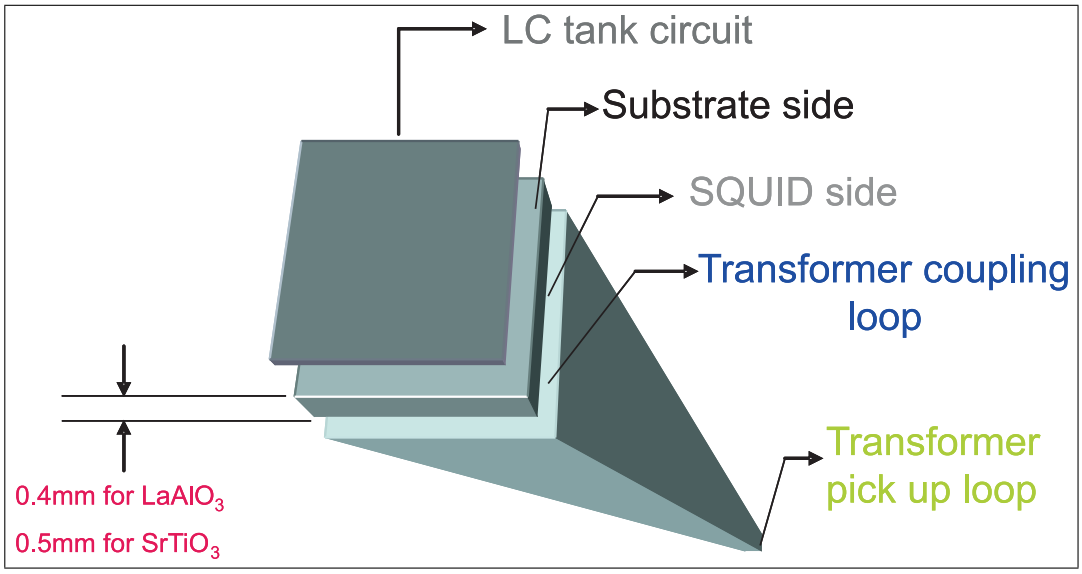

Figure 4.16: Conceptual figure for the new configuration for the sensing setup with SQUID coupled to the transformer face to face.

This study provides us the opportunity for a new configuration for the system shown in Figure 4.16. According to the new configuration, we can directly couple the SQUID washer to the transformer loop face to face, and couple the LC tank circuit from the back of the SQUID carrying substrate. Than the substrate can be thinned to 0.4 mm for $LaAlO_3$ substrate and 0.5 mm $SrTiO_3$ substrate. This will not only provide a good coupling between SQUID and LC tank circuit but also a better feeding from transformer loop to SQUID as the distance between them is minimized. The system is described in block diagram format in Figure 4.16.

This sort of configuration leads us towards the direction of multi layer structure, which will be discussed in the last chapter as future work. Another factor

related to geometry is to reduce the size of the front-end as we want to improve the spatial resolution which can be achieved by reaching as close as possible to sample with smallest diameter pickup loop as possible. This is with the consideration of the transformer efficiency based on the inductances of the pickup and coupling loops with respect to each other. Some designs for improving the efficiency as well as reducing the parasitic signal of the transformer structures are given in the conclusion and the future work.

Chapter 5

Scanning SQUID Microscope Design and Results

5.1 Introduction

The combination of the increasingly popular scanning probe microscopy techniques with the unparalleled sensitivity of a SQUID sensor to form a magnetic microscope is a straightforward approach. First experiments with low T_c SQUID and cold samples have been conducted in the 1970s and 1980s [104], [105]. Subsequently, scanning SQUID microscope using LTS magnetometers [106], [107] and HTS magnetometers [108] have been built. Such devices have been also applied to eddy current microscopy [109], imaging microwave fields [110], and radio-frequency fields [111]. The SQUID loop size and the SQUID-to-sample distance restricts these instruments to resolutions of the order of 10 μm. However, the use of an extremely soft magnetic electro chemically prepared sharp tip integrated into the SQUID loop [112], resulted in a resolution better than 100 nm. The SQUID was patterned with a pickup loop containing a centered bore, prepared by Excimer Laser with diameters down to 5 mm, for insertion of the flux guide. The sample could be moved under the tip by means of piezo actuators. With a scan range of 15 mm $\times$ 15 mm, sample scans were performed, imaging, e.g.,

the domain walls of an exchange coupled CoPt multi layer sample and magnetic colloid particles in a deposited ferro-fluid layer.

For many objects of interest, especially biological samples, systems operating with room temperature samples in ambient environment are required. In this case, the technical problem of distance minimization between the SQUID at cryogenic temperature and the warm sample is the key issue. Solutions using very thin insulating windows have been realized. The first such HTS microscope used a 25 μm thick sapphire window. A 15 μm SQUID-to-sample separation was achieved with a 3 μm silicon nitride window [113]. A thus far demonstrated application was the observation of magneto static bacteria [114], but multiple other uses can be imagined.

One can expect that many practical applications of SQUID microscopes will be developed in the near future. A straight-forward active application, at last in principle, is to test energized electrical circuits. Magnetic fields related to currents by the Biot Savart law can be inverted to find a unique two dimensional(2D) solution for the current distribution [115]. The recent most significant example is the use of a HTSC SQUID microscope for ac current mapping of connections and shorts in multi-chip modules (MCMs), and in flip-chip bump packages fabricated by semiconductor and computer industry. For this purpose, a HTS scanning SQUID microscope, with a Joule-Thompson APD Cryotrigger cryocooler, was unveiled in 1998 [116], [68]. This MAGMA microscope incorporates a dc SQUID mounted on the cold finger very close to a thin insulating window separating it from the measured object. the instrument has currently a lateral resolution of better than 50 μm (when SQUID-to-object distance $\leq$ 50 μm), and a B_N of $20pT/\sqrt{Hz}$ above 500 Hz.

5.2 Cryostat Assembly

Recent progress of SQUID technology, especially in the field of the high T_c SQUID, broadens the area of magnetic sensing applications. In considering the biomedical applications [117], [118], such as non-destructive evaluation [119], [120] and geophysical exploration T_c SQUID [121], it can be seen that the SQUID has clearly demonstrated its ability as a new evaluation technique in the semiconductor world. Mantz *et. al* first investigated antigen-antibody reactions in fluid samples with the SQUID using magnetic nano-particles.

This technique is anticipated because of the possibility of superiority of the SQUID against a conventional fluorescent method. Immunoassays are widely used in biology and medicine these days and the human health care industry can make progress with this technology. In the semiconductor field, Neocera Inc. developed the MAGNA-C1 prototype system, which can image current flow and make failure analysis in integrated circuits [122]. In these applications high magnetic field sensitivity with high spatial resolution is required as feature of the SQUID.

In the case of a low T_c SQUID, the lift-off distance, which corresponds to the distance between the SQUID and the sample, is inevitably widened because of Helium based cooling system. On the other hand, a high T_c SQUID has an advantage of higher cooling temperature and it can work even by using a thin window. Therefore, several tens of microns of short order lift-off distance can be achieved and high spatial resolution becomes realized. However, designs of these high T_c SQUID microscopes are very complex because of a precise separation adjustment system. In this chapter we will investigate few of new designs of high T_c SQUID microscope head and Dewar.

5.2.1 Mobile Glass-Fiber Cryostat based system

For providing a stable working temperature with low background vibrational noise, which is a part of conventional cryostat with mechanical pump system, a

cooling concept based on the orientation-independent cryostat ILK 2 (by institute für Luft- und Kältetechnik, Dresden) was evaluated. The mobile liquid nitrogen cryostat is depicted in Figure 5.10.

This Dewar also provides provision of using up to 4-channel system as shown in Figure 5.10(b). As the operating temperature of our superconducting sensors are 77K, therefore the pickup coil and the SQUID are housed in the vacuum space of a cryostat behind a thin sapphire window and are cooled through a thermal link to a liquid Nitrogen reservoir.

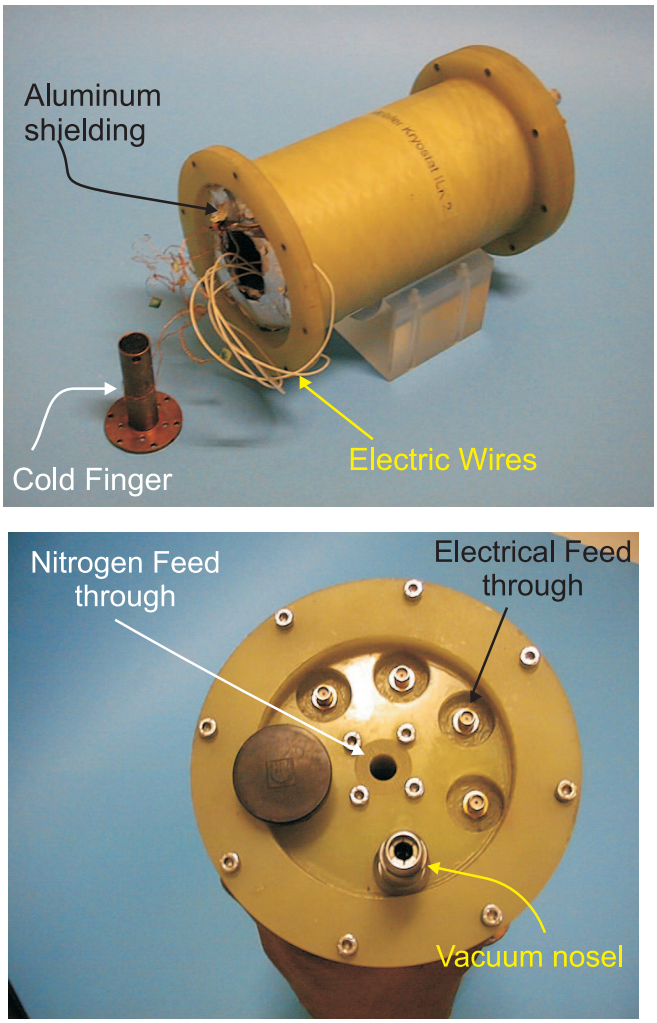

Figure 5.1: (a) Mobiler Kryostat ILK 2 with cold finger. (b) Top view of the Dewar.

A sapphire window has been used in order to keep the distance close enough to the sample and the pick up coil. The distance between the sapphire window and the pick up coil can be controlled with the help of Bellows [123]. To obtain optimal resolution, it is necessary to make the pickup loop of the SQUID very small, well shielded, and positioned as close as possible to the sample surface. A bellows mechanism is usually used to reduce the spacing between the 25 μm thick sapphire window and the superconducting pickup coil. The thermal insulation is provided by the vacuum. The sample is situated just below the sapphire window at room temperature.

For cold finger, sapphire based system has been proposed, as it is an insulator and has a high strength as well as a high thermal conductivity. The tip of the finger has been designed in such a way that proper coupling between SQUID sensor, LC-tank circuit, and the pick up coil can be achieved.

Mobiler Kryostat ILK 2 has not been pursued further for the following reasons: The cooling capacity, as shown in Figure 5.2(a), is not very high: values of 1.16 W/K in the upright orientation and 0.61 W/K in the upside down orientation were reported [33]; secondly, the hold time is only between 8 and 11 hours, as shown in Figure 5.2(b), depending on thermal load and on orientation. This will prevent keeping the SQUID microscope continuously cold since the hold time is not enough to maintain temperature from a working day's evening until the next morning.

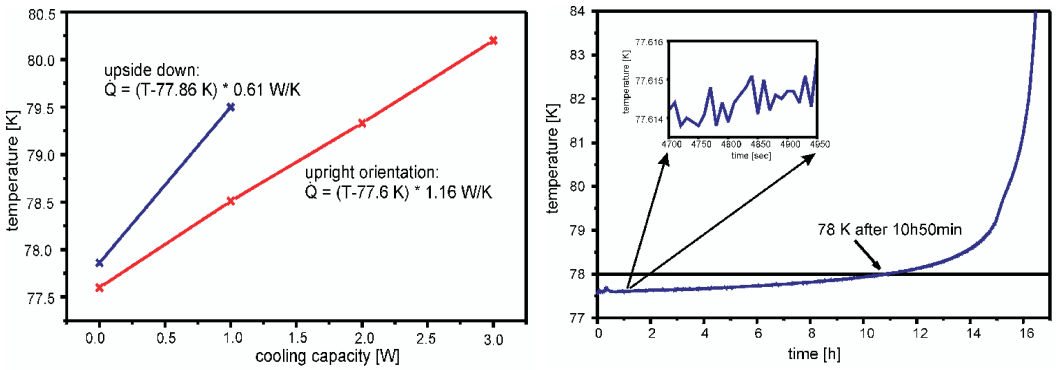

Figure 5.2: (Left:) Cooling capacity vs. temperature of Kryostat. (Right:) Hold time vs. temperature of Mobiler Kryostat ILK 2 dewar.

5.2.2 Stainless steel Cryostat based system I

The second prototype setup, which was realized for the SQUID microscope is based on a double wall cryostat manufactured from VA steel (see Figures 5.3 and 5.4). The internal container is filled with liquid nitrogen. The volume between the inner wall and outer wall is pumped down to 10 mbar by using a turbo molecular pump. At the bottom of the nitrogen bath, a casing filled with Zeolite material is incorporated.

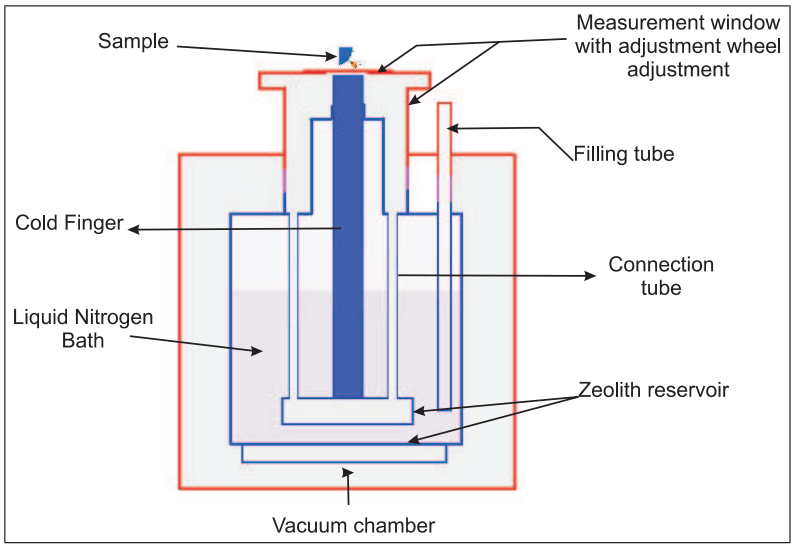

Figure 5.3: Schematic of the SQUID microscope with stainless steel cryostat.

It is used to make it possible to condense the air in vacuum chamber by getting cooled from the nitrogen in the inner bath. This condensation of oxygen and other gases helps to achieve the pressure down to 10^{-5} - 10^{-6}mbar. The inner liquid Nitrogen container is encapsulated with super isolation foil. The super isolation foil consists of thin polyethylene foil, which was vaporized on one side with aluminum. It prevents warming up the bath from radiant heat of the vacuum chamber. In Figure 5.4, the DN 100 flange, where the cold finger element is fastened, is located on the top of the vessel. An o-ring seals the cold finger with the cryostat, such that the nitrogen bath is gas tightly locked. The cold finger is manufactured using copper, since copper possesses very high heat conductivity. This is because with a circular cross sectional model with 10 mm diameter the minimum achievebale temperature under full bath condition was 84K, and with

almost empty bath, it was only about 118K, the cross section of the copper cold finger was enlarged by attaching half shells to it, which are bolted together. With this configuration working temperature range of 78K with full bath and 83K with almost empty bath has been achieved.

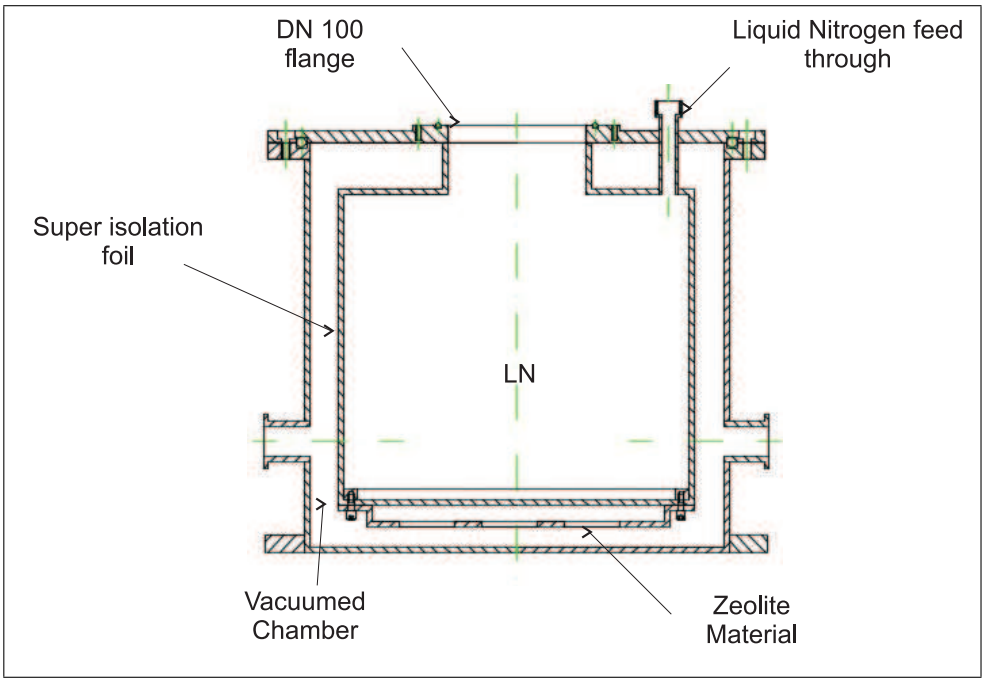

Figure 5.4: Sketch of the dewar [6].

At the bottom, with the lower assembly flange, cold finger element is connected with cryostat in gas tight configuration. This is because at low temperatures the water vapors would freeze. By means of the upper assembly flange, the measuring window is connected with the adjustment mechanics. The cold finger is also enclosed with super isolation foil, in order to resist against heating due to radiation. Two electrical connectors are connected to cold finger for readout of the SQUID signal and temperature measurement.

If one would mount the SQUID assembly directly on the copper finger, a magnetic field noise due to the statistical motion of charge carriers in the metal would be observed, the so called thermal noise. One must use a material with good thermal conductivity, where the conduction process is made not by means of electrons but by phonon. The best material for this purpose is diamond, whose thermal conduction amounts to a multiple of that of the copper but being

expensive and being difficult to work on, it was not used. A good alternative is Sapphire (alumina crystal ALO_3). The thermal conduction of Sapphire at ambient temperature amounts to only $\alpha = 40W/m.K$, approximately one tenth of the copper at 77K, but the production and treatment of sapphire are relatively economical. At T = 77K, its heat conductivity corresponds to that of the copper at this temperature. In Figure 5.5, the sapphire cold finger used in the microscope is depicted. By means of ultrasonic milling, a structure is machined into the material, in which the coupling coil and substrate resonator or the tank circuit are mounted. The bore is used to accommodate the thin cables for SQUID and Pt100 thermometer readout. The sapphire cord used in this SQUID microscope setup has a diameter of 14 mm at the top and of 20 nm at the bottom and is 50 mm long.

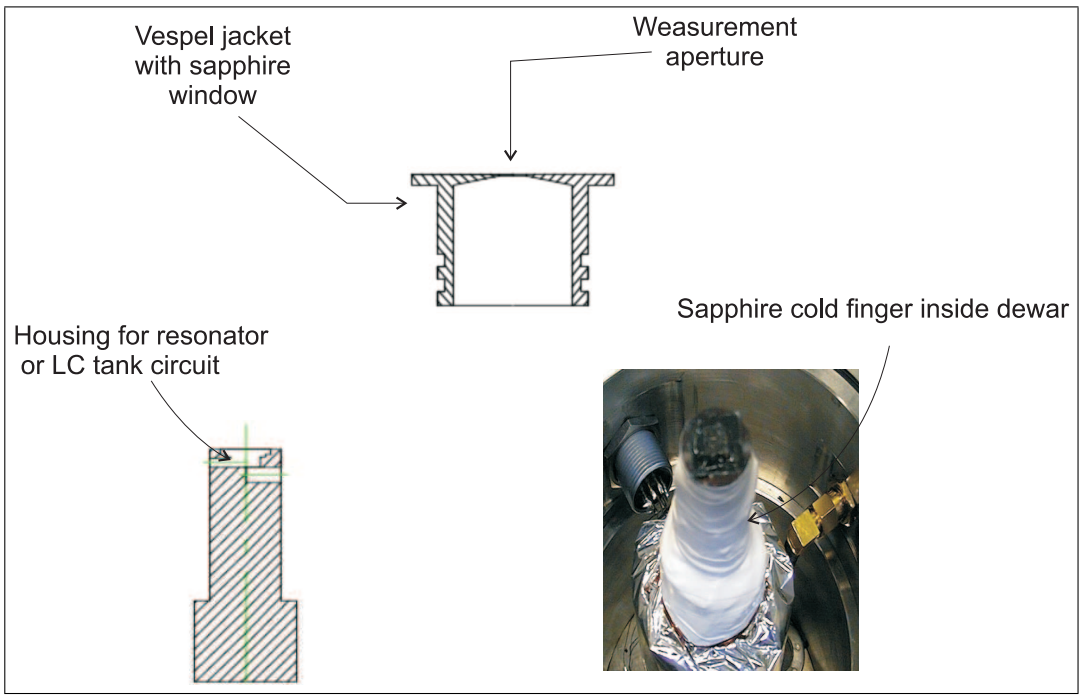

Figure 5.5: Sapphire cold finger with a diameter of 14mm. The upper hole serves as a fixture for the Pt-100 for temperature control. The coaxial measurement cable for the SQUID is guided through the inclined longitudinal hole with the opening at the side of the sapphire.

Figure 5.5 shows the Vespel jacket with the sapphire window sitting in the opening of the measurement window. The carrier jacket is manufactured from

Vespel, a special plastic material which is mechanically hard and may be subjected to large temperature variations. It is an electrical insulator, therefore thermal noise at the SQUID sensor is avoided. It is dimensionally stable up to temperatures of 350^oC and mechanically loadable down to temperatures of -200^oC without embitterment, as would most of plastic materials do at these temperatures. As a measurement opening, a bore hole of 8 mm diameter is applied in the center of the upper face. The measurement window is covered by sapphire slab (diameter 10 mm, thickness 50μm) which is affixed by means of two-component epoxy glue. The window is chosen such that to minimize the distance to the object.

As mentioned in the introduction, magnetic measurements are strongly dependent on the distance between sensor and magnetic sources, as described quantitatively by the dipole law.

$$B_z = \frac{\mu_0}{4\pi} \frac{2\pi R^2 I}{(z^2 + R^2)^{3/2}} \tag{5.1}$$

Where "z" is the distance between the center of the loop to point of observation and "R" is the radial distance [124].

In our measurement setup, the position of the magnetic field sensor, the SQUID, is constant [6]. In order to reduce the distance to the magnetic object to be measured, a mechanism was realized which allows approaching the magnetic object to the sensor as close as possible without impairing the isolation vacuum or the temperature of the sensor.

A Vespel jacket is inserted in the cold finger element by o-ring seals. This ensures vacuum tight vertical mobility of the jacket. With its upper face, the jacket rest on the plexiglass wheel. By rotating the plexiglass wheel, the distance between measurement opening and the SQUID underneath is altered. In order to obtain a scale, the plexiglass wheel is equipped with 130 holes around its circumference which serves as grid pattern. The pitch of the thread was chosen such that, the distance between SQUID and sample is altered by 3.85 μm for one notch of the grid pattern. Further detailed information about the system can be

found some where else [6], [125]. Here only necessary information are provided as for the basic design. This system is working at Forschungszentrum Jülich under the research group of ISG for further development of scanning SQUID microscope principles and improvement.

5.2.3 Prototype system II

In order to investigate the working principle of scanning SQUID microscope; a prototype system has been proposed and realized with a simple design configuration. The schematic diagram of the system is shown in Figure 5.6. In this configuration, the basic ease is that it can be modified easily for different configuration and is handy in use, while it also accomplishes the basic needs of having a SQUID sensor at liquid Nitrogen temperature and the sample at higher temperatures.

The system can be sub-divided into five main components and will be discussed in detail in the following. Before going into detail of each sub system we need to shed light on the environmental limitation in which this system has been made to work for high field sensitivity and spatial resolution.

- Un-shielded room from high EM waves generated from mobile and radio sub stations situated just on top of the building.
- Due to heavy electrical load on power lines, there are fluctuations in the ground levels up to few volts.
- Excessive use of mobile phone in the vicinity of the working environment, which generates quite high signals disturbing the SQUID signal.
- Active lab for Antenna and propagation research at the same floor.

These are few of the limiting factors which, as we will see later, affect the SQUID signal level either by suppressing, due to EMI waves, below such a level that it can not be locked [49] or, the high field suppresses the signal from the

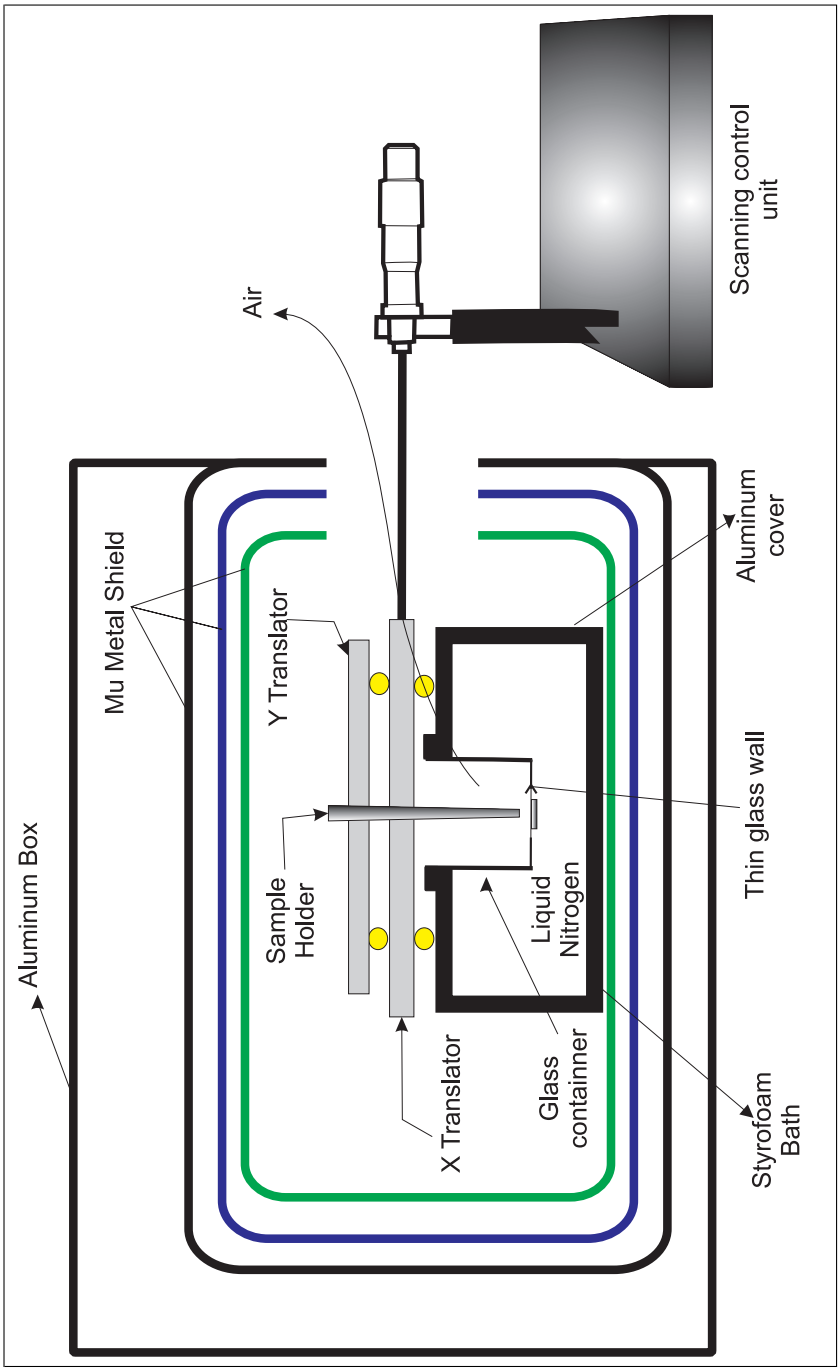

Figure 5.6: Schematic diagram of the hand made scanning SQUID microscope system.

sample itself. In the rest of the section we will investigate each sub system in detail.

5.2.3.1 Shielding

Magnetic fields exist everywhere and come in many different forms. As on one hand they are the main reason how most of our latest technological developments work, but on the other hand, there are certain cases, at lower frequencies, where these fields can interfere with the operation and accuracy of electronic components. One of which is, Superconducting Quantum Interference Devices (SQUIDs), which are very sensitive devices for magnetic sensing and is the main sensor of this study.

Common sources of low-frequency magnetic interference are permanent and includes superconducting magnets, power supplies, transformers, motors, transmission and distribution lines, and even the Earth's own magnetic field. Today, we are able to shield both AC and DC magnetic interference, either at the source or at the location of the sensitive component through the use of specially processed magnetic shielding materials. These shielding materials can entrap magnetic flux at the location of the source as effectively as they can shield fields away from a specific sensitive component. In deciding on the optimum shielding strategy and location of a shield, the determining factors are typically performance, complexity of design, and cost. According to the environmental condition stated above it is of quite importance to have proper shielding not only to low frequency magnetic fields but also to high frequency modulated electromagnetic fields for the system to work. In order to achieve this, the shielding has been done in three steps.

- **Low frequency shielding :** It is well known that rounded shields, such as cylinders or boxes with rounded corners, are better at redirecting lines of flux than square shape shields, as magnetic flux lines find it difficult to turn 90^o [126]. The size of the inner shield has been chosen according to well defined model (5.2), and by keeping the fact in mind that the smaller the effective radius of a shield, the better is its performance.

$$A = (\mu/4) * [(1 - Q1Q2Q3) + (\mu 2/16) * (N1N12N2N23N3) + (\mu/4) * (N1N3 + N1N2 - N1N2N3)(N12) + (N1N3 + N2N3 - N1N2N3)(N23) - (N1N12N2N23)] \quad (5.2)$$

A = attenuation, RI_x = Inside radius of the layers, RO_x = outside radius of layers, Q_x =$(RI_x^2)/(RO_x^2)$, Q_{xy} = $(RO_x^2)/(RI_y^2)$, N_x = 1-Q_x and N_{xy} = 1-Q_{xy} [127].

There are many available options for shielding as shown in Table 5.1 with their characteristics.

	Mumetal	Amunickel	ULCS
Density	0.316	0.294	0.283
Thermal Expansion	7.0 x 10^6	4.6 x 10^6	7.6 x 10^6
Thermal conductivity	136	90	-
Electrical resistivity	349	290	-
Curle Temperature	545	932	-

Table 5.1: Basic shielding materials and their general properties

In our setup we have used a μ-metal three layer shields in cylindrical format and is shown in Figure 5.7.

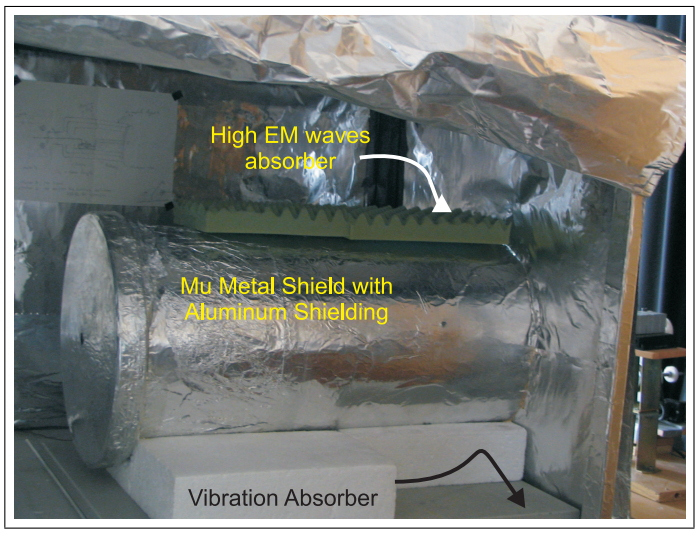

Figure 5.7: Three-layer μ-metal shield with circular shape, used to shield against low frequency magnetic filed.

Most magnetic shields made today are constructed from high permeability materials such as a μ-metal, an 80% nickel-iron alloy specially designed for magnetic shielding applications [127].

- **High frequency shielding:** High frequency EM waves suppresses the SQUID signal level. The effect is more severe when there is low frequency modulated EM waves as it is in our case. Hence it is very essential to encapsulate the whole system in proper shielding [49]. In this case aluminium Faraday cage kind of configuration has been used to shield the sensor and a μ-metal shield area as shown in Figure 5.8. For this purpose 0.5 mm thick aluminium sheet has been used with proper grounding not only with rest of the electronics components but also with water pipe lines which to our knowledge is a more stable grounding compared to the normal electrical ground.

Figure 5.8: Faraday cage made with aluminium sheet of thickness of about 0.5 mm to shield against high frequency EM waves.

- **Wire shielding:** Wires carrying the SQUID signal has been shielded with the same 0.5 mm thick aluminium sheet to protect them from unwanted pickup from the environment. Here it is worth to mention about the strange realization that the SQUID electronics coupling cable has to touch the μ-metal directly, otherwise there is no SQUID signal. An interesting observation is this that if we try to make contact between the cable and a μ-metal by any other means, for example, by using wire or thinner Al sheet, it does not resolve the problem.

5.2.3.2 Scanning stage

In order to scan the sample, one needs to have a very stable scanning stage. So for this case a scanning stage has been fabricated, which consists of two parts discussed as follows;

- **Motor end:** The conventional stepper motor based scanning stage can not be used for the reason of high magnetic field pulses generated inside the motor, which can not be shielded easily and can be sensed even inside three layers of a μ-metal shield. So to avoid the noise due to operation of step motor, a dc motor with appropriate gear system has been used, as shown in Figure 5.9(a). The speed of dc motor was controlled by a fixed voltage supplied by computer and can be reversed or increased according to the demand. During the measurements, a fixed scanning speed of 25 μm/sec has been used.

  A lever for manual motion control has also been embedded in order to do fine tuning when it is required to bias the sample at a fixed position. Here it is necessary to mention that due to non linearity of the dc motor reverse and forward scanning speeds were not the same under same applied voltage magnitude. Hence this correction factor had to be either adjusted through the computer program, or the data needed to be corrected by signal processing.

- **Sample end:** In order to couple the scanning unit outside the Faraday

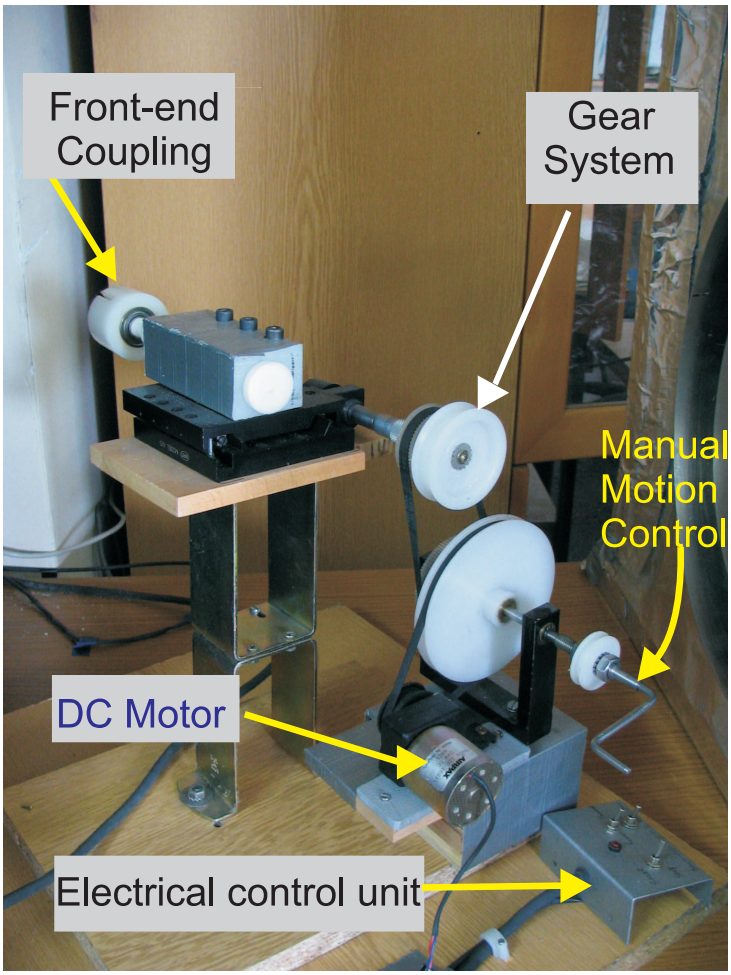

(a) Motor control unit for x-axis motion control with gear system to reduce the speed to 25μm/second.

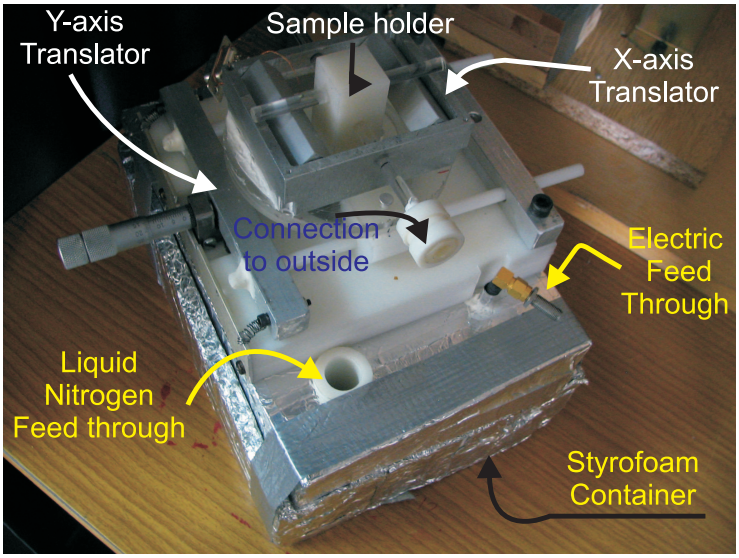

(b) Translation stage with x and y-axis translation units and coupling mechanism for liver to motor unit.

Figure 5.9: Scanning Stage configuration for microscope design.

cage, a glass rod has been used due to the facts that firstly it is non magnetic and secondly because of its low friction. This rod has been coupled to front-end scanning unit, which is shown in Figure 5.9(b).

Sample motion with this setup configuration provides us the freedom of 2 Dimensional motion. The only x-axis motion has been controlled by computer, where as y-axis has manual control with micrometer screw. Y axis control has been left as manual due to space limitation inside the a μ-metal shield and secondly for the initial measurement where one dimensional scanning was enough.

5.2.3.3 Liquid Nitrogen Bath

In order to increase the flexibility of the prototype dewar design, a simple stytrofoam based system has been designed, as shown in Figure 5.10.

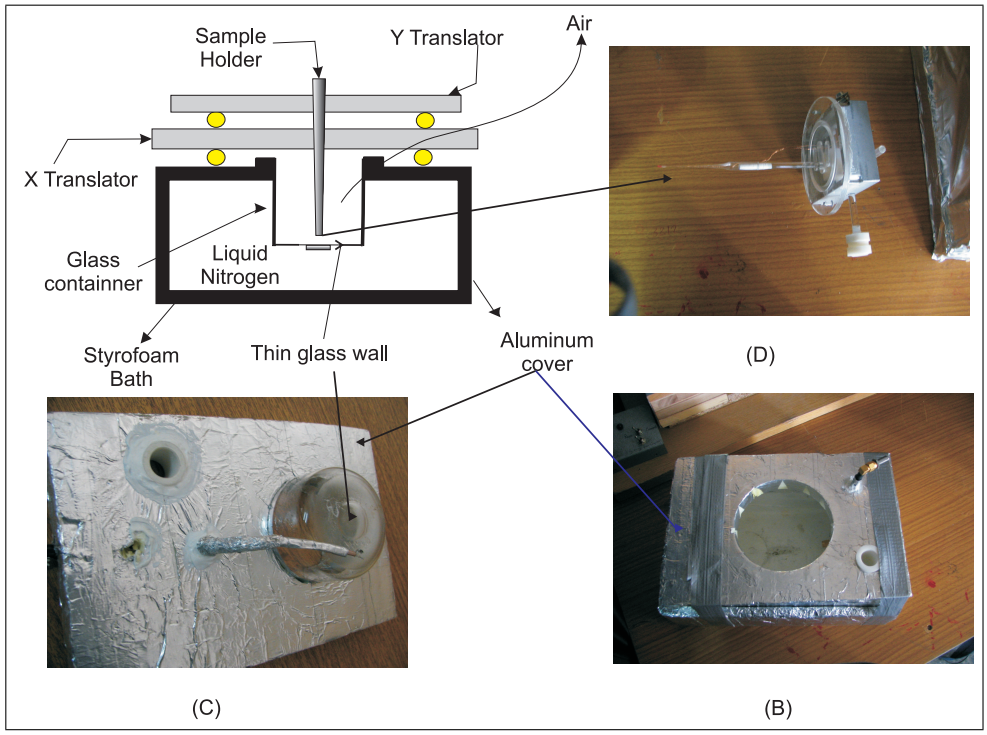

Figure 5.10: Styrofoam Dewar design and sample holder configuration for prototype system. (a) schematic diagram of the dewar (b) dewar with its accessories (c) glass configuration and (d) sample holder.

In order to protect from the high EM fields, the Styrofoam Dewar it has been properly wrapped in thin copper foil. Although the hold time of Nitrogen is not that much in this kind of simple design, it is easy to refill the bath without changing the configuration or disturbing the measurement. Styrofoam bath has been divided into two parts by using a glass container with extra thin bottom in the range of few 100s of micron. SQUID sensor is attached at the thin bottom of the glass and the sample to be scanned is scanned inside the glass. This makes the sample to sensor thickness as equal to the thickness of the bottom of the glass while the sample is outside the liquid Nitrogen as shown in Figure 5.10.

5.2.3.4 Computer control

In order to increase the reliability in the data acquisition, LabView software has been used for both data and monitoring the scanning stage. A graphic user interface window is shown in Figure 5.11.

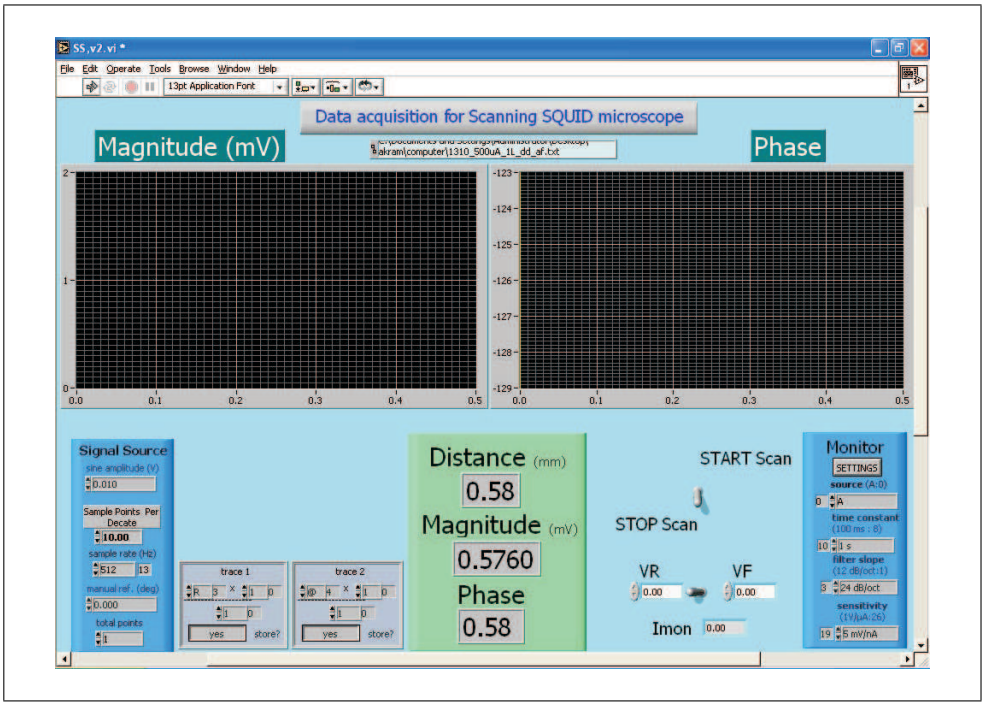

Figure 5.11: Front pannel of the LabView program developed to take the data and control the scanning stage.

- **Data Acquisition:** In our study, either straight wire or dipole has been used to simulate the magnetic particles as sample, which will be discussed later in this chapter in detail. In both of these configurations, the sample was fed with 1kHz frequency and the output of the SQUID Electronics in locked state is fed to lock-in amplifier to sense the 1kHz component. At each step of motion of the sample, the magnitude and phase has been recorded. The characterization setup will be discussed later.

- **Scanning stage control:** As stated before in our system, only x-axis motion has been controlled by use of computer. In this case, fixed voltage has been applied to motor and the data has been recorded with fixed time period. Due to nonlinearity of motor, speed depends on the direction of scan and hence, the possibility of different loop gains has been added in the program.

5.2.3.5 Characterization setup

In order to sense the signal due to the motion of dipoles, dipoles have been fed with low frequency current. This low frequency modulation has been sensed in the locked signal of the SQUID at the output of rf-electronics with the use of Lock-in amplifier. The block diagram representing the setup is shown in Figure 5.12.

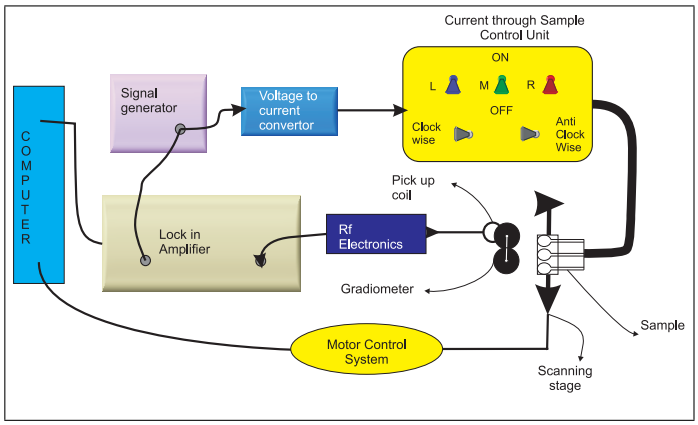

Figure 5.12: Block diagram representing the setup for sensing the dipole motion by computer controled system.

5.3 Scanning Results

5.3.1 Wire scanning

5.3.1.1 Results from System 1(Stainless steel Cryostat based system) [6]

In order to test the basic principle of the scanning, as a first step, a wire carrying ac current has been used as a sample to be scanned. This measurement also helps to find the distance between the sensor and the sample. The principal setup is shown in Figure 5.13.

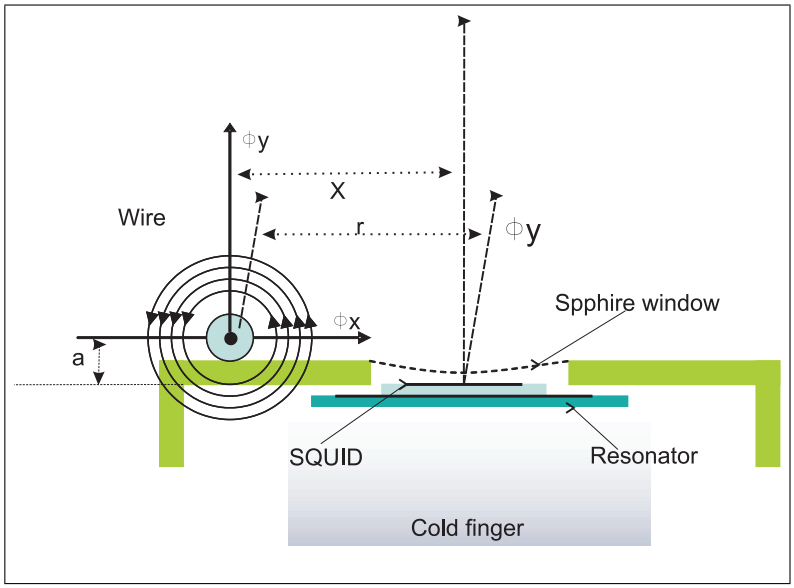

Figure 5.13: Principal setup for detection of magnetic field from a moving wire with an ac current modulation.

The wire has been stretched between two plastic supports and the motion has been facilitated by using the handle of a micrometer screw. When the handle of the micrometer screw is rotated with the help of a stepper motor through a rubber band, the wire would move back and forth. Here we tried to use non magnetic material during the measurement in order to reduce the effect of the interferences. It may ensure that the wire is continuously touching the glass at the bottom while sliding across.

The SQUID magnetometer only measures the magnetic flux threading its loop, thus only the field component perpendicular to its effective area is relevant. At a distance $x \ll -a$ in horizontal direction, the magnetic field recorded by the sensor is at its minimum. While the wire is approaching the SQUID, the field in the SQUID rises until it reaches a maximum, when the field of the wire runs through the SQUID center at 45^o to its normal. When the wire is located exactly above the SQUID, the sensor does not see any field because of the symmetry. Upon moving away, the field falls to minimum value, until the field decays more and more, while the wire moves further and further away ($x \gg a$).

A thin copper wire is moved across the sapphire window by means of a micrometer screw. The micrometer screw handle is driven by a computer controlled dc motor by means of a step down gear system. By this means, a constant velocity of 645 μm was obtained. The wire was fed with a 1kHz ac current signal, where this signal appears as a modulated signal on top of the locked signal of SQUID. This was acquired by means of a lock-in amplifier. Figure 5.14 shows the result of a measurement.

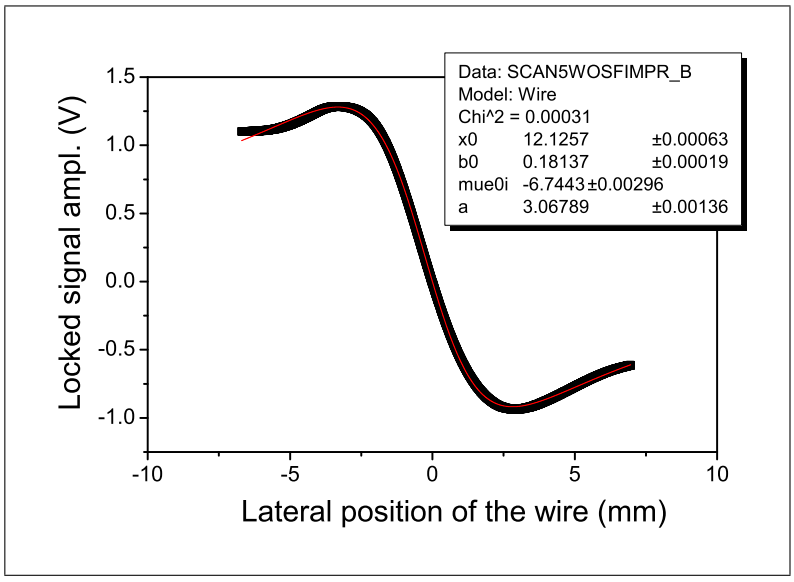

Figure 5.14: Results of magnetic distance measurement and fitting data with approximate model.

The positive and negative maximums are clearly visible in the figure. At the zero crossing, the wire is located exactly above the SQUID. Due to the limited

adjustment range of the micrometer screw, the limits $x \ll -a$ and $x \gg a$ could be realized experimentally. The distance between the two extremes in Figure 5.14 is a direct measure of the distance between the SQUID and the source.

The magnitude of the magnetic field B_L of a straight wire at a distance r is given by:

$$B_L = \frac{\mu_0}{2\pi}\frac{I_L}{r} \tag{5.3}$$

In our case with a SQUID sensor, a field of a few nT is more than sufficient. For sufficiently small frequencies, the current through the wire is given by:

$$I_L = \frac{U_{Lock-In}}{R_i + R_L + R_V} \tag{5.4}$$

With source resistance R_i, shunt resistance R_V and wire resistance R_L, by inserting value of I_L into B_L and solving for $U_{lock-in}$, one obtains the following function:

$$U_{Lock-in} = \frac{2\pi r(R_i + R_L + R_V)}{\mu_0} \tag{5.5}$$

Here, the shunt resistance R_V is chosen such that the voltage $U_{lock-in}$ can be varied conveniently between 1 V and 10V.

The distance between SQUID and source is derived from the recorded magnetic field transient during scan of a wire. B_L reads in vectorial notation as $r^2 = a^2 + x^2$.

$$B = \frac{\mu_0}{2\pi}\frac{I_L}{\sqrt{a^2 + x^2}}e_r \tag{5.6}$$

With the unity vector in r direction,

$$e_r = \begin{pmatrix} \frac{a}{r} \\ \frac{x}{r} \end{pmatrix} = \begin{pmatrix} \frac{a}{\sqrt{a^2+x^2}} \\ \frac{x}{\sqrt{a^2+x^2}} \end{pmatrix} \tag{5.7}$$

One obtains

$$B_y = \frac{\mu_0}{2\pi} \frac{I_L}{a^2+x^2} \begin{pmatrix} .a \\ x \end{pmatrix} \tag{5.8}$$

For $x \gg a$, one can neglect "a" , and the value of the vertical magnetic field component reduces to

$$B_y = \frac{\mu_0 I_L}{2\pi} \frac{x}{a^2+x^2}. \tag{5.9}$$

In order to obtain the distance between the two extrema, the above equation is differentiated and equaled to zero, resulting in;

$$B'_y = \frac{dB}{dx} = 0 = \frac{\mu_0 I_L}{2\pi} \left(a^2 - x^2\right). \tag{5.10}$$

The two solutions are: $x = \pm a$. Thus, the distance "a" between the SQUID and the wire source is simply half the distance between the two extrema recorded during a scan of the wire past the SQUID sensor.The above model has been used to find out the approximate value of "a" as shown in Figure 5.14.

5.3.1.2 Effect of distance

In order to measure the effect of the distance of the sample from the SQUID sensor, a wire with a fixed signal level has been scanned with different heights. For this, an accurate height and a measured height, with the help of a software model fitting, has been compared and the results are shown in Figure 5.15.

This kind of measurement can be used to find out the depth of fatigue in the system. This gives us an excellent reference to find out the position and depth

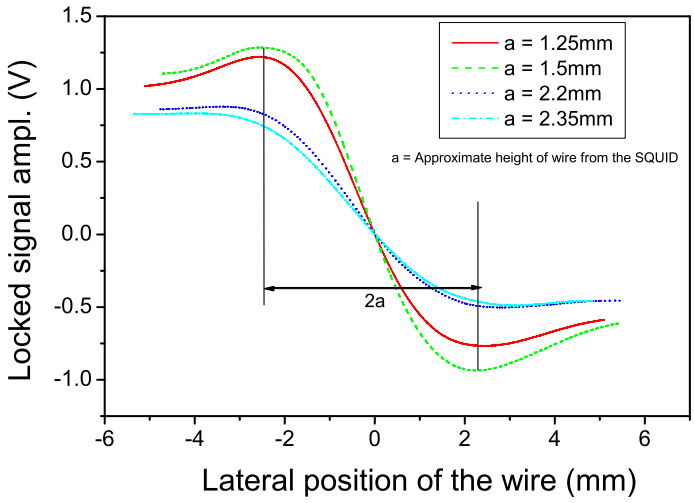

Figure 5.15: Results of magnetic distance measurement and fitting data with approximate model.

of the current carrying wire, or in other words, a live component buried under multi layers.

5.3.1.3 Effect of Applied field

In Scanning SQUID microscopy, one of the important measurements is to improve the field sensitivity of the setup. In order to measure the sensitivity of the system 1, effect of the signal level has been measured. Here, by fixing the height of the sample from SQUID, signal power has been reduced and the scan was repeated. The results are shown in Figure 5.16.

With such a simple setup, signal down to few nT was measured. The systematic decrease in the amplitude of the curve shows the linearity of the system and shows that system field resolution can be increased if we decrease the spacing between the sample and SQUID. This prediction lead to the fact that by decreasing "a" to few micrometers, we can sense the field in the range of fT, which is the ultimate aim of such a magnetic imaging system.

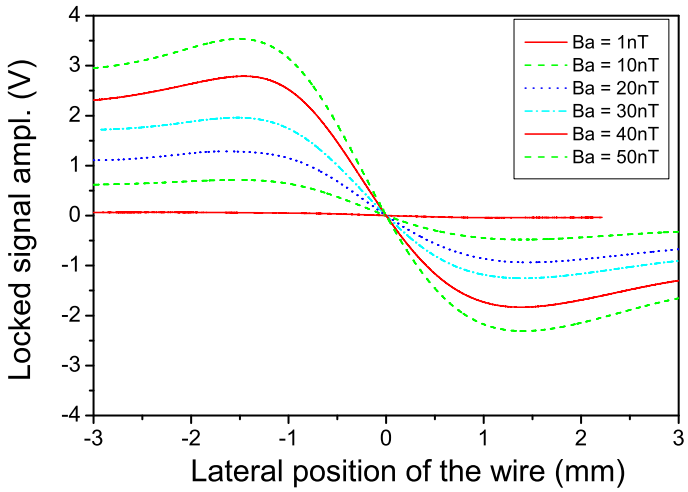

Figure 5.16: Ultimate field resolution for the system, which is quite linear predicting that the resolution can be increased further, if we decrease the distance between the sample and the SQUID.

Here another parameter which plays a role is the direct pick up from the substrate resonator. So in order to reduce the effect of this pick up, superconducting shielding concept discussed in the previous section has been implemented. In such a case, in order to sense the signal and in order to improve the spatial resolution of the system, the concept of transformer has been used. The results obtained by applying shield and flux transformer are discussed in the following subsection.

5.3.1.4 Effect of Applied transformer

Transformer coupling configuration is shown in Figure 5.17. Here we couple the back of the SQUID to front the face of the resonator and then couple the SQUID washer with transformer in face to face coupling. The whole configuration is shielded by using a superconducting film of YBCO.

Wire scan under such a condition is shown in Figure 5.18. One needs to compare the results without transformer condition under the same height configurations. These results are not much clear according to our expectations.

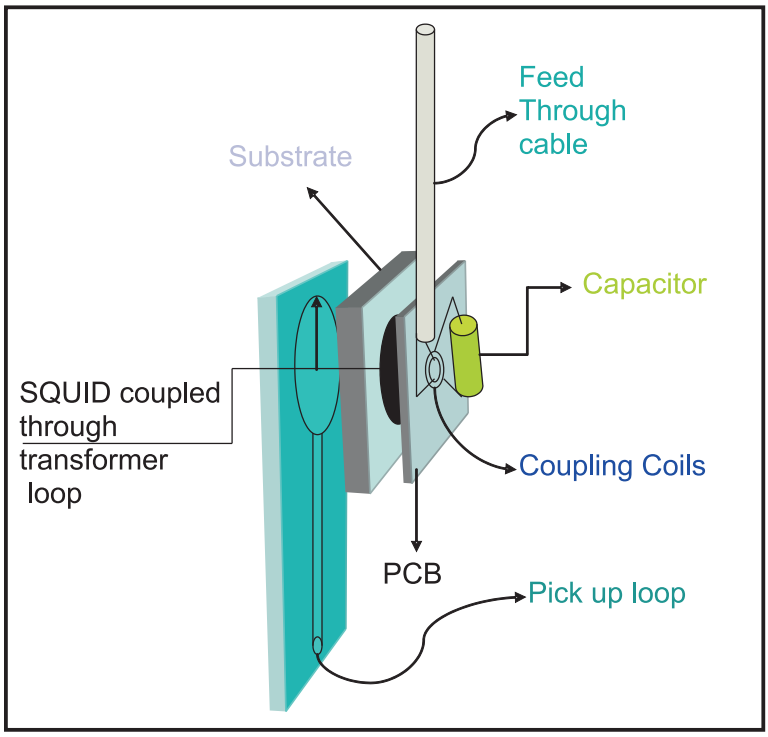

Figure 5.17: Schematic illustration of transformer coupling mechanism in order to improve the spatial resolution of SSM.

By performing the wire scan experiments we got the following concluding remarks which encouraged us to develop a new setup with the necessary conditions:

- Sample to SQUID height should be reduced to a few micrometers.
- Substrate resonator is not a good choice when trying to improve the spatial resolution. Where as, in the case of field sensitivity, it serves as a flux concentrator and enhances the signal level and thus provides better results compared to the LC-tank circuit.
- In order to improve the spatial resolution one needs to shield the resonator and SQUID washer area with proper shield.
- For higher resolution, flux transformer kind of configuration can be used. But this should be with an appropriate engineering concept at the front-end so that sample to SQUID distance does not increase.

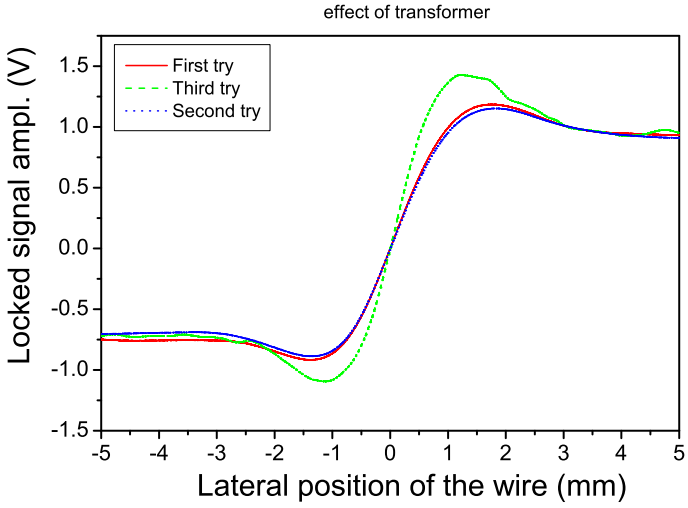

Figure 5.18: Results of magnetic distance measurement and fitting data with approximate model.

5.3.1.5 Results from System II (Prototype system)

The observation from the previous measurements dictated that use of rf-Gradiometer will be more beneficial for the sake of improving the field resolution, especially when there is excessive background noise. So in order to make use of the inherent noise cancellation properties of gradiometer structure, a prototype system has been made and has been discussed in section 5.2.3. Here we present the results obtained by scanning a wire carrying an ac current on top of the gradiometer. Figure 5.19 shows the expected behavior of the SQUID response for different positions of the wire.

Analysis of the above figure with respect to the flux threading the SQUID can be explained as: at Position "A" the flux produced from wire is just starting to enter the gradiometer washer area and so circulating current which tries to oppose the flux causing the magnitude of the locked signal to start increasing. This is till the point "B" where negative flux lines also start to enter the washer area. As the flux due to external source, which is entering and leaving the washer area, becomes almost the same, the circulating current generated due to external field also decrease causing a decrease in the magnitude of the SQUID signal. At point

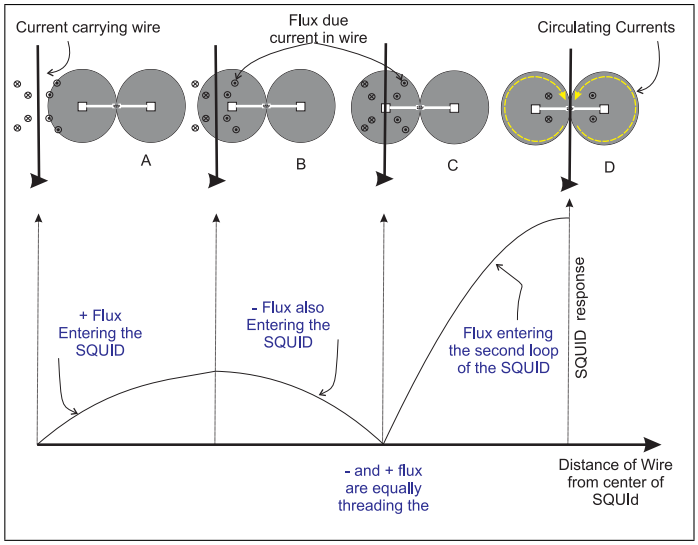

Figure 5.19: Conceptual diagram for the Expected SQUID response for the scanning of wire with an ac current regarding the position of the wire with respect to the center of the gradiometer.

"C", when the wire is just above the loop area, or half way on the washer area, the flux entering and leaving the washer becomes equal and so the circulating currents cancel each other in such a way that the SQUID response becomes zero. After point C, Flux due to wire also starts to enter the second washer area and as shown, the circulating currents are such a way that the total current faced by the junction adds up to give maximum response at point "D". After point D, it would follow the same behavior as discussed for points C, B, and A. This simple analysis based on the flux lines gives insight into the expected response for a single wire and for multiple wires carrying currents in same directions as well as different directions. It is expected that wires having current in the same direction would behave just like one wire but with higher magnitude, where as for opposite current directions,we would have minimum at the center and max peaks at both sides of this minimum. The results obtained from the prototype system are discussed as follows:

- **Effect of Applied Field:** In order to see the effect of applied field by either decreasing the current though the sample or by changing the height of the wire from the SQUID, a set of scans have been made and the results are shown in Figure 5.20. Due to the problem of friction, while sliding the

wire on the surface of the glass there were some unwanted jumps in the measurements, which also limited the field resolution down to 400pT.

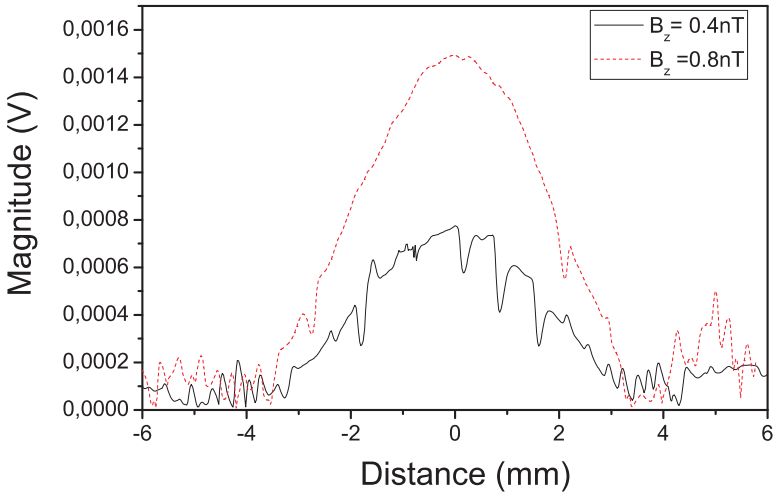

Figure 5.20: Effect of applied field to find the field resolution of the system.

- **Effect of Applied current direction through wire:** To observe the Effect of direction of current through the wire and correlate it with the above mentioned analysis, the experiment set has been repeated for two wires separated by about a distance of 1mm.

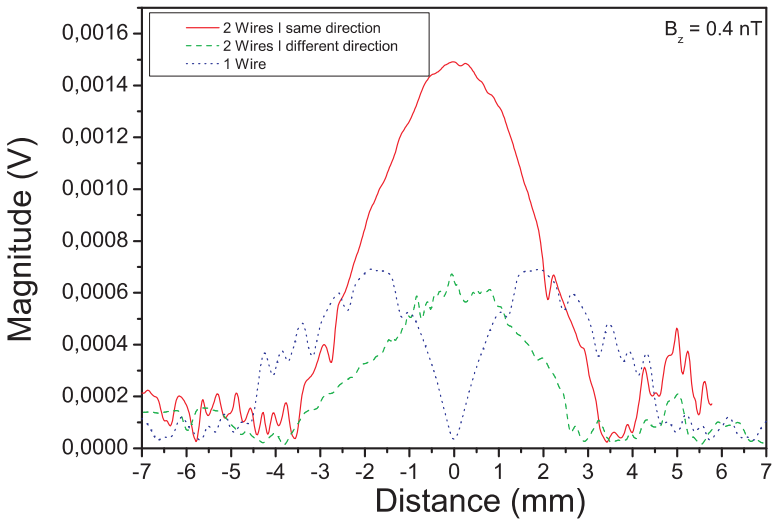

Figure 5.21: Effect of direction of the current on the response of the SQUID.

It is clear from Figure 5.21 that the results predicted earlier quite closely match with the experimental results. This is while again here it is obvious

that the system noise does not let us to see the side lobes clearly at low applied fields.

- **Ultimate Resolution:** With the aim to find the ultimate resolution for wire scanning, where the length of the wire puts limits on the spatial resolution, we have found that the signal is easily detectable down to 400pT, as shown in Figure 5.22.

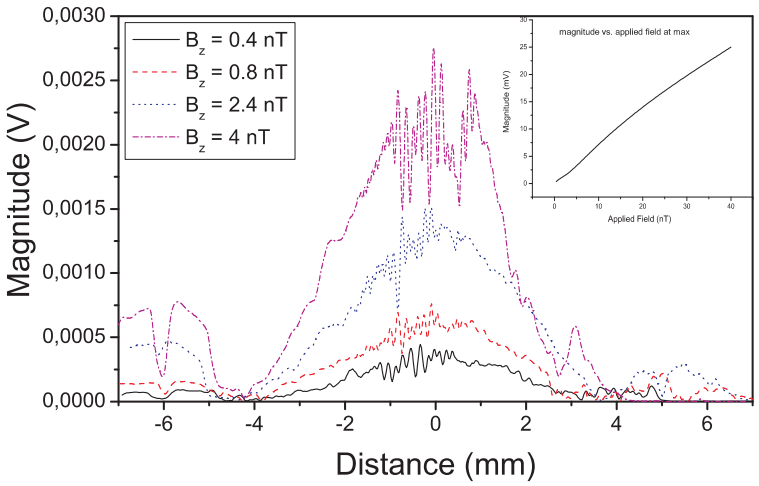

(a)

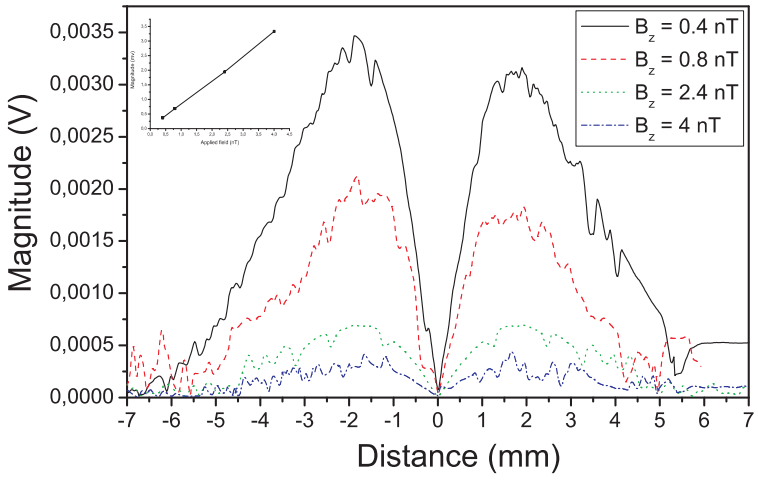

(b)

Figure 5.22: Finding the ultimate field resolution for wire scanning sample; (a) when the current through the wires are in the same direction, (b) when the current direction in the wires are apposite with respect to each other.

These scanning results suggest that one needs to decrease the sample size in order to improve the field and spatial resolution. This is while by decreasing the distance between the sample and the SQUID, high field sensitivity can be achieved. So in order to improve the system we made the samples by using the concept of dipole and the results obtained from these scans is studied in the next sub section.

5.3.2 Dipole scanning

5.3.2.1 Sample preparation

Dipoles with different sizes have been made by using a simple fabrication technique shown in Figure 5.23. A thin wires from 75μm to 150μm thickness have been used for making a dipole loops of different sizes. The rest connection part of the wires were twisted while care were taken to ensure that the twist loop size be much smaller than the original diameter of the dipole loop.

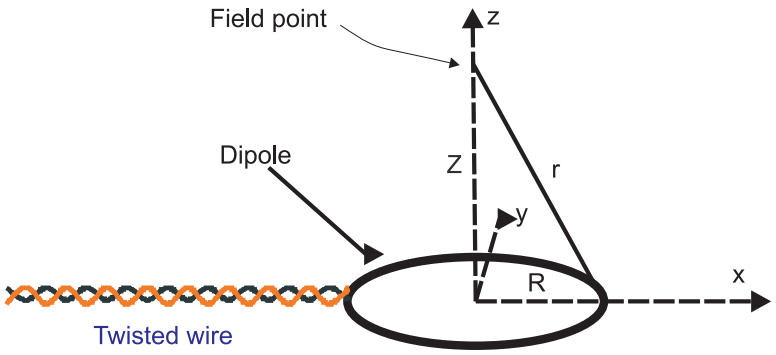

Figure 5.23: Visualization of a magnetic particle by the use of small loop of fixed diameter; where wire twisting has been used to decrease the effect of wires.

For such a configuration the magnetic field at a distance "z" for a loop with radius R can be written as [128];

$$B_z = \frac{\mu_0 \left(2\pi R^2\right) I}{4\pi \left(Z^2 + R^2\right)^{\frac{3}{2}}}. \tag{5.11}$$

Here we see that "Z", which is the distance between the sample and the SQUID, plays an important rule for sensing the magnetic field. In our case by fixing the distance z, we have changed the magnetic field by changing the current through the sample in order to measure the ultimate field resolution of the system.

5.3.2.2 Field sensitivity measurements

With a simple configuration, in which a dipole with a loop diameter of about 150 μm, is scanned directly on top of a gradiometer, field sensitivity down to few tens of **pT** has been obtained as shown in Figure 5.24.

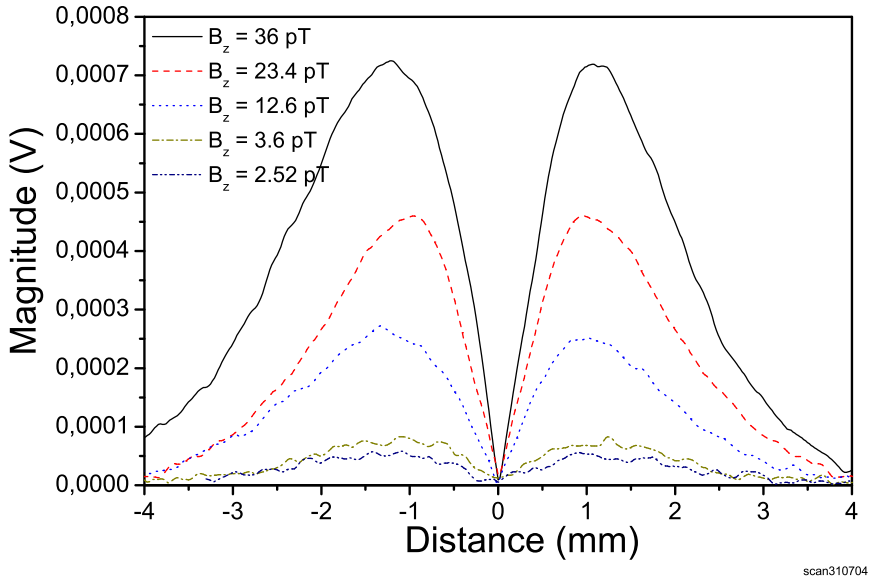

Figure 5.24: Field resolution by using 150μm diameter dipole configuration with a distance of about 2 mm between the sample and the SQUID.

Observed field sensitivity was limited by the factor that distance from the sample to the SQUID was about 2mm. Based on our previous observations from wire scanning and its dependence on sample to sensor distance, we know that distance plays a very important rule for improving field sensitivity. So by simply reducing the sample to sensor distance down to 1.2 mm we got the absolute resolution of our system to be few hundreds of **"fT"**, as shown in Figure 5.25.

Due to the thickness of SQUID substrate, we were constrained to further decrease the distance. Here at this point, if one needs to improve the field resolution, the substrate thinning concept and back side SQUID coupling technique could also be used. In such a case, according to our speculation, field resolution can be enhanced up to few hundereds of fT range.

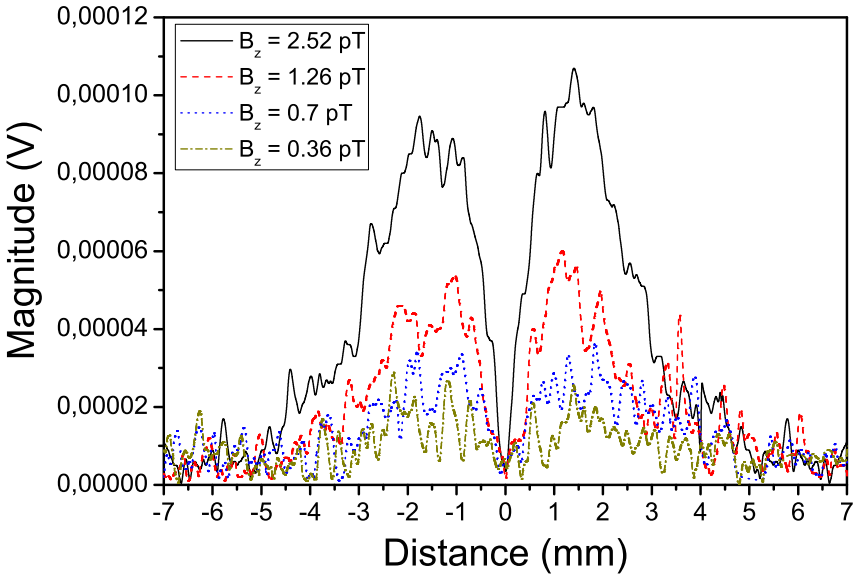

Figure 5.25: Maximum achieveable field resolution with 1.2 mm distance between the SQUID and the sample.

Here it is observable that there are high jumps in the measurements that can be interpreted as being due to the fact that at very low applied fields, the jumps associated with motion and the friction between the sample and the glass cause jumps in the field, which has magnitude higher than the field itself. This can be reduced by using piezo-electric motion control system, which gives much more smooth motion.

5.3.2.3 Spatial Resolution measurements

In order to find the spatial resolution of the system, at the first place the effect of field generated by two dipoles having current in the same or opposite direction

has been observed. The results are shown in Figure 5.26.

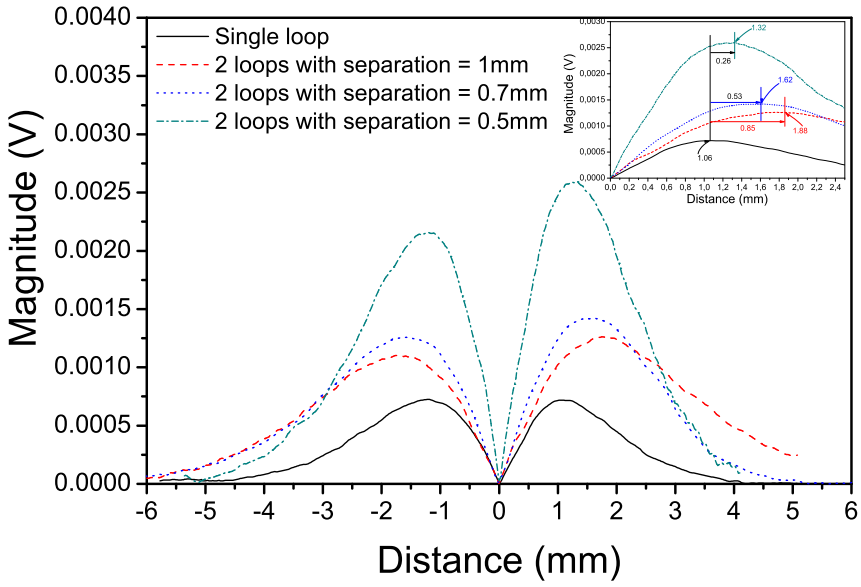

Figure 5.26: Effect of applied current direction and the separation between two dipoles.

The next step was to see what the spatial resolution of the system is and for this very purpose, dipoles with fixed loop area but different separations have been made. The results obtained from this study are shown in Figure 5.26. Here, we see that as the distance between the dipole is being decreased, the signal level increases suggesting that the fields are being added and after some point they will just behave as a single power with double the magnitude. As shown in the inset of the graph, while the shift in the peak, gives us some sort of proportionality due to noise in the system, it cannot be formalized. But still the shift in the peaks can be related to the separation between two dipoles. The optimum resolution of the system found by this simple scanning method has been found to be down upto 150μm, while it can further be reduced by using the concept of shielding and transformer. This method of improving the spatial resolution, which is beyond the scope of this thesis, will be discussed briefly in next section as future work related to this study.

Chapter 6

Summary and Conclusion

The motivation for this thesis was to design a magnetic imaging system with high field sensitivity and high spatial resolution using rf-SQUIDs, the most sensitive sensors available to date. In the course of this research, rf-SQUIDs were fabricated, optimized and implemented in a Scanning SQUID microscope, used for unshielded environment applications. Different designs for the microscope have been proposed and tested. Suggestions to overcome the different bottlenecks related to the front end assembly, have been suggested. The following section summarizes this dissertation.

6.1 Summary

As a recapitulation of the major points from the chapter on Josephson Junctions, the following observations were made for junction arrays on both bi-crystal $SrTiO_3$ substrates, and the $LaAlO_3$ substrates with steps developed using a CIBE process. Most of the SEJs with ∼200 nm deep steps and higher, showed RSJ type characteristics. This is while, all the BGBJs showed RSJ type characteristics. The SEJs had typically lower J_c and higher ρ_n values compared to those of the BGBJs, resulting in close I_cR_n products. Comparison of the present $I-V$ characteristics of our types of the junctions suggests that SEJs are more suitable

junctions for obtaining lower white noise devices. All the characterized junctions showed clear, linear $I-V$ curves for short junction characteristics at temperatures corresponding to $W_j/\lambda_j <\sim 2$, which served as a criterion for obtaining low noise devices in both technologies. These favorable results in linear flux flow free $I-V$ curves for both types of junction, do not impose a limit for obtaining low noise micron size junction devices operating at liquid Nitrogen temperature.

Two major, relatively, high and low field dependencies were obtained for our SEJ devices. A relatively high field sensitivity of the I_c of our SEJs and the resulting SEJ rf-SQUID were correlated to the junction widths, as for the BGBJ devices. The high field-sensitive SEJs also resulted in a need for submicron junction widths for applications in an unshielded environment. Due to the low J_c of our 200 nm thick film quality SEJs on the CIBE steps, this resulted in rf-SQUID designs with high B_a sensitivities inappropriate for operation in an unshielded environment. The obtained SEJs with relatively low field-sensitive I_c resulted in rf-SQUIDs with low B_a sensitivities appropriate for operation under the Earth's magnetic field, while carrying junction widths of 2-3 μm. The low field-sensitivity of some of our SEJs is associated with the structure of the low I_c junctions at the steps. Considering the effect of the $I-V$ characteristics of the junctions, the SEJs with low field-sensitive I_c are favorable in fabrication of low noise rf-SQUID for applications in an unshielded environment.

All the characterized BGBJs showed a well defined Fraunhofer-pattern-like magnetic field dependence on I_c, indicating an almost uniform junction barrier. A well defined B_a dependence for an array of SEJs could not be obtained as they showed various field dependencies as well as a higher spread of the I_c. The field sensitivity of the BGBJs led to the need for submicron-junction rf-SQUID designs, decreasing the yield of this kind of devices with appropriate optimum operating temperature.

The study of rf-SQUID for microscope applications during the investigation of the effects of the step structure and the film characteristics on the noise and operating temperature range of the SEJ rf-SQUIDs, led to the following results. For normal incident IBE process, a re-deposition of substrate material was formed

at the edges, as well as, on the side walls of the step. This re-deposition was dependent on the substrate materials being the most for the $LaAlO_3$. The re-deposited material at the edges is interpreted to be the main source for very low yield and high $1/f$ noise SQUIDs. Using a developed combinatorial IBE process, sharp steps were developed. By control of the height of the CIBE steps made using the Combinatorial Argon IBE process, the operating temperature range, ΔT_{op}, of the SQUIDs could be tuned to the desired liquid Nitrogen temperature. Low step heights resulted in high temperature and narrow ΔT_{op} ranges. This was in agreement with the I_c measurement of the junctions of the SQUIDs as well as the test junction arrays on similar type of the steps. Decrease of the junction width for the same step heights reduced the temperature of ΔT_{op} of the devices.

The white noise level in our devices could mostly be correlated to their V_{spp}. The $1/f$ type noise spectra was observed to be mostly dependent on the utility of the steps and the films at the steps, inspected by high resolution SEM. The low frequency $1/f$ noise of the SQUIDs made on the CIBE steps could be classified into two major categories. One type of the $1/f$ noise increased as the temperature decreased. This was associated to the noise in the junction caused by the I_{c-j} fluctuations. The second type of the $1/f$ noise spectra was found to increase as the temperature increased and was associated to the flux hopping mechanism in the film. The latter type of the noise was found in films with relatively high density of precipitates while the former was mostly observed in samples with smooth film surfaces but with defects at the edge of the steps. High yield of low $1/f$ noise rf-SQUIDs was achieved using high quality films on the CIBE steps on $LaAlO_3(100)$. The $I-V$ curves of the junctions of the SQUIDs showed RSJ type behavior with field dependency as for uniform junctions. The white noise level of the SQUIDs was mainly following the trend of the V_{spp} increasing as the voltage signal decreased.

Two distinct applied background magnetic field, B_a, sensitivities were observed for our rf-SQUIDs made on sharp CIBE steps. While some SQUIDs showed high B_a sensitivities, others showed much lower B_a sensitivities resulting in relatively magnetically stable devices under earth magnetic field. The magnetic field dependence of the I_c of the SQUID junctions was measured after opening the flux

focusing washer area of the devices. The B_a dependence of the I_c of the junctions followed that of the V_{spp} of the high field sensitive SQUIDs with a slight discrepancy associated to calibration accuracy of the fields. The study of the drop of the V_{spp} of high B_a sensitive devices led to the need of rf-SQUID layout designs with junction widths in the range of 0.6-1.2 μm to obtain magnetically stable devices for applications in unshielded environments.

We also obtained low noise magnetically stable rf-SQUIDs with 2-3 μm wide junctions proper for operation under the earth's magnetic field. The V_{spp} signal of the magnetically stable devices dropped by less than about 10% under $B_a \sim 50\mu$T. Isolated junctions and junctions of the low field-sensitive SQUID also showed the same low field-dependence behavior. The field sensitivity of the test junctions was correlated to that of the SQUID junctions through the effective area of their patterns. Effect of the flux focusing area of the SQUIDs, allowed the observation for the B_a dependence of the SQUID junctions below $B_a = 1mT$ by intensifying the field at the junction. The low and high B_a sensitivities of the SQUIDs might be associated to the physical position of the working junction of the devices at the steps and their orientation with respect to the B_a, as junctions with shielded effective area or an area parallel to the B_a are expected to have low field-sensitivity.

Asymmetric multi junction YBCO rf-SQUID magnetometers and gradiometers were fabricated using 200 nm thick PLD YBCO films on symmetric 30^o grain boundary (GB) bi-crystal $SrTiO_3$ substrates. Layouts based on asymmetric junctions with widths ratio of 1/2, 1/3, and 1/4 were implemented, avoiding both large area films on the substrate GB and large inductances. Low $1/f$ noise characteristics with corner frequency of about 10Hz for a white noise level of about 40 $\mu\Phi_0$, was obtained for the SQUIDs. The $1/f$ noise behavior of the above devices was found to be lower compared to that of the conventional designs. It showed a dependence on the width of the larger junction, increasing with increasing the junction width. While all the characterized junctions show RSJ behavior, the operating temperature range of the devices reduced for higher optimum operating temperature. The $1/f$ noise of both type of devices increased with decrease in temperature indicating that the $1/f$ noise was determined by the junctions.

The white noise of these devices was found to be dependent mainly on the flux to voltage transfer function signal. The fabricated SQUIDs showed a wide spread of junction parameters hindering the control of the optimal operating temperature of the devices by the layouts. Verification for the spread of I_c parameter was done by making arrays of 3 to 25 serial junctions, which showed variation of the I_c up to about 50% of its mean values. As a result, the SEJ based rf-SQUIDs showed to be more favorable for the use in the considered SQUID microscope designs.

To investigate the impediments faced with the front-end assembly of the considered scanning SQUID microscope and their related solutions, two basic rf coupling techniques, LC tank circuit and co planar resonator, have been studied. This was on the basis of their suitability to couple the SQUIDs with the electronics for maximum SQUID signal level, improving the field sensitivity, reducing the space in the front-end by appropriate design, reducing noise level, and increasing the capability to be shielded for unwanted pickups. From the study on rf-coupling techniques, it can be concluded that though coplanar resonator provides better signal level compared to conventional LC tank circuit for bare SQUIDs without any shield, it suffers from higher suppression under shielding and unwanted pickup due to a large flux focusing. It is therefore suggested to optimize the conventional LC tank by decreasing the diameter of the pick up loop to provide high V_{spp}. This also provides less percentage suppression under shielding compared to resonators.

Regarding the sample to sensor distance, appropriate thickness of substrate, 0.4 mm for $LaAlO_3$ and 0.5 mm for $SrTiO_3$, provides an alternate method to reduce the sample to sensor distance while providing maximum signal level.

To avoid unwanted pick up and noise coupling, shielding techniques for SQUID and particular rf coupling techniques have been explored to improve the shielding factor, while coping with the requirement of high field-sensitivity. Effect of electronics (based on working frequency range), tank circuit (resonance frequency), resonator (different configuration), temperature, and shield area has been investigated to optimize the system for high field-sensitivity and high spatial resolution.

Applied shield put some constraints on the front-end assembly as;

- film used for shielding should be as thick as possible ($\sim$ 400 nm-500 nm) so that better shielding currents can be achieved,
- an appropriate electronics should be found for particular choice of tank circuit, which provides better signal level as well as low noise,
- SQUIDs with higher J_c are preferred as under shielding the reduction in the inductance is compensated with the J_c.

In the final chapter on the design of and results from the scanning SQUID microscope, the following paragraph summarizes the work done. Different microscope setups were considered to test the underlying principle of scanning SQUID microscopy by using either magnetometer or gradiometer as basic sensor. Thorough study and countless efforts have been persuaded for;

- improving the temperature stability of the systems
- appropriate shielding of electronics and systems for noise reduction
- appropriate scanning mechanism designs with the constraint of keeping the sample at room temperature and the SQUID at Nitrogen temperature,

While at the same time, keeping the distance between them as low as possible. Using the simple design concepts, where we used Liquid Nitrogen as cooling agent and gradiometer SQUID configuration with optimized tank circuit, field-sensitivity down to few hundred fT range and spatial resolution up to few hundred μm have been shown. This is while method of using flux transformer has been proposed as the future work to further improve the spatial resolution and the field-sensitivity of the systems.

6.2 Conclusion

After a thorough investigation of Josephson Junction fabrication techniques for Step Edge Junctions (SEJ) and Bi-Crystal Grain Boundary Junctions (BGBJ), it has been concluded that the SEJs with low field-sensitive I_cs are favorable for fabrication of low noise rf-SQUIDs for applications in an unshielded environment. This deduction is based on the following observations:

- Although for SEJs the I_c is lower and R_n is higher compared to BGBJs, the overall I_cR_n product is the same.
- The SEJs provide low white noise level compared to the BGBJs.
- All the BGBJs that were fabricated during the course of this work, showed Fraunhofer-pattern-like magnetic field dependence; thus in order to avoid this field dependence for SQUIDs, it is required to make the junctions in sub-micron sizes.
- SEJs produced by using CIBE process provide low field sensitivity compared to the ones made by conventional IBE process. Re-deposition of the substrate material at the step-edge in conventional IBE process not only affects the yield but also causes high $1/f$ noise devices.
- SQUIDs produced by SEJs made with CIBE process, and with low field dependence waive the requirement of having sub micron size junctions. This is in contrast with the cases for BGBJs and high field sensitive SEJ made by conventional IBE process.
- CIBE process also provides control on the working temperature range of the SQUIDs. Lowering the step height narrows ΔT_{op} and also shifts it towards higher temperatures ΔT_{op}, whereas at constant step height, reducing the junction width shifts ΔT_{op} to lower temperatures.
- The junctions typically showed two types of $1/f$ noise behaviors - increasing noise with increasing temperature and increasing noise with decreasing

temperature. Both dependencies can be reduced by improving the film and step structure.

- To improve the BGBJ based SQUID characteristics, new asymmetric designs has been investigated, which unquestionably reduces the $1/f$ noise compared to the conventional designs. The inherent spread of BGBJs reflect the same spread in the characteristics of the SQUIDs, which makes them unsuitable for usage.

- It has also been observed that by using CIBE process, high yield and low $1/f$ noise with low magnetic field-dependent rf-SQUIDs are achievable with junction widths of 2-3 μm.

As a result of the above mentioned observations, the SEJ based rf-SQUIDs have been chosen for use in our SQUID microscope designs.

Having chosen SEJ, for the Scanning SQUID Microscope, the next step was to investigate the front-end assembly. This study on the bottlenecks associated with front end revealed that coplanar resonator configuration with proper shielding provides better SNR and ease in coupling mechanism for use in gradiometer configuration. For shielding the gradiometer and resonator from unwanted pickups, thick YBCO film shielding has been suggested and has also been demonstrated to have better shielding due to its capability of retaining the higher shielding currents. For further improving the coupling between the SQUID, the resonator, and the sample, the optimum substrate thickness for SQUID fabrication has been found to be 0.4 mm for $LaAlO_3$ and 0.5 mm for $SrTiO_3$.

Different microscope designs were investigated and it finally led to a prototype system, which provides the best field resolution, about 200 fT and a spatial resolution in the range of 100 μm. This can further be improved by using the concept of flux transformer with either single layer or multi-layer self-shielded configurations [129]. Gradiometer provides ease in coupling the sample through the flux transformer in one of its loop and with resonator in the second loop. This, plus its inherent noise cancellation property enabled us to choose gradiometer configuration for the microscope design. Here, self-shielded transformer provides

not only shielding of its own arms from unwanted pickup but also provides a shield to gradiometer and the resonator from the environment. Further improvements are possible with this flux transformer configuration together with YBCO shield, either in Flip-Chip configuration or multi-layer structure.

The various achievements during different stages of this research resulted in numerous journal publications and conference contributions, and they are listed in the following section.

6.3 List of Publications

6.3.1 Journal Publications

- "$1/f$ Noise Characteristics of SEJ Y-Ba-Cu-O rf-SQUIDs on LaAlO3 Substrate and the Step Structure, Film, and Temperature Dependence," M. Fardmanesh, J. Schubert, R. Akram, M. Bick, Y. Zhang, M. Banzet, W. Zander, H.-J. Krause, H. Burkhart, and M. Schilling, IEEE Trans. on Appl. Superconductivity, Vol. 11, No. 1, p. 1363, 2001.

- "Dependence of the substrate structure and the film growth at the junction of YBCO SEJ rf-SQUIDs on the IBE process and effects on the SQUID's characteristics," M. Fardmanesh, J. Schubert, R. Akram, M. Bick, M. Banzet, W. Zander, J.-H. Krause, Physica C, Vol. 372, p. 240, 2002.

- "Junction Characteristics and Magnetic Field Dependence of Low Noise Step Edge Junction rf-SQUIDs for Unshielded Applications," M. Fardmanesh, J. Schubert, R. Akram, A. Bozbey, M. Bick, M. Banzet, D. Lomparski, W. Zander, Y. Zhang, and H.-J. Krause, IEEE Trans. on Appl. Superconductivity, Vol. 13, No. 2, p. 833, 2003.

- "Noise, Junction Characteristics, and Magnetic Field Dependencies of Bicrystal Grain Boundary Junction rf-SQUIDs," M. Fardmanesh, J. Schubert, R. Akram, M. Bick, M. Banzet, W. Zander, Y. Zhang, and H.-J.

Krause, IEEE Trans. on Appl. Superconductivity, Vol. 13, No. 2, p. 873, 2003.

- "Analysis of Electrical Characteristics and Magnetic Field Dependencies of YBCO Step Edge and Bi-crystal Grain Boundary Junctions for rf-SQUID Applications," M. Fardmanesh, J. Schubert, R. Akram, M. Bick, M. Banzet, W. Zander, Y. Zhang, H.-J. Krause, Supercond. Sci. Technol. 17. S375-S380, 2004.

6.3.2 Conference Contributions

- M. Fardmanesh, J. Schubert, R. Akram, M. Bick, M. Banzet, W. Zander, J.-H. Krause, "$I-V$ characteristics of single and arrays of YBCO bi-crystal grain boundary and Step Edge Josephson junctions and the temperature dependence," 5th European Conference on Applied Superconductivity (EUCAS), Copenhagen, Denmark, 26-30 August 2001.

- M. Fardmanesh, J. Schubert, R. Akram, M. Bick, K. Barthel, W. Zander, Y. Zhang, M. Banzet, J.-H. Krause, "Asymmetric Multi-Junction YBCO rf-SQUID Magnetometer and Gradiometer designs on Bi-crystal Substrates and the Noise and Junctions Characteristics," 8th International Superconductive Electronics Conference (ISEC2001), Osaka, Japan, 19-22 June 2001.

- M. Fardmanesh, J. Schubert, M. Banzet, R. Akram, M. Bick, W. Zander, Y. Zhang, M. Schilling, J.-H. Krause, "YBCO SEJ rf-SQUID Magnetometer and Gradiometers: Effects of the step structure on the film at the junctions, noise, and the yield," 8th International Superconductive Electronics Conference (ISEC2001), Osaka, Japan, 19-22 June 2001.

- M. Fardmanesh, J. Schubert, R. Akram, M. Bick, M. Banzet, W. Zander, Y. Zhang, and H.-J. Krause, "Noise, Junction Characteristics, and Magnetic Field Dependencies of Bicrystal Grain Boundary Junction rf-SQUIDs," Applied Superconductive Conference, Houston, TX, August 2002.

- M. Fardmanesh, J. Schubert, R. Akram, A. Bozbey, M. Bick, M. Banzet,

D. Lomparski, W. Zander, Y. Zhang, and H.-J. Krause, "Junction Characteristics and Magnetic Field Dependence of Low Noise Step Edge Junction rf-SQUIDs for Unshielded Applications," Applied Superconductive Conference, Houston, TX, August 2002.

- M. Fardmanesh, J. Schubert, R. Akram, M. Bick, M. Banzet, D. Lomparski, W. Zander, Y. Zhang, and H.-J. Krause, "Analysis of Electrical Characteristics and Magnetic Field Dependencies of YBCO Step Edge and Bi-crystal Grain Boundary Junctions for rf-SQUID Applications," 6th European Conference on Applied Superconductivity (EUCAS), Napoli, Italy, September 2003.

- M. Fardmanesh, J. Schubert, R. Akram, M. Bick, M. Banzet, D. Lomparski, W. Zander, H.-J. Krause, "Magnetic Field Dependencies of YBCO Step Edge and Bi-crystal GB-JJ Based rf-SQUIDs," 9th International Superconductive Electronics Conference (ISEC2003), Sydney, Australia, July 2003.

- R. Akram, T. Eker, A. Bozbey, M. Fardmanesh, J. Schubert, M. Banzet., "Study of Correlation between the flux to voltage transfer function signal of rf-SQUID and the rf pumping frequency and power," III. Ulusal Y*ü*ksek Sıcaklık S*ü*periletkenler Sempozyumu, Bolu, Turkey, 20-22 June 2005.

- R. Akram, M. Fardmanesh, J. Schubert, W. Zander, M. Banzet , D. Lomparski, M. Schmidt, and H.-J. Krause, "Impediments and related solutions to develop high field sensitive and high spatial resolution Imaging Systems", III. Ulusal Y*ü*ksek Sıcaklık S*ü*periletkenler Sempozyumu, Bolu, Turkey, 20-22 June 2005.

- R. Akram, M. Fardmanesh, J. Schubert, M. Banzet, M. Schmidt, and H.-J. Krause, "Design and optimization of a prototype HTS rf SQUID microscope setup for magnetic nanoparticle detection and the results," III. Ulusal Y*ü*ksek Sıcaklık S*ü*periletkenler Sempozyumu, Bolu, Turkey, 20-22 June 2005.

- R. Akram, M. Fardmanesh, J. Schubert, H.-J. Krause, Y. Zheng, M. Banzet,

W. Zander, M. Schmidt, and D. Lomparski, "Developments towards realization of High Tc rf-SQUID based SQUID Microscope for High Resolution Magnetic Imaging System," International Summer School on Superconductive Electronics, Pisa, Italy, 7th July 2005.

- R. Akram, M. Fardmanesh, J. Schubert, W. Zander, M. Banzet, D. Lomparski, M. Schmidt, and H.-J. Krause, "Front-end Assembly Optimization for High Temperature SQUID Applications for High Field Sensitive and High Spatial Resolution Magnetic Field Imaging Systems" 7th European Conference on Applied Superconductivity (EUCAS), Vienna, Austria, 11-15 September 2005.

- M. Schmidt, H.-J. Krause, M. Banzet, D. Lomparski, J. Schubert, W. Zander, Y. Zhang, R. Akram and M. Fardmanesh, "Setup of an HTS rf SQUID microscope for magnetic nanoparticle detection," 7th European Conference on Applied Superconductivity (EUCAS), Vienna, Austria, 11-15 September 2005.

6.3.3 Patent

"Self -shield multi-layer thin film SQUID gradiometer and magnetometer transformer" , M. Fardmanesh, J. Schubert, R. Akram, M. Banzet, in progress for German and European patents, filed in Sept. 2003.

Bibliography

[1] http://www.hostultra.com/∼mhegazy/pld.htm.

[2] M. Fardmanesh, J. Schubert, and M. Banzet., "Asymmetric step-edge junction rf-SQUID design," Germany 101 53 705.0, and Europe," Patent.

[3] M. Fardmanesh, J. Schubert, and K. Bartel, "Low noise high-tc rf-SQUID bi-junction magnetometers and multi-junction gradiometers on bi-crystal substrates," Germany, 199 02 580.0-35, Europe, USA, Japan," Patent.

[4] M. Fardmanesh, J. Schubert, R. Akram, M. Bick, Y. Zhang, M. Banzet, W. Zander, J. Krause, and M. Schilling, "l/f noise characteristics of SEJ YBCO rf-SQUIDS on LaAIO, substrate and the step structure, film, and temperature dependence," *IEEE Trans. Appl. Superconductivity*, vol. 11, pp. 1363–1366, 2001.

[5] M. Fardmanesh, J. Schubert, M. Banzet, W. Zander, Y. Zhang, and J. Krause, *Physica C*, vol. 372, pp. 240–5, 2002.

[6] M. Schmidt, "SQUID mikroskop zur detektion magnetischer nanopartikel," Diplomarbeit, Forschungszentrum Juelich, July 2003.

[7] R. Boll, *Introduction to Magnetic sensors*, k.j. overshott ed. VCH, Weinheim, 1989, vol. 5.

[8] M. Gibbs and P. Squire, *Applications of magnetic sensors*, r. boll, k.j. overshott ed., 1989, vol. 5.

[9] W. Happer, "Optical pumping," *Rev. Mod. Phys.*, vol. 44, pp. 169–249, 1972.

[10] E. B. Alexandrov, V. A. B. Bonch, and N. N. Yakobson, "Magnetometers based on the optical pumping of atoms: status and prospect," *sov. J. opt. Technol*, vol. 60, pp. 756–765, 1993.

[11] F. Primdahl, "The fluxgate magnetometer," *J. Phys. E, Sci. Instrum*, vol. 12, pp. 241–253, 1979.

[12] C. L. Chien and C. R. Westgate, *The Hall effect and its applications*. Plenum press N.Y., 1980.

[13] R. Popovic and W. Heidenreich, *Magnetogalvanic Sensors*. Weinheim VCH, 1989, vol. 5.

[14] H. Wieder, "Hall generators and magnetoresistors," Pion, London, 1971.

[15] N. Smith, F. Jeffers, and J. Freeman, "A high sensitivity magnetoresistive magnetometer," *J. Appl. Phys.*, vol. 69, pp. 5082–5084, 1994.

[16] "Mr SQUID and IMAG magnetometers, conducts, inc." 969 West Maude Ave., Sunnyale, CA94086 USA.

[17] "NKT research center A/S," Priorparken 878, DK-2605 Brondby, Denmark.

[18] "Necera, inc." 1000 Virginia Manor Road, Suite 300, Beltsville, Maryland 20705-4215, USA.

[19] "Sumitrno Electric, Ltd." Itami Research Laboratories, 1-1, 1-chome, Koya-kita, Itami, Hyogo, 664 Japan.

[20] "JSQ bmbh," Lankenstr. 29, 52428 Juilch, Germany.

[21] "Magnetosensor Inc." 9717-Apacific Heights Bd. San Diego, CA 92121, USA.

[22] "Tristan Technologies Inc." San Diego, CA 92121, USA.

[23] F. I. T. M. GmbH, P. O. Box 1147, D-31158 Bad Salzdetfurth, Germany.

[24] S. W. Goodyear, N.G.Chew, R.G.Humphreys, J.S.Satchell, and K. Lander., "Vertical c-axis microbridge junctions in ybacuo/prbacuo thin films," *IEEE Transactions on Applied Supercoductivity*, vol. 5, no. 2, June 1995.

[25] M. Fardmanesh, J. Schubert, M. Banzet, W. Zander, Y. Zhang, and J. Krause, *Physica C*, vol. 354, pp. 40–44, 2001.

[26] D. Jia and c.p. Foley, "trimming, stability and passivation of YBCO step-edge junctions," *Phsica C*, vol. 391, pp. 31–41, 2003.

[27] P. A. Nilsson, Z. G. Ivanov, H. K. Olsson, D. Winkler, and T. Claeson, "Bicrystal junctions and superconducting quantum interference devices in $YBa_2Cu_3O_7$ thin films," *J. Appl. Phys.*, vol. 75, no. 12, 1994.

[28] M. S. Dilorio, S. Yoshizumi, K. Y. Yang, J. Zhang, and B. Power, "Low noise dc SQUIDs at 77k," *IEEE Trans. Appl. Supercond.*, vol. 3, pp. 2011–2017, 1992.

[29] R. H. Ono, J. A. Beall, R. W. Cromar, T. E. Harvey, M. E. Johansson, C. D. Reintsema, and D. A. Rudman, "High- Tc SNS josephson microbridges with high resistance normal metal links," *Appl. Phys. Lett.*, vol. 59, pp. 1126–1128, 1991.

[30] J.-H. Krause, "SQUID magnetometers," ISG Forschungszentrum Juelich," Report, 2000.

[31] T. V. Duzer and C. W. Turner, *Principles of Superconductive Devices and Circuits*, 2nd ed. Printice Hall PTR, 1999.

[32] J. Clarke, "SQUID fundamentals." in *SQUID Sensors: Fundamentals, Fabrication and Applications*, H. Weinstock, Ed., vol. 329, NATO ASI Series E. Kluwer Academic Pbl., pp. 1–62.

[33] H. J. Krause, "SQUIDs fur die zerstorungsfreie prufung and flugzeugteilen, forschungsbericht spuraleitung," Bundesministerium fur bildung, wissenschaft, forschung und technologie. Forschungszentrum, Julich, 1999.

[34] ——, "Detektion von fremdkorpern in medikamenten und lebensmitteln mittels HTSL-SQUID," ISG Forschungszentrum Juelich," Final report, 2003.

[35] J. Vrba, "SQUID gradiometers in real environments," in *SQUID Sensors: Fundamentals, Fabrication and Applications*, H. Weinstock, Ed., vol. 329, NATO ASI Series E. Kluwer Academic Pbl., 1996, pp. 63–116.

[36] J. M. Jaycox and M. B. Ketchen, "Planar coupling scheme for ultra-low noise dc SQUIDs," *IEEE Trans. on Magnetics*, vol. MAG-17, pp. 400–403, 1981.

[37] G. Hildebrand and F. H. Uhlmann, "Inductance calculation for integrated supercondcuting structues by minimizing free energy," *IEE Trans. Appl. Supercond.*, vol. 5, pp. 2766–2769, 1996.

[38] H. Fuke, K. Saitoh, T. Utagawa, and Y. Enomoto, "Estimation of inductance for HTS dc SQUIDs in coplanar waveguide." *Jpn. J. Appl. Phys.*, vol. 35, pp. L1582–L1584, 1996.

[39] K. C. Gupta, R. Garg, and I. J. Bahl, *Microstrip Lines and Slotlines.* Artech House, Dedham, MA, 1979.

[40] R. Cantor, "DC SQUID: Design, optimization and practical applications." in *SQUID Sensors: Fundamentals, Fabrication and Applications*, H. Weinstock, Ed., vol. 329, NATO ASI Series E. Kluwer Academic Pbl., 1996, pp. 1–62.

[41] M. B. Ketchen, W. J. Gallagher, A. W. Kleinsasser, S. Murphy, and J. R. Clem, "The DC SQUID focuser," in *Superconducting QuantumInterference Devices and their Applications*, H. D. Hahlbohm and H. L. ü big, Eds. Walter de Gruyter, Berlin, 1985, pp. 865–871.

[42] M. Matsuda, Y. Murayama, S. Kiryu, N. Kasai, S. Kashiwaya, M. Koyanagi, T. Endo, and S. Kuriki, "Directly-coupled dc SQUID magnetometers made of BSCCO oxide films." *IEEE Trans. on Magnetics*, vol. 27, pp. 3043–3046, 1991.

[43] D. Koelle, A. H. Miklich, F. Ludwig, E. Dantsker, D. T. Nemeth, and J. Clark, "dc SQUID magnetometers from single layers of YBCO," *Appl. Phys. Lett.*, vol. 63, no. 16, pp. 2271–2273, 1993.

[44] H. R. Yi, Z. G. Ivanov, D. Winkler, Y. M. Zhang, H. Olin, P. Larsson, and T. Claeson, *Appl. Phys. Lett.*, vol. 65, p. 1177, 1994.

[45] C. Bowich, "RF circuit design," USA: howard W. Sams and Company, Inc., 1982.

[46] R. Ludwig and P. Bretchko, *RF circuit design.* New Jersey: Prentice Hall, 2000.

[47] W. D. H., *Phase-Locked Loop circuit design.* Prentice Hall Inc. Nw Jersey, 1991.

[48] T. Akkar, MS Thesis, Bilkent University, 06800, Ankara, Turkey, June 2005.

[49] M. Muck, J. Dechert, J. Gail, M. von kreutzbruck, S. Schone, and R. Weidel, "Response of radio frequency SQUIDs to electromagnetic interference," *Rev. Sci. Instrum.*, vol. 66, pp. 4690–4694, 1995.

[50] W. Gopel, J. Hesse, and J. n. Zemel, *W. Gopel, J. Hesse, J. N. Zemel.* Physikalisch technische Bundesanstalt, Berlin, 1989, vol. 5.

[51] W. G. Jenks, S. S. H. Sadeghi, and J. P. W. Jr, "SQUIDs for nondestructive evaluation," *Appl. Phys.*, vol. 30, pp. 293–323, 1997.

[52] "Online SQUID," http://www.jsquid.com.

[53] D. Gill, B. Block, C. Conrad, B. Wessels, and S. Ho, *Appl. Phys. Lett.*, vol. 69, p. 2968, 1996.

[54] F. Walker and R. McKee, *Appl. Phys. Lett.*, vol. 65, p. 1495, 1994.

[55] R. McKee, F. Walker, and M. Chisholm, *Phys. Rev. Lett.*, vol. 81, p. 3014, 1998.

[56] P. Barrios and H. Kim, *Appl. Phys. Lett.*, vol. 73, p. 1017, 1998.

[57] B. Stritzker, J. Schubert, U. Poppe, W. Zander, U. Kruger, A. Lubig, and C. Buchal, *J. Less-Common Met.*, vol. 279, pp. 164–165, 1990.

[58] J. Schubert, M. Siegert, M. F. andD W. Zander, M. Proempers, C. Buchal, J. Lisoni, and C. H. Lei, *Appl. Surface Science*, vol. 168, pp. 208–214, 2000.

[59] A. I. Braginski, *Sensors: Fundamentals, Fabrication and Applications*, h. weinstock ed., ser. NATO ASI. Kluwer Academic, 1996.

[60] C. L. Jia, B. Kabius, K. Urban, K. Hermann, J. Schubert, W. Zander, and A. I. Braginski, "The microstructure of epitaxial YBCO films on steep stepps on $laalo_3$ substrates," *Physica C*, vol. 196, p. 211, 1992.

[61] Y. Zhang, N.Wolters, X. H. Zeng, J. Schubert, W. Zander, H. Soltner, H. R. Zi, M. Banzet, F. Ruder, and A. I. Braginski, "Washer rf-SQUID magnetometers with coplanar resonators at 77k," *Appl. Superconductivity*, vol. 6, pp. 358–390, 2001.

[62] M. Bick, J. Schubert, M. Fardmanesh, G. Panaitov, M. Banzet, W. Zander, Y. Zhang, and H.-J. Krause, *IEEE Trans. Appl. Superconductivity*, vol. 11, pp. 1339–1342, 2001.

[63] P. Chaudhari, J. Mannhart, D. Dimos, D. D. Tsuei, J. Chi, M. M. Oprysko, and M. Scheuerman, *Phys. Rev. Lett.*, vol. 60, p. 1653, 1988.

[64] P. Selders, A. Castellanos, M. Vaupel, and R. Woerdenweber, *IEEE Trans. Appl. Superconductivity,*, vol. 9, pp. 2967–2970, 1999.

[65] M. Fardmanesh, J. Schubert, R. Akram, M. Bick, M. Banzet, W. Zander, Y. Zhang, and H.-J. Krause, "Noise, junctions characteristics, and magnetic field dependence of bicrystal grain boundary rf-squids," Applied Superconductivity Conference, Houston, TX, Aug. 2002.

[66] M. Fardmanesh, "Development and optimization of HTc SQUID technology for a high resolution magnetic imaging," Juelich (FZJ-A-IB) -Bilkent (TUBITAK)," Joint Research and Development, 2000.

[67] M. Fardmanesh, J. Schubert, and M. Banzet, "Combinatorial ion beam etching process for step-edge junction SQUIDs," Germany, 199 54 167.1, Europe and USA," Patent.

[68] E. F. Fleet, S. Chatraphoron, and F. C. Wellstood, "HTS scanning SQUID microscopy of active circuits." *IEEE Trans. on Appl. Superconductivity*, vol. 9, pp. 4103–4106, 1999.

[69] M. Fardmanesh, J. Schubert, R. Akram, M. Bick, M. Banzet, W. Zander, Y. Zhang, and H. J. Krause, "Junction characteristics and magnetic field dependencies of low noise step edge junction rf-squids for unshielded applications," *IEEE Trans. Appl. Supercond*, vol. 13, no. 2, p. 833, 2003.

[70] A. Marx, U. Fath, L. Alff, and R. Gross, *Appl. Phys. Lett.*, vol. 67, no. 13, pp. 1929–1931, 1995.

[71] T. Minotani, S. Kawakami, Y. Kuroki, and K. Enpuku, *Jpn. J. Appl. Phys., pt. 2*, vol. 37, no. 6B, pp. L718–721, 1998.

[72] L. P. Lee, M. Teepe, V. Vineskiy, R. Cantore, and M. S. Colclough, *Appl. Phys. Lett.*, vol. 66, no. 22, pp. 3058–3060, 1995.

[73] E. Dantsker, S. Tanaka, and J. Clarke, *Appl. Phys. Lett.*, vol. 70, no. 15, pp. 2037–2039, 1997.

[74] *DatenblattzurStromquelle*.

[75] R. Otto, *Messknecht*, ISI-4-6-92, Forschungszentrum Juelich, 1992.

[76] J. Schubert, *Peronliche Mitteilung*, 2000.

[77] M. Fardmanesh, J. Schubert, R. Akram, A. Bozbey, M. Bick, M. Banzet, D. Lomparski, W. Zander, Y. Zhang, and H. J. Krause, *IEEE Trans. Appl. Supercond.*, vol. 13, p. 873, 2003.

[78] A. Barone and G. Paterno, *Physics and Applications of the Josephson Effect*. Wiley Interscience, 1982.

[79] J.-K. Heinsohn, R. Dittmann, J. R. Contreras, J. Scherbel, A. Klushin, and M. Siegel, *IEEE Trans. Appl. Superconductivity*, vol. 11, no. 1, pp. 795–798, 2001.

[80] E. E. Mitchell, C. P. Foley, K.-H. Mueller, and K. E. Leslie, "Vortex penetration and hysteretic behaviour of narrow planar josephson junctions in a magnetic field," *Physica C*, vol. 321, pp. 219–230, 1999.

[81] H. Shimakage, R. H. Ono, L. R. Vale, and Z. Wang, *IEEE Trans. Appl. Superconductivity*, vol. 11, no. 2, pp. 4032–4035, 2001.

[82] P. A. Rosenthal, M. R. Beasley, K. Char, M. S. Colclough, and G. Zaharchuk, "Flux focusing effects in planar thin-film grain-boundary josephson junctions," *Appl. Phys. Lett.*, vol. 59, pp. 3482–3484, 1991.

[83] O. G. Vendik, I. B. Vendik, and D. I. Kaparkov, *IEEE Trans. Microwave Theory Tech.*, vol. 46, no. 5, pp. 469–478, 1998.

[84] C. Foley, E. Mitchell, S. Lam, B. Sankrithyan, Y. Wilson, D. Tilbrook, and S. Morris, *IEEE Trans. Appl. Supercond.*, vol. 9, p. 4281, 1999.

[85] E. J. Tarte, G. A.Wagner, R. E. Somekh, F. J. Baudenbacher, P. Berghuis, and J. E. Evetts, *IEEE Trans. Appl. Superconductivity*, vol. 7, no. 2, pp. 3662–3665, 1997.

[86] Y. Zhang, "Evolution of HTS rf-SQUIDs," *IEEE Trans. Appl. Superconductivity*, vol. 11, pp. 1038–1042, 2001.

[87] H. Burkhardt, O. Bruegman, A. Rauther, F. Schnell, and M. Schilling, *IEEE Trans. Appl. Supercond*, vol. 9, no. 2, pp. 3153–3156, 1999.

[88] K. Enpuku, T. Minotani, F. Hiraishi, A. Kandori, and S. Kawakami, *IEEE Trans. Appl. Supercond.*, vol. 9, pp. 3109–12, 1999.

[89] M. Fardmanesh, J. Schubert, R. Akram, M. Bick, M. Banzet, W. Zander, Y. Zhang, and H. J. Krause., "Analysis of electrical characteristics and magnetic field dependences of YBCO step edge and bicrystal grain boundary junctions for rf-SQUID applications." *Supercond. Sci. Technol.*, vol. 17, pp. 375–380, 2004.

[90] X. H. Zeng, Y. Zhang, B. Chesca, K.Barthel, Y. S. Greenberg, and A.I.Braginski, "Experimental study of the amplitude-frequency characteristics of HTS rf-SQUIDs," *J. Appl. Phys.*, vol. 88, pp. 6781–6787, 2000.

[91] E. Il'ichev, G. S. Krivoy, and R. P. J. Ijsselsteijn, *Physica C*, vol. 377, pp. 516–20, 2002.

[92] M. Fardmanesh, J. Schubert, R. Akram, M. Bick, M. Banzet, W. Zander, and J.-H. Krause, European Conference on Applied Superconductivity, Copenhagen, Denmark, August 26-30 2001.

[93] M. Bick, "HTSL-rf-SQUID sensoren in magnetfeldern: Charakterisierung und stursignalunterdruckung," PhD Thesis, Institut fur Schichten und grenzflachen, Bonn, University., 2001.

[94] D. Lomparski, *SQUID-I-V 1.0 Programm zur Mess daten erfassung und Mess ablaufsteuerungin LabView*, ISI, Forschungszentrum, Juelich., 2000.

[95] S. Mayer, "Fluxmaster teslameter, bedienungsanleitung, s. mayer messgerate,," Ph.D. dissertation, Munster, Deutschland, 1993.

[96] C.M.Falco and W.H.Parker, "Operation characteristics of thin-film rfbiased SQUID," *J.Appl.Phys*, vol. 46, pp. 3238–3245, 1975.

[97] H. Bousack, "A SQUID 9-channel module for application in biomagnetics, nondestructive evaluation, and geomagnetism," ISI, Research Centre Juelich GmbH, Germany, Final report 13N7327iA (in German).

[98] L. Vant-Hull, R. A. Simpkins, and J. Harding, *Phys. Lett.*, vol. A24, p. 736, 1967.

[99] N. Ishikawa, K. Nagata, H. Sato, N. Kasai, and S. Kiryu, "Effect of rf interference on characteristics of dc SQUID system," *IEEE Trans. Appl. Supercond.*, vol. AS-3, pp. 1910–1913, 1993.

[100] R. H. Koch, V. Foglietti, J. R. Rozen, K. G. Stawiasz, M. B. Ketchen, D. K. Lathrop, J. Z. Sun, and W. J. Gallagher, "Radio frequency interference in dc SQUID," *Appl. Phys. Lett.*, vol. 65, pp. 100–102, 1994.

[101] M. Muck, B. Chesca, and Y. Zhang, "Radio frequency squid and their applications," in *Institute of Thin Film and Ion Technology SQUID application Group Publications.* Forschungszentrum Juelich, 1999, pp. 15–17.

[102] A. I. Braginski, J. K. H, and J. Vrba, "SQUID magnetometers," Academic press, San Diego, April 1999, a contribution for Superconducting Devices.

[103] R. Akram, "Development and optimization of HTc SQUID technology for a high resolution magnetic imaging system," Juelich (FZJ-ISG2) and Bilkent (EEE dept.)," Joint Research and Development Project, 2003.

[104] W. L. Goodman and B. S. Deaver, "Detailed measuremnts of the quantized flux states of holow supercondcuting cylinder." *Phys. Rev. Lett.*, vol. 241, pp. 870–873, 1970.

[105] F. P. Rogers, "A device for experimental observation of flux vortices trapped in superconducting thin films," Master thesis, Massachust Institute of Technology, 1983.

[106] A. Mathai, D. Song, Y. Gim, and F. C. Wellstood, "High reolution magnetic microscopy usin a dc SQUID," *IEEE Trans. Appl. Supercond.*, vol. 3, pp. 2609–2616, 1993.

[107] S. A. Gudoshnikov, O. V. Snigirev, L. V. Matveets, K. A. Andreev, A. M. Tishin, J. D. M. Muck, and C. Heiden, "Scanning SQUID microsocpe technique for measurements of ultrathin films magnetic properties," *Applied Superconductivity*, vol. 5, pp. 319–325, 1998.

[108] L. N. Vu, M. S. Wistrom, and D. J. V. Harlingen, "Design and implementation of a scanning SQUID microscope," *IEEE Trans. Appl. Supercond.*, vol. 3, pp. 1918–1921, 1993.

[109] R. C. Black, F. C. Wellstood, E. Dantsker, A. H. Miklich, J. J. Kingston, D. T. Nemeth, and J. Clarke, "Eddy current microscopy using a 77k superconducting sensor," *Appl. Phys. Lett.*, vol. 64, pp. 100–102, 1994.

[110] R. C. Black, F. C. Wellstood, E. Dantsker, A. H. Miklich, D. T. Nemeth, D. Koelle, F. Ludwig, and J. Clarke, "Microwave microscopy using a superconducting quantum interference device," *Appl. Phys. Lett.*, vol. 66, pp. 99–101, 1995.

[111] R. C. Black, F. C. Wellstood, E. Dantsker, A. H. Miklich, D. T. Nemeth, D. Koelle, and J. Clarke, "Imaging radio-frequency fields using a scaning SQUID microscope," *Appl. Phys. Lett.*, vol. 66, pp. 1267–1269, 1994.

[112] P. Pitzius, V. Dworak, and U. Hartmann, "Ultrahigh resolution swcanning SQUID microscope, a 24," ISEC'97 6th International Superconductive Electronics Conference, June 25-28 1997, Berlin, Germany.

[113] T. S. Lee, Y. R. Chemla, E. Dantsker, and J. clarke, "High tc SQUID microscope for room temperature samples," *IEEE Trans. Appl. Supercond.*, vol. 7, pp. 3147–3150, 1997.

[114] Y. Chemla, H. L. Grossman, T. S. Lee, J. Clarke, M. Adamkiewicz, and B. B. Buchanan, Presented at ASC 98 (unpublished), 1998.

[115] B. J. Roth, n. G. Sepulveda, and J. P. Wikswo, "Using a magnetometer to image in two dimensional current distribution," *J. Appl. Phys.*, vol. 65, pp. 361–372, 1989.

[116] "MGMA SQUID microscope, necera inc."

[117] R. Rottier, "The application of superconductors in medicine, Web site," 2000.

[118] Y. Zhang, G. Panaitov, S. G. Wang, N. Wolters, R. Otto, J. Schubert, W. Zander, H. J. Krause, H. Soltner, H. Bousack, and A. I. Braginski, "High-temperature SQUID gradiometer for magnetocardiography in unshielded environment," *Appl. Physic. Lett*, vol. 76, 2000.

[119] A. I. Braginski and H. J. Krause, "Nondestructive evaluation using high-teperature SQUIDs," *Physica C*, p. 3637, 2000.

[120] H. J. K. et al., "Mobile HTS SQUID system for eddy current testing of aircraft," D. O. Thompson und D. E. Chimenti," Review of Progress in QNDE 16, 1997.

[121] C. P. Foley, D. L. Tilbrook, K. E. Leslie, R. A. B. andJ. Du, S. K. Lam, G. B. Donaldson, P. W. Schmidt, and D. A. Clark, "Geophysical exploration using magnetic gradiometery based on hts squids," *IEEE Trans. Appl. Supercond.*, 2001.

[122] J. R. Kirtley, P. John, and J. Wikswo, "Scanning SQUID microcopy," *Anual Review of Materials Science*, vol. 29, pp. 117–148, August 1999.

[123] R. Akram, "Development of a high resolution magnetic imaging system," Juelich (FZJ-ISG2) and Bilkent (EEE Dept.)," Progress Report, 2002.

[124] http://hyperphysics.phy-astr.gsu.edu/hbase/magnetic/curloo.html♯c1.

[125] M. Fardmanesh, R. Akram, M. Schmidt, and H. J. Krause, "Development and optimization of HTc SQUID technology for a high resolution magnetic imaging," forschungszentrum Juelich (ISG-2)-Bilkent University (EEE Dept.)," Joint Research and Development project, 2004.

[126] *http://www.mushield.com*, http://www.amuneal.com/theorie/default.htm.

[127] "Magnetic shielding," http://www.amuneal.com/.

[128] "Dipole field calculation," http://hyperphysics.phy-astr.gsu.edu/.

[129] M. Fardmanesh and J. Schubert, *Asymetric Junctions rf-SQUID Magnetometer and Gradiometer Designs on Bi-Crystal Substrate*, German patent (DE)19 902 580A1.